UNIVERSITÄT FÜR BODENKULTUR WIEN
University of Natural Resources
and Life Sciences, Vienna

Doctoral Dissertation

Tracing biotic and abiotic stress reactions on the micro-level in softwood tracheids and cuticles

submitted by

Nadia SASANI, MSc

in partial fulfilment of the requirements for the academic degree

Doktorin der Bodenkultur (Dr.nat.techn.)

Vienna, August 2022

Supervisor:

Assoc. Prof.in Dr.in rer.nat. Notburga Gierlinger
Institute of Biophysics
Department of Nanobiotechnology (DNBT)

Doktorarbeit, vorgelegt am Department für Nanobiotechnologie der Universität für Bodenkultur, Wien, zur Erlangung des Titels Doctor rerum naturalium technicarum (Dr. nat. techn.)

Betreuer:

Assoc. Prof. Dr.rer.nat. Notburga Gierlinger

Berater:

Assoc. Prof. Dipl.-Ing. Dr. Sabine Rosner

I hereby declare that I am the sole author of this work. No assistance other than that which is permitted has been used. Ideas and quotes taken directly or indirectly from other sources are identified as such. This written work has not yet been submitted in any part.

Diese Arbeit wurde aus Mitteln des

START Project [Y-728-B16]

Fonds zur Förderung der wissenschaftlichen Forschung im Rahmen eines START-Projekts mit der Nummer Y-728-B16.

Contents

Abstract

Biotic and abiotic stress factors threaten trees under a changing climate. Land plants, unlike animals, cannot escape from harmful situations, and thus need tolerance mechanisms to cope with stress factors. In my thesis, I studied abiotic drought stress responses in the wood of three larch species and biotic rust infection responses in Norway spruce needles.

Abiotic stress such as drought is becoming more and more a limiting factor for tree growth, and we need a better understanding of the tree responses. We studied the physiological, anatomical and cell wall chemistry reactions in the xylem of European larch (EL, *Larix decidua*), Japanese larch (JL, *Larix kaempferi*), and hybrid larch (HL) saplings subjected to an artificial drought. EL developed high hydraulic safety wood and showed with anisohydric behaviour a different strategy to deal with drought. All species showed higher lignin levels in the wood cells formed under limited water supply and HL induced latewood formation earlier than the other species.

Biotic stress, like *Chrysomyxa ledi* var. *rhododendri* infection affects alpine Norway spruce (*Picea abies* L. Karst.) stands. Neighbored trees may be resistant or susceptible to needle-rust infection and the reason behind the different reaction is of interest. Therefore we studied the microstructure and chemistry of the needle cuticle, as the first main entrance point of the pathogen. Raman imaging visualized aromatic cuticle components together with waxes, cutin, minerals, and carbohydrates on the microscale. Phenolic acids impregnated the whole cuticle and flavonoids, especially the periclinal upper epidermal walls. These aromatic components play a role in rust resistance as their composition, distribution, and amount change between susceptible and resistant needles.

All experimental approaches yielded detailed cellular information on biotic and abiotic stress responses and are useful for selective breeding, forest protection, and reforestation programs.

Kurzfassung

Biotische und abiotische Stressfaktoren bedrohen Bäume im Zuge des Klimawandels. Im Gegensatz zu Tieren können Landpflanzen schädlichen Situationen nicht entkommen und benötigen daher Toleranzmechanismen. In meiner Dissertation untersuchte ich die Reaktionen auf abiotischen Trockenstress im Holz von drei Lärchenarten und biotischen Rostbefall in Fichtennadeln.

Abiotischer Stress wie Trockenheit wird immer mehr zu einem begrenzenden Faktor für das Wachstum von Bäumen. Um die Reaktionen der Bäume besser zu verstehen, haben wir 3 Lärchenarten (Europäische Lärche EL, *Larix decidua*; Japanische Lärche JL, *Larix kaempferi* und Hybridlärche HL) einem kontrollierten Trockenstress unterzogen und die physiologischen, anatomischen und chemischen Reaktionen untersucht. EL verhalten sich anisohydrisch und entwickeln generell ein hydraulisch sichereres Holz. Unter begrenzter Wasserversorgung imprägnierten alle Arten die Zellwände mit mehr Lignin.

Biotischer Stress, wie die Infektion mit *Chrysomyxa ledi* var. *rhododendri*, beeinträchtigt die Bestände der Alpenfichte (*Picea abies* L. Karst.). Benachbarte Bäume können resistent oder anfällig für die Nadelrostinfektion sein, und der Grund für die unterschiedliche Reaktion ist unklar. Daher untersuchten wir die Mikrostruktur und die Chemie der Nadelkutikula als ersten Eintrittspunkt des Erregers. Mit Raman-Imaging wurden aromatische Substanzen zusammen mit Wachsen, Cutin, Mineralien und Kohlenhydraten auf der Mikroskala sichtbar gemacht. Phenolsäuren imprägnierten die gesamte Kutikula und Flavonoide insbesondere die periklinen oberen Epidermiswände. Diese aromatischen Komponenten spielen eine Rolle bei der Rostresistenz, da ihre Zusammensetzung, Verteilung und Menge zwischen anfälligen und resistenten Nadeln variiert.

Alle experimentellen Ansätze lieferten detaillierte zelluläre Informationen über biotische und abiotische Stressreaktionen und sind nützlich für selektive Züchtung, Waldschutz- und Wiederaufforstungsprogramme.

Acknowledgments

I would like to thank the people, without whom I would not have been able to finish this research, and without whom I would not have made it through my Ph.D. study.

The staff of the institute of biophysics at the University of Natural Resources and Life Sciences, Vienna, especially my supervisor Assoc. Prof. Dr.rer.nat. Notburga Gierlinger, whose support allowed my studies to go the extra mile, In addition, special thanks to Assoc. Prof. Dipl.-Ing. Dr. Sabine Rosner and Prof. Adya Singh whose insight and knowledge into the subject matter steered me through this research.

I would also like to thank, Peter, Bati, Nannan, and Martin for their assistance in measurements and technical support in my study. I am as well thankful to Meysam for always being there for me and supporting me empathically.

I am also especially grateful to my parents, my brothers, and sisters, especially Leila and Hamid who always encouraged me in so many ways. I always knew that you believed in me and wanted the best for me.

1. Introduction

1.1. Definition of plant stress

Stress in plants is a condition that disrupts plant function by increasing needs and reducing cell activity, followed by normalizations and improved resistance. Naturally, plants adapt fast to their metabolic fluxes and develop specific stress tolerance mechanisms. Depending on the intensity and duration, stress can lead to permanent damage or death in plants if it is beyond the capacity of plant adaptation. Other factors include plant species, growth conditions, and stressor types involved in the stress tolerance threshold [1, 2]

External and internal stresses in plants are two categories of stress. Unplanned gene mutations or strange cell division might lead to incompatible metabolic or genetic balancing reactions called internal stresses. In addition, biotic and abiotic are external stresses [1-3]. Biotic stresses include various living organisms attacking fungi, bacteria, oomycetes, nematodes, and herbivores. Plants use sophisticated strategies to prevent the progress of biotic stresses. The defense mechanisms against biotic stresses are controlled genetically, and these resistant genes against biotic factors are saved in the plant genome [3]. Pathogens are divided into three categories according to the way plants are fed: biotrophic, necrotrophic, and hemibiotrophic pathogens. Biotrophs keep their host alive and feed on living plant tissue. In contrast, necrotrophs produce toxins or tissue degrading enzymes leading to dead cells accessing the plant’s nutrients. In addition, some pathogens shift the strategy between biotrophs and necrotrophs during different stages of pathogenicity [4]. In addition, environmental or abiotic factors such as drought (water stress), excessive watering (waterlogging), extreme temperatures (cold, frost, and heat), salinity, and mineral toxicity can physically or chemically lead to a negative effect on growth and development of plants [3, 5]. Understanding the adaptive responses in the plant at the micro-level is very helpful for the development of rational breeding and transgenic strategies to impart stress tolerance in plants.

1.2. How stress affects plants

When plants are exposed to stress, plant response begins with a decline of one or several physiological functions, such as photosynthesis and transport of metabolites, because of the disturbance of cellular and molecular processes. As a result, the plants move away from the normal physiological state. Most plants will remain active in their coping mechanisms by acclamation of metabolic fluxes, activation of repair processes, and long-term metabolic and morphological adaptations. If plants are exposed to long-term stress or high-dose stress, the plants' stress coping mechanism is disrupted, leading to the plant's gradual death. A new standard physiological function will regenerate when the stressors are eliminated and the intensity of damage is not high. The new normal physiological process depends on external and internal factors such as the time of the stressor removal and the duration and intensity of the stress. When plants receive stress alerts in different forms in different organs, their reaction is through direct metabolic responses such as readjustment of metabolic fluxes and gene expression. The gene expression can modify the metabolic response of stressed plants and control the stress resistance minimum and the maximum [2, 6].

1.3. Plant defense system

Plants use two strategies to resist stress: physical or constitutive defense and induced defenses. Constitutive defense is by substances of the plant structure, such as bark, plant cell walls, and waxy cuticles. Innate immunity or basal resistance is triggered when pathogens cross the physical barrier. Plant cells could recognize the microbe-associated molecular patterns (MAMPs), including specific proteins, lipopolysaccharides, and cell wall components. Cell surface-resident pattern recognition receptors (PRRs) could perceive MAMPs. Receptors like kinases (RLKs) or receptors like proteins (RLPs) in plants encode the stress, and cellular and physiological responses begin. Suppose the pathogens could suppress the basal resistance. In that case, the plants will react more sharply by deliberate suicide at the infected cells called hypersensitive response (HR) with the production of antimicrobial molecules. After hypersensitive response in plants, it leads to systemic acquired resistance (SAR) that resists a wide range of pathogens over a long period. The infected tissue generates signals and then spreads throughout the plant. These plant signals or phytohormones include salicylic acid (SA), jasmonic acid (JA), ethylene (ET), and abscisic acid (ABA) [7-10]. Physiological responses vary depending on plant species and PAMPs perceived and can be rapid or delayed. However, there are some physiological responses in various plant cells, such as an increase in Ca^{2+} concentration, extracellular alkalinization, membrane potential depolarization, ion fluxes, phosphatidic acid (PA) production, and reactive oxygen species (ROS) production, and callose deposition [7]. Anatomical stress responses occur in plant organs such as roots, xylem, and leaves and include inhibition of cell elongation, localized stimulation of cell division, and alterations in cell differentiation status. Anatomical alteration under drought stress conditions starts with the effect on the cell structure of tree rings, which arises from the physiological and biochemical changes of the tree to survive. Xylem structure changes could limit the tree ring growth and hydraulic conductance. The potential of water in the stem is controlled by physiological and anatomical adaptation to climate-changing [11, 12]. Annual ring monitors to study the diversity in the tree ring width in response to alteration in environmental conditions when tree growth bounds by climate-changing such as temperature or precipitation [13]. Other anatomical changes in the xylem that could be impressed by environmental conditions include xylem size, cell wall, and xylem pit membranes [14]. Tracing diversity in xylem structure on a microscale between interspecies exposed to different water regimes allows one to know more about the link between the environmental condition and the function of the xylem. Potters *et al*. hypothesized that various stresses induce similar morphogenic reactions because of the expected molecular activities [6]. Many factors such as stress types, plants species, stress perception mechanisms, target tissues, and effects on cellular metabolism are involved. These anatomical changes are due to auxin, reactive oxygen species (ROS), and ethylene interactions. Different stress factors with various intensities can activate other sensors depending on the plant species. Each sensor could regulate a set of signals interaction that leads to compatibility reactions [5, 6].

1.4. Abiotic stress responses in trees

The significant abiotic stresses such as drought, cold, high salinity, and heat threaten the sustainability of natural and managed forest systems and restrict plant production worldwide. These environmental changes have led to complex adaptation mechanisms to overcome the challenges [15, 16]. Adaption of the tree to stress conditions has biological and human management components. For example, drought is one of the most severe abiotic stresses in climate change conditions, which has a high risk to plant health [17, 18]. To understand optimal growth conditions for trees in different environmental conditions the analysis of tree rings through time is necessary. Assessing the wood's anatomical properties, such as conduit diameter, cell wall thickness, and wood density showed differences between and within species and environmental changes' effects on the anatomical structure of the xylem on a micro-scale were not apparent. [13, 14, 19]. Recently, Piermattei *et al.* indicated that some characteristics, such as latewood lumen diameter and the cell wall reinforcement index, have a high inter-annual variation as a proxy of phenotypic plasticity [19].

Drought stress in trees: Changes in the microstructure and microchemistry of the vascular system?

Drought stress has an effect on plant growth at many different levels. The influence of drought stress at the physiological level is realized in roots and leads to turgor loss, reduced water potential, and decreased stomatal conductance. In the following, the internal CO_2 concentration and the net carbon fixation rate diminish, which leads to reduced growth rates and biomass production. When the balance between light capture and utilization is disturbed, photosynthesis is affected, and there is a reduction in carboxylation efficiency. This reduction causes waste of excess light energy and ROS production, which leads to macromolecule harm, including lipid peroxidation and protein denaturation. Cells produce antioxidative metabolites (glutathione, ascorbate, tocopherol) to prohibit oxidative damage and increment the expression of detoxifying enzymes (superoxide dismutase (SOD), catalase (CAT), and ascorbate peroxidase (APX)). In addition, drought stress could lead to osmotic stress by the synthesis and accumulation of compatible osmolytes (sugars, amino acids, glycine betaine, polyamines, and sugar alcohols). The induction of stress-responsive genes mediates physiological and biochemical responses [20]. Many factors such as plant species, water shortage, and stress time are involved in the plant's defense mechanism. Drought affects plant morphology, such as plant height, leaf size, leaf area, stem diameter, and the number of leaves per plant, causing changes in the meristematic regions [16, 21]. When the plants perceive the drought signals, they generate the signal molecules such as abscisic acid (ABA), Ca^{2+} inositol-1, 4, 5-triphosphate (IP3), and cyclic adenosine 50-diphosphate ribose (cADPR), which lead to external morphological and internal structural changes. In contrast, through signal transmission, plants respond with physiological and biochemical reactions such as photosynthesis changes, osmotic regulation metabolism, protein metabolism, antioxidant enzymes, and reactive oxygen metabolism. In addition, drought stress signals indirectly lead to expressing functional and regulatory genes for many substances (e.g., proline, glycine betaine, soluble sugars, aquaporin, kinases) involved in the plant's metabolism, morphology, physiology changes, and drought tolerance.

Most terrestrial plant species are at the risk of drying out because plants must constantly balance in a competitive environment to absorb carbon through the leaves and replace transpired water with dragged water from the soil. The vascular system, which plays an essential role in water transfer, has the anatomical and functional diversity to adapt to the variable hydraulic tension [22]. This system includes two components: tracheid and vessel, which as specialized vascular tissue play an essential role in long-distance water and solutes transport from the soil interface to the stems and leaves, mechanical support, and storage. When the xylem goes through the growth and development stage, it is alive and full of water and cellular organelles. It dies during the process of maturity to become functional. As an internal structure in all vascular plants, the xylem has high diversity and plasticity in the anatomical traits, which impress the hydraulic characteristics through changes in water conductivity and the ability of plants to adapt to different abiotic stresses [23, 24]. When the soil dries, hydraulic tension in the xylem lifts, which leads to osmotic stress. Osmotic stress increases the risk of cavitation and dysfunction in the xylem. The critical structural properties in xylem, such as the deposition of lignin, formation of the secondary cell wall, and cell wall thickness, need to be adapted to environmental requirements to be protected against cavitation and wall collapse [25-28]. Negative water pressure threatens the xylem conduit wall in two ways. The first is a compressive hoop around the xylem cell wall, spreading to the nearby wall by the middle lamella. The first is minor stress to uniform pressure in the adjacent cells. The second point of stress due to negative pressure in the xylem is in the double wall between water and gas-filled conduits—the thickened and lignified cell walls relative to the lumen area act as reinforcement against conduit collapse [29].

To investigate anatomical responses on the micro-level, saplings of European larch (*Larix decidua*), Japanese larch (*Larix kaempferi*), and their hybrid (*Larix x eurolepis*) were exposed to drought stress in controlled greenhouse experiments. We compare the anatomical and physiological reactions in different larch species [30]. We have chosen these species because they have great socio-economic importance in several parts of the northern hemisphere. Plantation of European larch outside their native range were vulnerable to European larch canker (*Lachnellula willkommii Hartig*). Therefore Japanese larch was planted as an alternative but failed in adaptation in many locations because of the sensitivity to summer drought [30]. Consequently, we hypothesized that Japanese larch is more drought sensitive than European larch and that the hybrid may show higher drought plasticity during growth. Therefore, we studied the tree larch species' hydraulic vulnerability and drought reaction with constitutive wood anatomy to elucidate different drought response strategies:

Sasani, N., Pâques, L.E., Boulanger, G. et al. Physiological and anatomical responses to drought stress differ between two larch species and their hybrid trees (2021). https://doi.org/10.1007/s00468-021-02129-4

Additionally, responses in cell wall chemistry (lignification) were investigated using Confocal Raman microscopy (see 1.6).

1.5. Biotic stress responses in plants

The effect of living organisms is called biotic stress, which includes viruses, fungi, bacteria, nematodes, insects, and weeds [31]. These agents disrupt forest ecological, economic, and social performance with adverse effects on tree growth. It is worth noting that climate change plays a vital role in providing favorable conditions for these factors and reducing defense responses in trees [32]. Fungi are known as one of the most critical biotic stress factors to hurt the growth of trees. Long-term interaction between fungi and trees has led to the evolution of these pathosystems, and observed phenotypic diversity in those trees is expected [31, 32].

Norway spruce needles cuticle: which factors induce rust resistance?

When the pathogen interacts with a specific host, there are two possible responses in the plant: compatible response or/and incompatible response. The outcome of compatible response is the disease, while the second result is mild or no disease. The non-pathogenicity of a particular pathogen in a specific host (incompatible response) while being a sensitive host for that pathogen indicates the possibility of genetic resistance to aid the identification of the pathogen and activate the immune system in that host. For example, some Norway spruce (*Picea abies*) trees indicate disease when infected with the fungus pathogen *Chrysomyxa rhododendri* (a compatible response). Still, some individual trees can hurt less and control the disease by resistance (an incompatible response). However, the emergence of resistance to the disease ranges from extreme susceptibility with significant disease symptoms to complete resistance with the complete lack of any or some disease symptoms [9, 32, 33]. Ganthaler *et al.* also acknowledged that spruce resistance to *C. rhododendri* is a quantitative feature with a significant phenotypic difference, and existing trees with remarkable low susceptibility are scarce [34]. *Chrysomyxa rhododendri*, as a rust species pathogen in Norway spruce in the European Alps, can cause needle yellowing during summer, followed by needle dropping in autumn. Its life cycle terminates by overwintering in the leaves of rhododendron (*Rhododendron ferrugineum or R. hirsutum*) plants as the primary host [32, 35, 36]. Decreased timber yield and disorder in rejuvenation are two of the destructive effects of this fungus in subalpine Norway spruce forests [34]. When the pathogen (basidiospore) penetrates current-year developing spruce needles, it dominates the varied defense strategies that trees have evolved [37]. These strategies include multiple constitutive and inducible defenses, which act physically and chemically to control and eliminate the pathogen. Constitutive defenses serve at the frontline of the defense system in different parts of plants at all times. Some anatomical properties or pre-formed structural barriers act in all plants as physical and chemical barriers against fungal and bacterial attacks, such as the suberized bark, the cuticle, trichomes, papillae, thorns, and prickles. These can be constitutive or induced by wounds or exposure to biotic stressors [38]. The first site of contact of *C. rhododendri* with a needle is the cuticle covering plants' outermost surfaces, such as leaves, floral parts, fruits, seeds, stems, and roots [9]. The cuticle protects the epidermis and consists of a waxy crystalline and lipidic amorphous layer saturated with phenolic components (phenolic acids and flavonoids) [9, 39]. This hydrophobic structure, whether thin or thick, can prevent water loss and plays a role in defending against pathogens and limiting infection caused by them [9]. If disease agents cross defense barriers, acquired or induced resistance is stimulated. Induced resistance is achieved by activating the host's genetically programmed defense pathways. This resistance results in alterations that reduce the effects of further biotic attacks [32, 33, 40]. Eyles has classified induced defense mechanisms into five groups, and all or several of these mechanisms may appear in a tree response. These mechanisms include inducible chemical defenses, inducible protein-based defenses, inducible anatomical defenses, ecological or indirect defenses, and Inducible civilian defenses [33].

For chemical defenses, secondary metabolites, such as terpenoids, phenolic, and alkaloids, indirectly impede the pathogen's growth and reproduction due to their toxic and antimicrobial activity. The phenolic class includes various chemical defense-related compounds such as flavonoids, anthocyanins, phytoalexins, tannins, lignans, and furanocoumarins, which affect in different ways the pathogen metabolism or cellular structure and are often pathogen-specific in their toxicity [9, 33]. Other phenolic compounds have variable concentration levels in Norway spruce during needle development [41]. They can be constitutively in healthy plants and induced in response to infection. For some phenolic components such as flavonoids, stilbenes, simple phenylpropanoids, and the precursor shikimic acid, changes in concentrations were correlated with different degrees of infection [34]. In addition, Ganthaler *et al.* demonstrated that a combination of constitutive and inducible accumulation of phenolic compounds is associated with the lower susceptibility of individual trees to *C. rhododendri* [32, 34, 42]. Probing the chemical responses of the whole needle might overlay distinct changes on the microscale, e.g., in the cuticle. Therefore, we aimed to investigate the microchemistry of the needle cuticle by Confocal Raman microscopy and compare the resistant Norway spruce cuticles with needles from neighboring trees infected with *C. rhododendri*. As only a few studies have used Raman microscopy on plant surfaces [39], we first had to dive deeper into the methodology of Raman imaging of plant surfaces

1.6. Raman imaging of plant tissues

Raman imaging probes the molecular vibrations at every position of the plant sample in context with the anatomical structure.

Molecular vibration

The atoms that make up a molecule are connected by chemical bonds, in which the distance between atoms is changeable. Therefore, the vibration of molecules in the standard modes can be explained in classical mechanics by using the counterexample of simple balls connected by springs. Like massless springs, the internuclear forces attempt to keep the molecule together to restore the bond lengths or bond angles to specific equilibrium values [43, 44]. Many factors such as the energy, the strength among the bonds, and the constants of motion are involved [45, 46]. To calculate the vibrational frequency, v (in s^{-l}) that follows Hooke's law equation (1) has been used in which: Force constant of the spring is shown by f (N/m), and μ is the reduced mass in kg [47].

$$v = 1/2\Pi \sqrt(f/\mu) \quad (1)$$

Another aspect is the molecular vibration energy and transitions between different energy levels, which is a concept in quantum mechanics. The power of the molecules consists of translational, rotational, vibrational, and electronic energy [44]. The following equation (2) presents the vibrational energy:

$$E = hv_0\,(v + 1/2) \quad (2)$$

The vibrational quantum number is shown by v, v_0 shows the vibrational frequency of the ground state, and h is Planck's constant [47]. Each atom in a molecule can vibrate with three independent degrees of freedom of motion in the x, y, or z-direction. Therefore, the total number of vibrations in a molecule with N atomic nuclei will be 3N-6 for a nonlinear molecule and a liner molecule, 3N-5 [45, 46]. Two groups of vibrations are described based on vibrational motion: stretching and deformation. Stretching vibrations move along a bond and go hand in hand with a change in bond length, while in deformation or bending vibrations, the bond angle changes. In more detail, vibration classifications include asymmetric and symmetric stretching, wagging, scissoring, and rocking or breathing modes [45]. There are two different techniques to monitor these vibration motions in atoms of the molecule: infrared (IR) spectroscopy and Raman spectroscopy. These data about molecular vibrations are obtained in the form of vibrational spectra and are based on the interactions of electromagnetic radiations [43-46]. According to oscillation frequencies, there are different forms of electromagnetic radiation, such as Gamma rays, X-rays, ultraviolet (UV) radiation, visible light, NIR and mid-IR radiation, and terahertz (far-infrared) radiation, microwaves, and radio waves. For Raman and infrared spectroscopy, the range from UV to far infrared is used. The wavelength λ (the length of one wave), wavenumber $\tilde{V}$ (the number of waves per unit length), and frequency v are three features of electromagnetic radiation. Frequency v (in s^{-l}) in vibrational spectroscopy is shown by wavenumber V (cm^{-1}), which defines the number of waves in a 1 cm wave train per unit of time [45]. The following equations (3) and (4) show the relation between these parameters and the speed of light (in a vacuum is 2.997925 x 1010 cm/sec) and the refractive index (n) of the material. When light travels through matter, its speed relative to a vacuum will be decreased. The ratio of light speed in a vacuum to the speed of light in a matter is its refractive index. For instance, the refractive index of air is 1.0003.

$$\tilde{V} = v/(c\,/\,n) \quad (3)$$

$$\tilde{V} = 1\,/\,\lambda \quad (4)$$

In vibrational spectroscopy, the Raman scattering or infrared absorbance is plotted along the wavenumber as it is proportional to frequency. Frequency and energy are two standard features between radiation and molecules [44]. Raman and infrared spectroscopy both probe molecular vibrations based on different physical phenomena. Raman spectroscopy measures inelastic light scattering, while infrared spectroscopy detects absorbed photons. Therefore, the underlying section rules are different, and acquired spectra often complement each other. Raman scattering depends on changes in the polarizability in the electron cloud, while infrared depends on changes in the dipole moments in the molecular bonds. One of the advantages of Raman over infrared is that it is possible to study fresh plant samples in-situ in water. Still, it comes along with problems of sample degradation and autofluorescence [48].

Raman spectroscopy

The first time using the Raman method returned to the 1930s, and its first application in plant science was in 1984 with the investigation of tracheid cells. Essential specifications of Raman spectroscopy are that it is non-destructive, it does not need treatment for intact tissue, and the intensity of the water bands as solvents is low [49, 50]. In combination with microscopy, Raman spectroscopy is utilized to identify the microstructure features of different tissues or cell layers non-destructively and with high spatial resolution [48, 49, 51-53]. Raman spectroscopy results from the interaction of the focused laser beam and the sample under investigation. When photons of a focused laser beam strike the sample's molecules, the scattered photons will be produced. Shifts in the energy (E) and frequency of scattered photons that correspond to the vibrational frequencies of the samples are measured by Raman spectroscopy [50, 52, 54, 55]. The scattered light can be of two types: elastic Rayleigh scattering and inelastic Raman scattering. There is no difference between the irradiated photon and reflected photon in terms of energy and wavelength in Rayleigh scattering ($E = Eo$). Inelastic scattering happens when the interaction between molecules and photons leads to energy exchange. Compared to the original photons, inelastic scattered light with higher or lower wavelengths is measured based on loss or gain in energy. If the scattered light gains the vibrational energy of the molecules, then the scattered light will reach a higher frequency than the incident photon. This case is known as anti-stokes Raman scattering ($E = Eo + Ev$). The molecules must be in the excited modes before oscillating between the irradiated light and molecules. In the opposite case, the irradiated light reaches a lower frequency by giving its energy to the molecules. This process is called Stokes Raman scattering ($E = Eo - Ev$). In comparison between anti-stokes and stokes, the intensity of stokes is higher because very few molecules are in the excited state at room temperature. Due to the high intensity of stokes over anti-stokes Raman spectroscopy usually focuses on stokes scattering of the sample [45, 55-57]. The Raman microscope is based on a monochromatic light source—a laser, a microscope with objectives, a spectrometer, and a detector [50, 58]. Lasers radiate the light of a specific wavelength. Different types can be used for Raman microscopy: krypton (530.9 and 647.1 nm), helium-neon (632.8 nm), neodymium (1064 nm and 532 nm), argon (488.0 and 514.5 nm), and diode lasers (630 and 780 nm) [48-50, 59]. The ideal state of a Raman spectrum is to have the lowest background and highest Raman signal (lowest noise). There is an inverse relationship between the increase in the wavelength with the Raman signal and sample autofluorescence [50].

Two different technologies exist to collect Raman scattering: Dispersive Raman spectroscopy and Fourier transform Raman spectroscopy (FT). The intensity of the scattered photon depends on several factors, including the intensity of the exciting photon and the fourth power of excitation frequency. Dispersive Raman spectroscopy consists of the laser with a wavelength in the visible range for excitation, a dispersive spectrometer, and a charge-coupled device detector (CCD) for detection that is typically placed at the exit focal plane of a single-stage [48, 50, 60]. The CCD is a low focal length Raman monochromator originally used in low astronomy light-sensitive imaging sensors. It is used to collect dispersive Raman spectra. In FT Raman spectrometers, interferometers or mirrors collect the scattered light induced by 1064 nm near-infrared (NIR) lasers, which solve the problem of sample fluorescence [51, 54, 57, 61].

The two main primary conditions for Raman vibrations are the polarizability and symmetry of the molecules. Displacement of electrons due to vibration leads to polarization in the molecules that directly affect the intensity of photon reflection. Symmetric stretches also appear in Raman spectra with high intensity. The acquired Raman spectrum consists of bands representing the vibration frequency of the chemical bonds of the sample. The band´s position, intensity, and form are characteristics used to identify the organic compound and functional groups in the sample under investigation [49, 62].

Another noteworthy point is the spatial resolution, which depends on the excitation wavelength, the selection of the objective lens, and its optical specifications (numerical aperture). Furthermore, by adding the confocal technique, the spatial resolution of Raman microscopy has been significantly improved [53, 55, 63]. Eventually, the filtered Raman signal enters the spectrometer to spread over CCD (charge-coupled device) camera [62, 64].

The spectral resolution which is the full width at half maximum (FWHM) of a narrow peak or how well the overlapping peaks can be differentiated, is determined by the following parameters: the focal length of the spectrometer, the grating, the pixel size on the charge-coupled device (CCD) camera, the entrance slit or pinhole, and the line shape preservation. The spectral resolution is higher when the focal length is longer, and the grating has a higher groove density. Also, the smaller the pixel size, slit, or pinhole, the higher the spectral resolution. Finally, the spectrometer should provide equal imaging quality to preserve the shape line. There are various ways to illustrate the spectral resolution or show how the system measures items such as pixel resolution, two-pixel criterion, and measurement of peak resolution on known reference samples [64, 65].

Additional advances in Raman microscopy include higher-efficiency solid-state lasers, holographic notch rejection filters, and silicon charge-coupled device (CCD) detectors, as well as the ability of Raman spectroscopy to put together with other analytical techniques, such as high-performance liquid chromatography, micro chromatography, scanning tunneling microscopy and atomic force microscopy. Particular approaches evolved, such as surface-enhanced Raman spectroscopy (SERS), coherent anti-stokes Raman scattering (CARS), and resonance Raman spectroscopy (RRS) make it possible to track molecules in low amounts, with high accuracy, high spatial resolution, and without fluorescence background [45, 48, 57, 66].

Spatial Resolution

To measure chemical structure, physical properties such as form, size, molecular orientation, interactions, and dynamics of the constituents of a heterogeneous plant sample on the micrometer scale, we need a confocal Raman microscope with a high spatial resolution. When analyzing heterogeneous samples, it is essential to remember that the intrinsic properties of scattered photons in different phases are different. Spatial resolution is strongly influenced by the wavelength (λ) of the laser and numerical aperture (NA) of the objective based on the following equation (5)[62]:.

$$\Delta \mathrm{x} = 0.61\lambda/\mathrm{NA} \tag{5}$$

The microscope objective's NA affects the waist and depth of the focused laser beam. However, the obtained values in practice are less than the theoretical resolution limit based on Agarwal's results. For example, at 514.5 nm, an excitation-based Raman microprobe reaches 1.6 micrometers (μm) spatial resolution and about 10 μm for a 1064 nm-based system using a 100× microscopic objective. [67]. To achieve the best possible spatial resolution and come near the theoretical diffraction limited spatial resolution, the use of a high NA objective, like oil immersion objectives, is recommended [44]. In addition to the numerical aperture, the way the sample is reflected or the total laser intensity (power/area) and the sample's illumination have an essential role in spatial resolution. The spatial resolution of a confocal Raman microscope includes depth (z) resolution in addition to lateral (x and y) resolution [49, 64].

Depth resolution

The depth resolution (the length of the region illuminated by the laser beam) depends on the volume of the focused laser. Moreover, it is also dependent on how the confocal aperture scatters back this volume of Raman photons into the spectrometer. In nontransparent media, depth resolution decreases due to the more expansion of focus in the scattered photons [57]. There is an aperture at the back focal plane of the system to limit the reception of scattered photons only close to the focus point. The effect of refraction at the sample/air interface is to shift the point of focus much deeper into the sample. Interpreting the structure of a multilayer sample from z-scan Raman data is impossible unless refraction is taken into account. An immersion objective reduces the refraction at the sample surface and improves the depth resolution by focusing all rays close to the apparent depth. A reasonable estimate of layer position and thickness from the Raman intensity variations is provided. However, different deeper layers have different refractive indexes. One of the other suggested effective solutions for keeping the depth resolution much closer to the actual values is to prepare a thin section of samples with clean edges. This approach also affects the lateral spatial resolution of the confocal Raman microscopy. In addition, the depth resolution is not recommended for studying the interfacial properties because it covers the deposited surface with increasing depth, and therefore the intensity is overestimated. They are changing the laser spot profile in some Raman systems [62, 68, 69]. In addition, the pinhole size or slit affects how the emission is presented as the detected signals. Moreover, the aperture determines how much light and Raman scatter is passed through the spectrometer. The range of slits and pinholes varies from 10 to 100 µm, affecting sensitivity, spectral, and depth resolution [48, 65].

Imaging approach: spectra pretreatment and image generation

Chemical imaging combines Raman spectroscopy and digital imaging, allowing access to the sample's molecular structure at every pixel [70]. The hyperspectral Raman data sets include massive information and need specialized chemometric tools to manage, visualize and interpret the data. The Raman data contain spatial and spectral information, which gives chemical information of the components of the sample at small surface or volume areas, called pixels or voxels. At every pixel (voxel), a spectrum presents the molecular fingerprint of the sample.

Some spectral pretreatments are beneficial before selected analysis methods and improve the spectra and image quality by removing noise, dead pixels, and variations that are not derived from the sample. Several ways to reduce signal/noise on spectroscopic data sets (smoothing) include median or mean filters, and Savitzky–Golay smoothing fast Fourier transform (FFT). Normalization (min-max on a selected band) is a way to remove unwanted intensity differences (e.g. changes in focus) to estimate the concentration from the Raman signal in quantitative analysis. Furthermore, baseline correction or subtraction is suitable to remove the high background when Raman images are affected by irregularly shaped baselines due to fluorescence. Another undesirable spectral feature that needs to be removed is spiking from cosmic rays, formed from high-energy particles from outer space or instruments. Recorded images from Raman measurement are hyperspectral data cubes with plenty of information. A Raman hypercube is an intensity data set of I (x, y, v), where x and y are the image pixel coordinates, and v is the wavenumber. In other words, it has two axes to analyze data: the spectral axis and the imaginary axis. This method makes it possible to characterize chemically and spatially components dependent upon each component's local concentration and intrinsic Raman scattering of each element. Intensity is also influenced by crystallinity, orientation, and domain size of components. In addition to that, other factors such as fluorescence background, scattering, and noise are also involved. The other issue that must be noticed is the speed of measurement by using the two different modes, standard and fast scanning. The ideal mode is to obtain an acceptable signal/noise in a short exposure time [71].

There are three ways to illuminate the sample: point, line, and global illumination. Raman maps can be obtained by raster-scanning the line-focused laser across the sample. A fiber-optic array probe and specialized filters (e.g., liquid-crystal tunable, dielectric acousto-optic filters) are used in global illumination to obtain high-quality spectral imaging and specific wavelengths from samples [55]. In Raman point mapping a Raman hypercube consists of x, y, and v, where x and y are the image pixel coordinates, and v is the wavenumber [71, 72]. In confocal microscopy, in addition to the two coordinates x and y, known as the lateral dimension of spatial resolution, depth resolution can be achieved in the z coordinates [71, 72] to derive four-dimensional (4D) information in stack scans [64, 66].

The acquired spectra of plant structures contain specific bands of different functional groups and overlapping wide bands that have been driven by the high chemical heterogeneity and close interaction of various complex polymers in the plant structure [73-75]. The hyperspectral dataset can be visualized and analyzed by univariate or multivariate methods. Univariate data analysis or classical image representations integrates the Raman bands to produce intensity-dependent heat maps and extract average spectra based on intensity thresholds for detailed analysis. It means that just one variable at a time, such as peak position (absolute or shift), peak height (absolute, relative or normalized), bandwidth (absolute or broadening), or area (absolute, relative, or normalized), is used in analyzing. However, there are some limitations to analyzing single spectra and single bands, and the multivariate data analysis method has the potential to overcome this challenge. The multivariate analysis uses all of the information in the spectral dimension at once. The most conventional methods in multivariate analysis are principal component analysis (PCA) and cluster analysis (hierarchical or k-means clustering) [48, 71, 76, 77]. Cluster analysis is a segmentation algorithm to find groups of pixels with similar spectra, i.e., similar chemical composition, but finding the correct number of clusters is also complex. Spectral unmixing algorithms describe images by a bilinear model analogous to the Beer-Lambert law (D = CST + E) that D is the raw Raman image, St the matrix of pure spectra, C the stretched concentration profiles, and E the error. The purest components of the dataset are extracted by the unmixing algorithm, which has several applicable methods in spectroscopy, such as Non-negative Matrix Factorization (NMF) and Multivariate Curve Resolution [39, 73]. Therefore, before tackling a specific research question with the Raman imaging approach, an optimized data acquisition as well as data analysis approach has to be established. In this thesis, this was successfully done for the analysis of spruce needle cuticles:

Paper 2:

Sasani, N., Bock, P., Felhofer, M. et al. Raman imaging reveals in-situ microchemistry of cuticle and epidermis of spruce needles. Plant Methods (2021). https://doi.org/10.1186/s13007-021-00717-6

1.7. Aims and research questions

This doctoral thesis aims to trace the effect of biotic and abiotic stress on trees at the micro-level. The two different stress types have been probed in softwood trees, spruce and larch, from two different projects and experimental set-ups.

1. The abiotic drought stress response was aimed to be probed in three different larch species out of a controlled greenhouse experiment to answer the following research questions:
    a. Is there a drought stress response laid down in wood anatomy and related to physiological traits?
    b. Is the different growth behavior of the three larch species (European, Hybrid, Japanese) reflected in different hydraulic vulnerability assessed by constitutive wood anatomy?
    c. Can we assess differences in the chemistry of the tracheid cell wall after drought reaction in the three larch species by Confocal Raman microscopy?
    d. Does drought stress influence the cell wall lignification?

2. The biotic stress response was aimed to be probed in the needle cuticle of paired spruce trees: one of them infected and the other one resistant to *C. rhododendri*
    a. Is Raman imaging an appropriate tool to probe the microchemistry of the cuticle and epidermal layer of spruce needles?
    b. What is the best sample preparation, experimental set-up, and data analysis approach for Raman imaging of spruce needles?
    c. Can we track differences between resistant and rust infected spruce needles in microchemistry assessed by Raman imaging?

The thesis aims to understand biotic and abiotic stress responses as climate change makes these threats more and more relevant. Understanding different trees and species, and reactions on the micro-level can help assess threats to inbreeding and reforestation programs.

1.8. Publication

This cumulative thesis is based on the following two first-author papers.

Paper1:

Sasani, N., Pâques, L.E., Boulanger, G. et al. Physiological and anatomical responses to drought stress differ between two larch species and their hybrid. Trees 35, 1467–1484 (2021). https://doi.org/10.1007/s00468-021-02129-4

Paper 2:

Sasani, N., Bock, P., Felhofer, M. et al. Raman imaging reveals in-situ microchemistry of cuticle and epidermis of spruce needles. Plant Methods 17, 17 (2021). https://doi.org/10.1186/s13007-021-00717-6

2. Methodology

2.1. Drought stress in larch trees

Sampling

Three-year-old saplings of European larch (*Larix decidua* Mill., EL, seed source: Sudetan larch seed orchard Theil-FR), 4-year-old saplings of Japanese larch (*Larix kaempferi* (Lamb.) Carrière, JL, seed orchard Flensborg-DK) and 2-year-old saplings of hybrid larch (HL, *Larix x eurolepis*, parents of family REVE-VERT-FR) were examined (Fig. 1). The plants were grown at Champenoux, France (48°45′09.3″ N, 6°20′27.6″ E) under two different water treatments using an automatic weighing and watering system [78]. The control plants (C-trees) were grown at 80% of the field capacity of the soil and drought-stressed plants (S-trees) at 30% of the field capacity of the soil for 70 days. The harvested trees were cut into 5 cm long stem segments. Physiological parameters such as biomass, transpiration rate, needle surface area, carbon isotope composition (δ13C), and relative water content were estimated, and the results were also published [30]. Stem samples were stored frozen at − 20 °C until the anatomical investigation. Normal wood of stem segments with perpendicular orientation to the central fiber axis was cut for anatomical study by cryomicrotome (CM 3050 S, Leica Biosystems Nussloch GmbH, Germany). Disposable microtome blades (N35HR Blade 35, Feather, Japan) were used to cut 10–20-µm-thick transverse sections. The image preparation process was followed using a Leica DM4000 M microscope equipped with a Leica DFC 320 R2 digital camera. In addition, these two software, namely Leica IM 500 (Leica, Weltzlar, Germany) and Image J software (HTTPS:// ImageJ. nih. gov), were used to stitch the digital images and measure the quantitative anatomical traits.

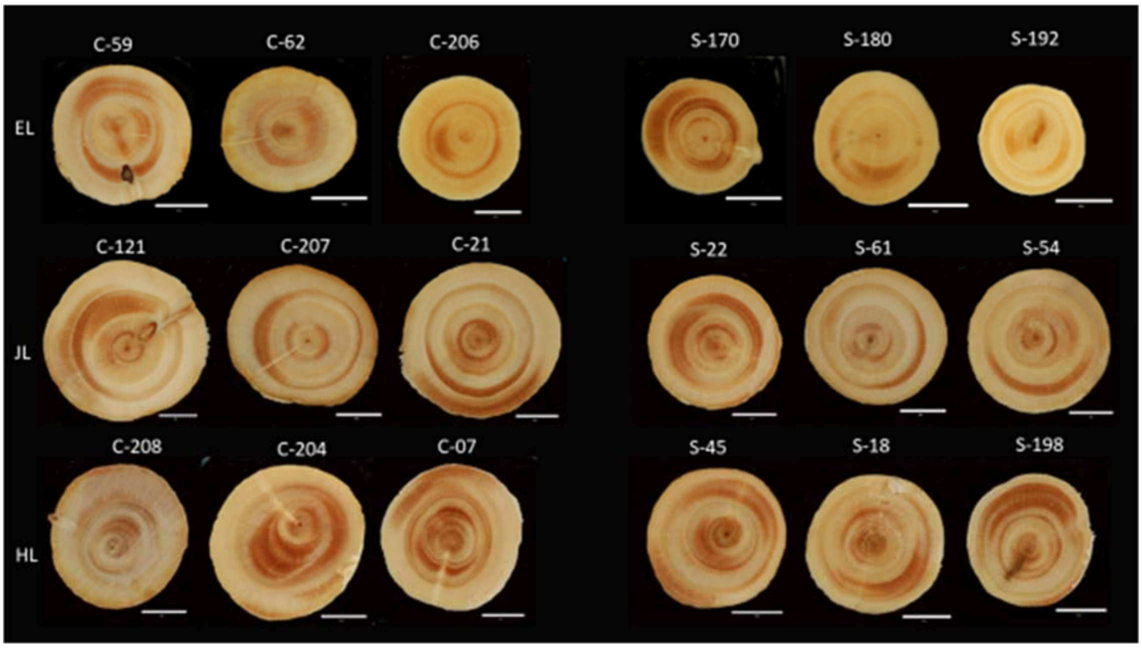

Fig. 1 Photographs of stem discs from control (C) and drought-stressed (S) trees of three different larch species; EL =European larch; HL= hybrid larch; JL=Japanese larch. The reference bars represent 10 mm.

Constitutive wood anatomy

Evaluation of some quantitative anatomical traits called constitutive wood anatomy before drought happens, such as tracheid dimensions, conduit wall reinforcement, and pit traits were undertaken [79]. The first formed earlywood tracheid of the latest annual ring was examined to indicate whether the variation in anatomical traits affected species' performance under drought stress. Double cell wall thickness (t) and lumen diameter (b) of earlywood cells were measured in radial (t_r, b_r) and tangential (t_t, b_t) directions in the first ten cell rows of the 2015 growth ring using

Image J software. For each of the four traits, a tree mean value was calculated from 20 single measurements performed on four different positions around the whole circumference. Conduit wall reinforcement was calculated in the radial ($(t_r/b_r)^2$) and tangential ($(t_t/b_t)^2$) direction [80]. Light microscopy and scanning electron microscope were used to compare the pit properties such as cavity area, pit membrane diameter, torus diameter, and pit aperture diameter.

Wood formation of control and drought stressed trees

The anatomical traits such as radial lumen diameters and the tangential double cell wall thickness were measured in one complete radial cell row of the latest wood increment to compare the impact of drought within and among Larch species. The undertaken method to define the anatomical traits was based on the SilviScan technology [79, 81, 82].

Statistical analyses

Differences between species and the drought treatment effects of some physiological and anatomical traits were statistically analyzed. The HSD test was used to estimate means and group differences for species, treatment, and species × treatment; the ANOVA analysis results are placed in tables 2, 3, and 4 in paper 1 [30]. We studied three trees per species and treatment, respectively, generally 18 trees. We pooled six trees per species to analyze the constitutive wood- and pit anatomy and then calculated 20 single measurements per tree for mean values. Finally, used tree mean values in statistical analyses (ANCOVA analyses).

Lignification changes

The division of cambial cells led to the cells in the tree ring that then go through the growth stages. Cell walls thicken and lignify in the last step of the growth stages before programmed cell death. Genetics, ontogenesis (organism development over time), hormone regulation, and environmental conditions affect this wood cell wall formation. For instance, tracheid diameter and cell wall thickness have played an essential role in trees' hydraulic efficiency and mechanical functioning [19, 83, 84]. We tracked the last step of cell wall formation and lignification to investigate changes in the microstructure and chemistry of trees grown under artificial drought stress using the Raman imaging approach. We applied a confocal Raman microscope (alpha300RA, WITec GmbH, Germany) with a 100 × oil immersion objective (NA 1.4, 0.17 mm with coverslip correction) (Carl Zeiss, Germany) to achieve Raman images from Larch wood cross sections. We used a linear polarized (0°) laser (λ_{ex} = 532 nm, WITec, Germany) with 25 mW power and integration time at 0.01 s for every pixel. An optic multifiber (100nm diameter, directed the scattered light to a spectrometer UHTS30 (WITec, Germany) (600gmm^{-1} grating) and a CCD camera (DU401DD) (Andor, Belfast, NorthIreland). We used the control Four acquisition software (WITec, Germany) to control the measurement. We used three trees per species and treatment, respectively. Generally, 18 trees, to analyze the chemistry of the tracheid cell wall after drought stress in two different areas along latewood last year in every tree by univariate analysis evaluated the spectra.

2.2. Biotic stress response in the spruce needle cuticle

Sampling & Sample preparation

Eight branches (about 40cm long and including several years of growth) of Norway spruce trees were received from Praxmar (Tyrol, 47° 09′ N/11° 07′ E, see also [85]) with high *C. rhododendri* infection pressure (Fig. 2a) [69]. Current-year needles (only last year) have been cut, and the severity or degree of infection varied (Fig. 2b). 15-20 µm thick cross-sections from these needles were cut using a cryo- microtome (CM 3050 S, Leica Biosystems Nussloch GmbH, Germany) (Fig. 2c). It is a rapid, non-invasive sectioning of tissue samples [70, 72]. Cryomicrotomy is preferred over other microtomy methods as the structure is not changed, and no embedding medium is necessary, which might interfere with the Raman signal of the sample.

After microtoming, the cross-sections were washed with distilled water and then a drop of water onto a glass slide and covered by a coverslip (0.16 mm thick). Finally, to prevent water evaporation and the formation of air bubbles, we seal the sample along the coverslip border with nail polish. The fresher and wetter the sample and the smoother the surface, the better the results have been because of decreased fluorescence emission.

Confocal Raman microscopy

A confocal Raman microscope (alpha300RA, WITec GmbH, Germany) with a 100 × oil immersion objective (NA 1.4, 0.17 mm with coverslip correction) (Carl Zeiss, Germany) was used to capture the Raman images from the Norway spruce needle thin cross-sections. The Raman measurement involves a linear polarized (0°) λex = 785 nm laser (WITec, Germany) with 150 mW laser power and an integration time of 0.1 s. We used a 785 nm laser for excitation because of the high sample fluorescence. An optic multifiber (100 nm diameter) directed the scattered Raman signal to a spectrometer UHTS30 (WITec, Germany) (600gmm^{-1} grating) and a CCD camera (DU401DD) (Andor, Belfast, NorthIreland). Calibration of the instrument to the silicon band of 520 cm^{-1} was undertaken before the Raman experiments began. For achieving the maximum possible diffraction-limited spatial resolution ($r = 0.61 \times \lambda/NA$), a spectrum in every 0.3 µm was captured. Therefore, the theoretical spatial resolution recorded was about 342 nm for the 785 nm laser.

Data analysis

Before data analysis, some pretreatments on Raman spectra were necessary: cropping the wavenumber region (300–1800 cm^{-1}), cosmic rays removal, and baseline correction. We used univariate (band integration) and multivariate (cluster analysis, non-negative matrix factorization (NMF)) data analysis by WITec Project plus 4.1 software (WITec, Germany). Average spectra were extracted by selecting pixels above an intensity threshold of the different Raman bands. Finally, we used OPUS 7.5 (Bruker, Germany) to export the extracted average spectra to evaluate and compare control and stressed samples.

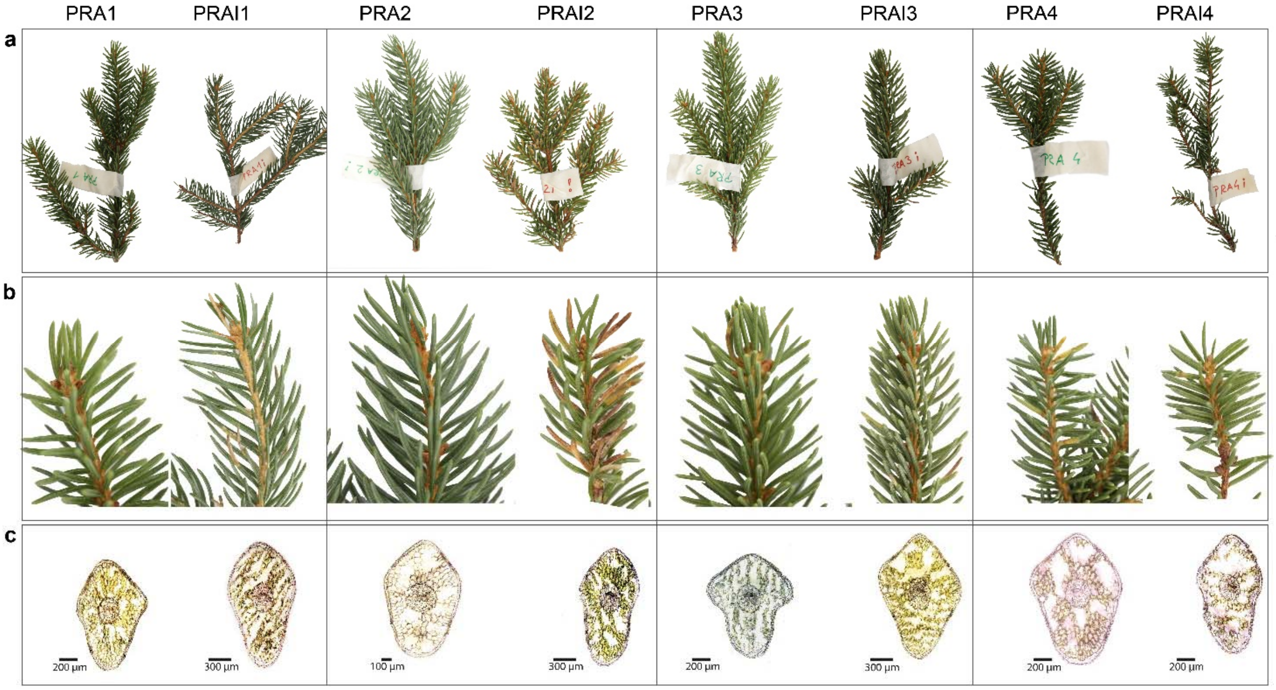

Fig. 2 Norway spruce twigs (A), needles in current-year (B), and microscopic picture of the cross sections (C) of the four pairs of Picea abies with different susceptibility to Chrysomixa rododendri rust fungi. Shoots were harvested in August 2019 from Praxmar (Tyrol, 47° 09′ N/11° 07′ E), and samples were immediately frozen to -20 °C after harvesting.

3. Results and discussion

European larch (EL), Japanese larch (JL), and hybrid larch (HL) differ greatly in their biomass and constitutive wood anatomy [19, 86, 87], but detailed information on comparative eco-physiological responses of the two parental Larix species and their hybrid is not available. Several studies have confirmed that the growth of EL is more strongly impacted by soil drought compared to other conifer species [88-92]. The first part of the thesis concerned physiological responses of EL, JL, and HL trees to drought and was conducted in collaboration with a research group in France, resulting in a joint publication [30].

3.1. Is there a drought stress response on wood anatomy and is it related to physiological traits?

Anatomical traits such as the diameter and cell wall thickness of the tracheid have changed as a response to drought stress. In the adapted trees, the lumen diameter decreased and cell wall thickness increased. Such anatomical traits boost the mechanical support of the stem and prevent xylem cell collapse [29, 80]. Differences in wood anatomy were studied in 5% steps along the last radial increment. A decrease in the radial lumen diameter of about 50% was observed for all stressed trees (Fig. 3a, b, c). The lumen diameters, plotted against the absolute distance from pith to bark (Fig. 3b) indicate extreme reaction of HL to drought stress. Radial lumen diameters in the region of the last 90–95% of the increment significantly decreased due to drought in all species. Still, drought-stressed EL had significantly larger lumens than stressed HL and JL (Fig. 3a). In 90–95% of the increment, cell wall thickness indicated a tendency for higher values under drought, especially for HL (Fig. 3d, e, f) [30].

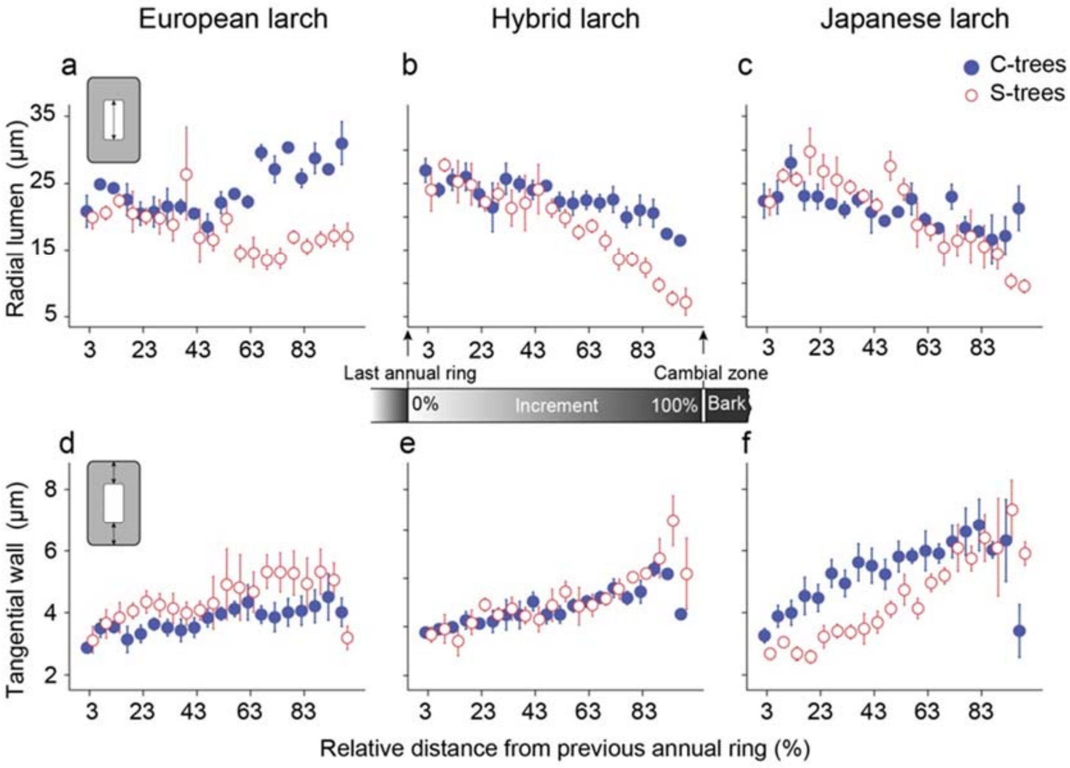

Fig. 3 Anatomical changes in 5% steps of the 2015 increment of European, hybrid, and Japanese larch trees are shown for drought-stressed trees (S-trees) in comparison to control trees (C-trees). Each stepwise mean value of radial lumen diameter of European larch (A), hybrid larch (B), and Japanese larch (C), and tangential wall thickness of European larch (D), hybrid larch (E), and Japanese larch (F) is indicated. See [30] for experimental details.

Towards the end of the experiment, the wood produced was denser, as smaller lumen diameter and thicker cell walls in stressed trees indicate (Fig. 4). The interpretations proposed for these structural changes are that transition wood formed early and had a higher hydraulic safety than earlywood and latewood. Intra-annual density fluctuations, such as the formation of a “false ring” were observed [30].

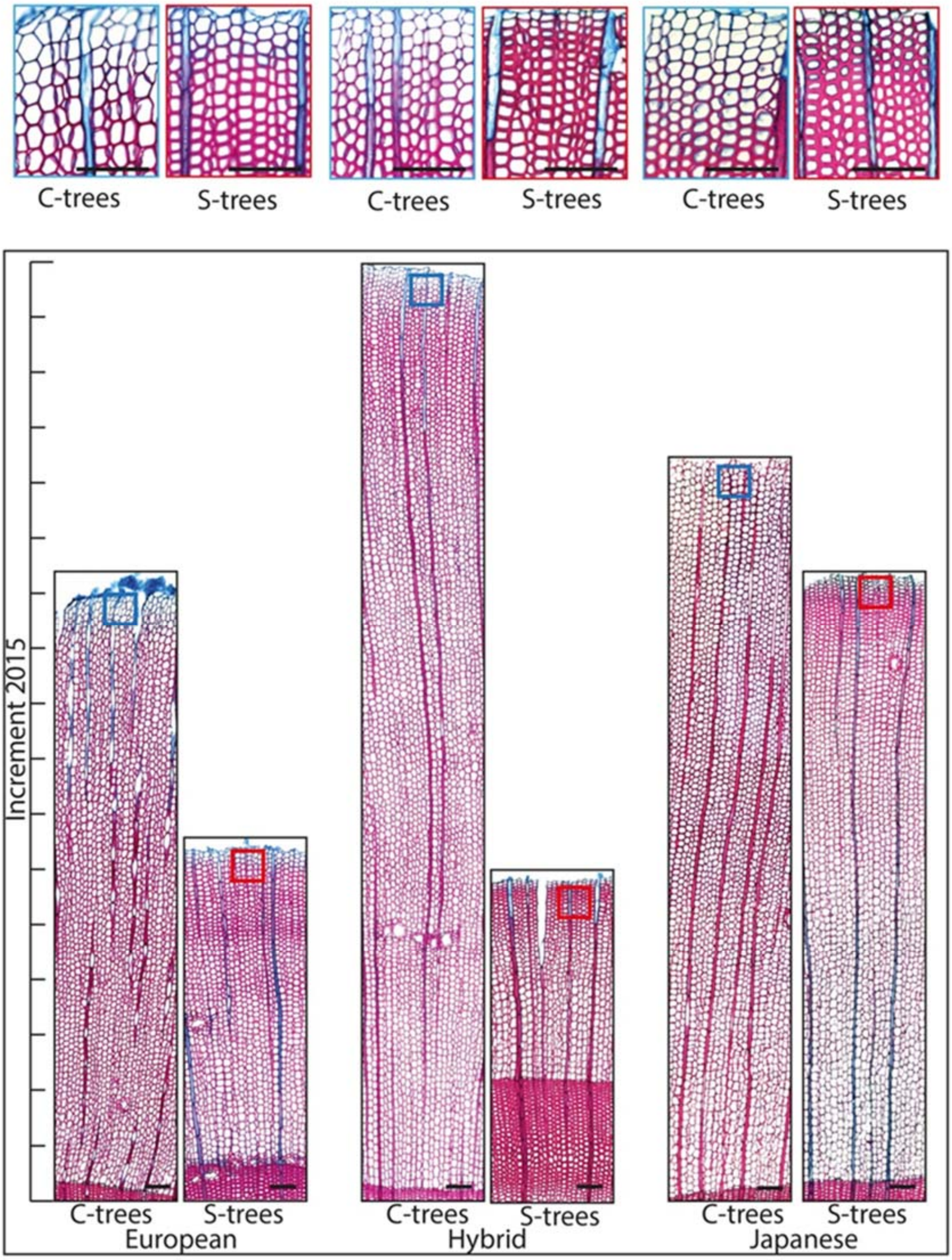

Fig. 4 Light micrographs of the wood increment 2015 of control trees (C-trees) and drought-stressed trees (S-trees) of European larch (EL), hybrid larch (HL), and Japanese larch (JL). The boxed regions in each micrograph are presented at high magnification. The scale bar is 100 µm. Sample and experimental details in [30].

3.2. Is the different growth behavior of the three larch species (European, Hybrid, Japanese) reflected in different hydraulic vulnerabilities, assessed by constitutive wood anatomy?

Trees adapt several strategies to modify their wood composition and structures, such as pit structure, conduit wall reinforcement, cell wall lignification and lignin composition, to prevent or minimize cavitation [29, 80, 93, 94]. The conduit wall reinforcement is the cell wall thickness to span ratio $(t/b)^2$ that positively correlates with embolism resistance. Decreasing lumen diameter or increasing wall thickness leads to hydraulic failure resistance [29]. We observed smaller tangential lumen diameters in European larch (EL), which indicated that EL had a higher theoretical hydraulic safety against implosion of the tangential cell walls $((t_t/b_t)^2)$ (Fig. 5a) compared to other species, and thus was superior in terms of resistance against cavitation [79]. There were no significant differences between Japanese larch (JL) and hybrid larch (HL) in lumen diameter or cell wall thickness traits in the wood formed before the start of the drought stress. In addition, there were no significant differences between species in conduit cell wall reinforcement of the radial cell walls $((t_r/b_r)^2)$ (Fig. 5b). Pit structural modification is another determining factor with respect to cavitation resistance [94]. The results of our study, comparing pit membrane, aperture, torus diameters and torus overlap, showed that there were no significant differences between the species. Our data indicate that juvenile larch wood is relatively safe hydraulically compared to other conifer species [94]. We observed a higher torus overlap in JL followed by EL and HL as a trend [30]. However, regarding conduit wall reinforcement in the tangential direction, JL was the most cavitation-sensitive species. Thus, we interpret these features to be regarded as a compromise between this species' hydraulic efficiency and safety. The pit cavity area was significantly smaller in EL than in HL or JL, which could be related to higher hydraulic security. A proxy for cavitation vulnerability has not tested this anatomical trait [30]. The results of the anatomical comparison suggest that EL with structural properties such as higher conduit wall reinforcement and smaller pit cavity size had increased hydraulic safety, which comes at a cost of slower growth. Our results are in line with other studies suggesting that EL is an anisohydric species, which can cope with lower water potentials than isohydric species [95-99]. EL prevents cavitation by keeping stomata open at greater negative water potentials than JL or HL because cavitation happens at lower water potentials [29]. With two different strategies, the transpiration efficiency in JL and HL was increased under controlled drought. The reason for this is that in HL, there was a substantial decrease in transpiration per leaf surface, while in JL; there was a decrease in the leaf surface. HL appeared the most reactive to soil water availability with physiological responses such as a greater decrease in transpiration rate, lower relative water contents in sapwood, and early production of denser wood compared to other species [30].

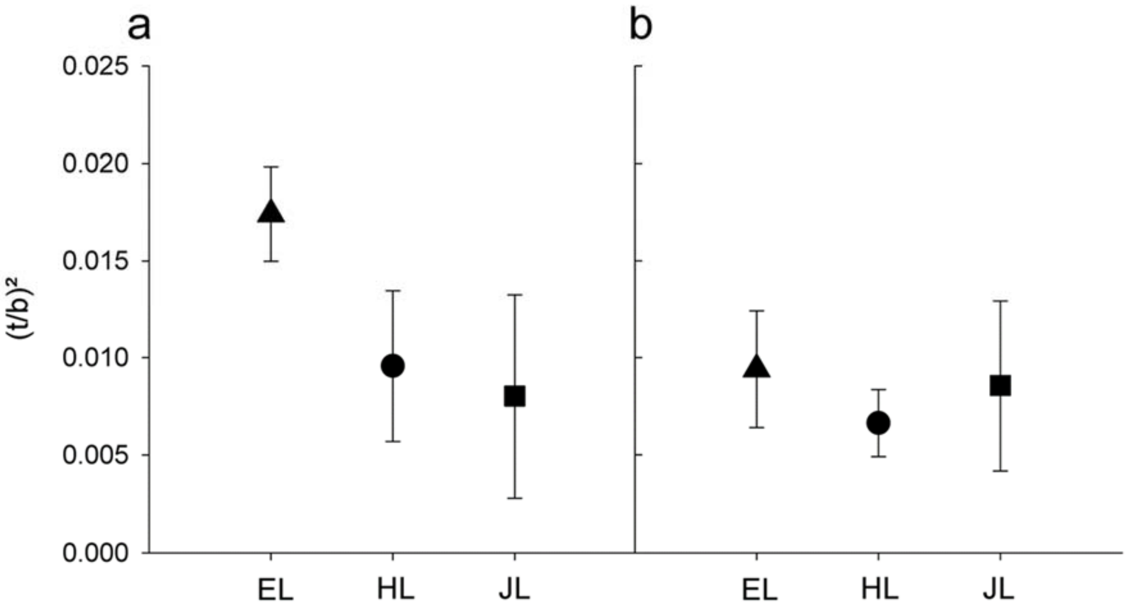

Fig. 5 shows conduit wall reinforcement in the tangential direction (A) and the radial direction (B) in the first formed earlywood tracheid of European larch (EL), hybrid larch (HL), and Japanese larch (JL). Whiskers indicate the standard deviation. See [30] for sample and experimental details.

3.3. Does drought stress influence cell wall lignification?

We undertook a comparison of the lignification between control and drought-stressed larch species. With respect to plant strategies for adaptation to environmental stresses, plant's physiological and biochemical responses to drought stress conditions at cellular and organism levels differ [16]. The species, genotype, duration, and intensity of stress are determinants of sensitivity and time response in plants. In other words, the intensity of the reaction depends on the intensity of the stress, tree species, and intraspecific and even provenance differences [88, 100, 101]. Plants experiencing drought conditions overproduce reactive oxygen species (ROS), which prevent growth and photosynthetic functions and have been linked to programmed cell death, which can also lead to increased lignification [101]. Lignin in cell walls is a polyphenolic polymer, which is responsible for the mechanical strength, and also forms a barrier to water permeability in softwood tracheids [102]. The other secondary cell wall components are cellulose and hemicellulose. Cellulose microfibrils are the main load-bearing structures, which are embedded in the hemicellulose-lignin matrix [54, 103]. Conifer wood consists mainly of one type of cell called tracheids, which are long tubular cells with lignified cell wall walls. Tracheids consist of a three-layered secondary cell wall surrounded by a primary wall and the middle lamella (compound middle lamella). The three layers of the secondary wall S1, S2, and S3 differ in their thickness and microfibril orientation. They may also vary in lignin concentration [24, 104-106]. Secondary cell walls, as an essential part of the xylem structure, consist of cellulose (40-50%), hemicellulose (20–30%), and lignin (20–35%) [49, 111]. Structurally, tracheid cell walls are differentiated into a middle lamella, which acts as a glue between adjacent cells and keeps them connected, a thin primary wall and a thick three-layered secondary wall. We compared the structure and distribution of lignin on a micro-scale in tracheid cell walls of European larch (EL), Japanese larch (JL), and hybrid larch (HL) subjected to controlled drought, using Raman confocal microscopy. Several studies have provided information on the effect of climate signals on the xylem cell wall chemistry and biopolymer composition, such as Zahner [107]. The studies have shown that tree water status has an influence on tracheid dimensions in conifers. In addition, thicker cell walls of the xylem in the stress-treated plants have been studied using histochemical, biochemical, and gas chromatography-mass spectrometry (GC-MS) approaches [108-110]. Because it is often difficult to differentiate middle lamella and the primary wall, particularly at the light microscope level, together these cell wall regions are described as the compound middle lamella (CML) (Fig. 6). On a European larch wood cross-section integration over bands at 1600 cm $^{-1}$, 1097 cm $^{-1}$, and 2900 cm $^{-1}$ respectively visualize the cell corner (CC) together with compound middle lamella (CML), the tangential S2 layer and the overall S2 layer (Fig. 6 b). The high signal of the 1097 cm $^{-1}$ band only in the x-direction shows the high cellulose microfibril angle (MFA) relative to the fiber axis, which is because the alignment of cellulose fibrils with a gentle helical slope (S-layer) leads to appear the C O–C bonding of the cellulose at the cross-section [48, 49]. Lignification of the cell wall begins in the middle lamella, progressing across the cell wall towards the lumen. The middle lamella-primary cell wall region has consistently been found to be the most highly lignified part of the cell wall, with reported minor variations. Cell death (via apoptosis) occurs after completion of cell wall lignification across the secondary cell wall, including the S3 layer, the innermost part of the cell wall [111, 112]

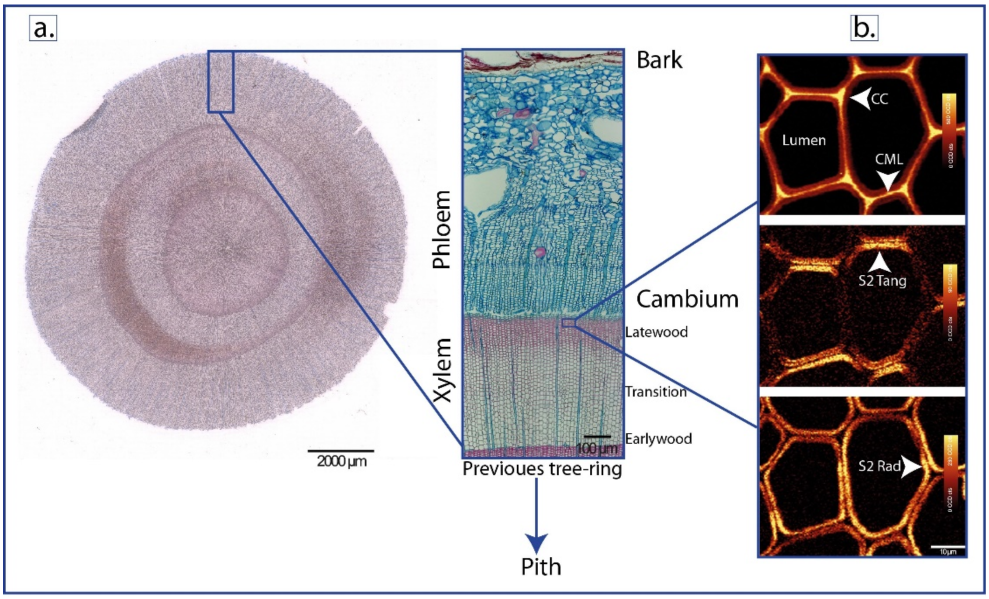

Fig. 6 Tree-rings in the wood cross-section of Larch. (A), light micrograph of a cross-section of the last tree ring of European Larch (EL) normal wood, showing a cambium zone located between the latewood and the phloem. (B) Raman confocal images of a cross-section of European larch wood showing middle lamella and primary cell wall (CML),cell corners (CC) (1600 cm $^{-1}$ band integration), cell wall emphasized in tangential direction (1097 cm $^{-1}$ band integration) and the secondary cell wall (S2) based on (2900 cm $^{-1}$ band integration).

Characteristics, such as the number, size, wall thickness, and lignin composition of cells in the same tissue do not vary much, but can be impacted by age, and biotic and environmental stresses [112, 113]. Numerous studies have commented on the effect of the environment on lignification, such as Gindl & Grabner [114], indicating that there is a variation in lignin concentration in the secondary cell wall of finishing cells of latewood tracheid's in autumn under alpine growth conditions. Conifer tree rings consist of thin walled earlywood (EW) formed in the spring and thick walled latewood (LW) formed in the summer. Earlywood tissues in the sapwood are responsible for the transport of water taken up from roots, and the upward movement of water within xylem conduits is driven by the transpiration pull. In contrast, LW cells mainly function in providing mechanical support to tree organs. The cambium (the lateral meristem) produces secondary xylem and phloem tissues through the division of its cells [115]. The cambial derivative cells that become part of the secondary xylem undergo expansion growth prior to secondary wall deposition. In our study, we focused on lignification as a dynamic physiological process to understand the effect of drought stress, knowing that environmental factors can affect cell wall lignification. We tracked the lignin distribution of tracheids in cross-sections in their wet native state by integration of the 1600 cm $^{-1}$ band on the 10-12 cells towards the cambium zone in every larch species and treatment (Fig. 7a, b, and c). As expected, a trend in decreasing lignification is found towards the cambial zone. In the control larch trees (C) high lignin intensity (pink) highlights mainly CML and middle lamella and the secondary cell walls seem to be very thin. In drought stressed trees, thicker lignified cell walls are observed in these 10-12 cells, especially in Japanese larch (Fig. 7c). The total average spectra of each sample were extracted and normalized on the 380 cm^{-1} cellulose band to compare lignin amount (yellow highlights). The two strongest bands of lignin in the Raman spectrum are at 1600 cm^{-1} and 1657 cm^{-1}. The strong band at 1600 cm^{-1} represents two ring deformation modes without overlapping carbohydrates in the cell walls. In addition, another characteristic band at 1657 cm^{-1} is a shoulder, which represents the ring-conjugated C = C stretch of coniferyl alcohol and a C = O stretch of coniferyl aldehyde [53].

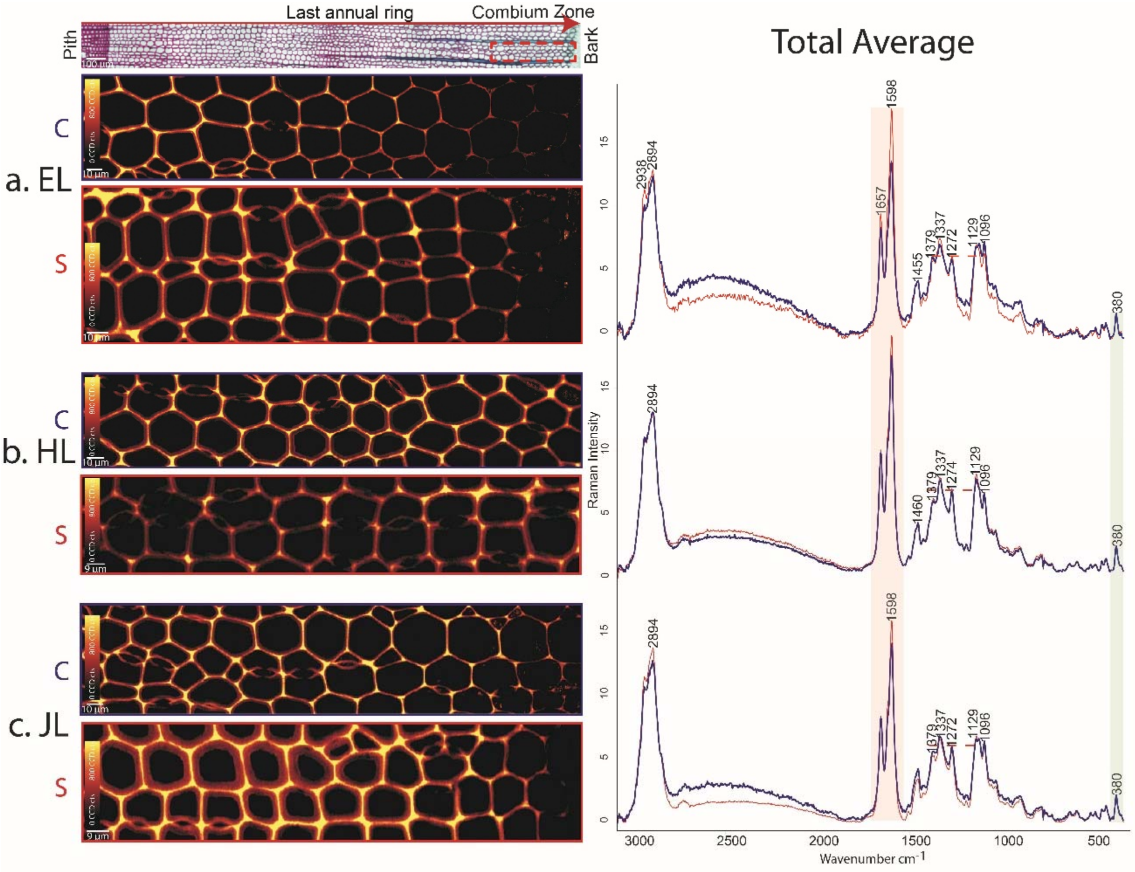

Fig. 7 Raman images of the cross-section in the latewood (LW) of the last tree ring in European larch (EL) (A), Hybrid Larch (HL) (B), and Japanese Larch (JL) (C). In addition, total average Raman spectra of the selected area around the cambium zone in three species of larch were extracted to compare lignin changes between control(C) and stress(S) trees based on the band at 1600 cm^{-1} (lignin).

Comparison between total average spectra of control and stressed EL and JL showed that stressed trees have higher lignin with increasing intensity at the 1600 cm^{-1} band. Furthermore, EL control had a different intensity ratio between bands at 1129 cm^{-1} and 1096 cm^{-1} compared to stressed (EL) because of the different cellulose orientation (Fig. 7a). Moreover, two other bands at 1069 cm^{-1} and 1273cm $^{-1}$ (lignin) in the total average Raman spectrum were varied (Fig.7a). These ratios characterize lignin distribution changes in the secondary wall. Repeating studies confirmed that the lignin distribution pattern through the annual ring of conifers is formed by a decrease from the first EW cell to the EW-LW boundary and a rise towards the end of the annual increment. The last LW cells in tree line Norway spruce have high values and alteration in lignin, which have been explained by temperature variations [114].

Lignification provides rigidity and strength to conduit walls needed to withstand the forces of the negative pressure arising during water transport [93, 116, 117]. Pettermann *et al.* [93] showed that hydraulic safety in conifers increased with a greater thickness to span ratio in a tracheid, mainly achieved by a reduction in the lumen instead of an increase in wall thickness. We could show that the Raman image would allow us to capture changes in lignin distribution in cell walls induced by the drought as a strategy for trees to cope with drought stresses. It has been reported that drought stress induces biochemical and morphological responses when the water shortage rate exceeds the critical level [118].

3.4. Is Raman imaging an appropriate tool to probe the microchemistry of the cuticle and epidermal layer of spruce needles? (Paper 2)

This study revealed that chemical components could be tracked in native spruce cuticles by using high-resolution (~ 300 nm) confocal Raman spectroscopy (CRM). We applied two different approaches to analyze the acquired hyperspectral data cubes: univariate and multivariate data analysis. Chemical images of the cuticle of Norway spruce were generated using band integration (univariate approach) (Fig. 2 in [39]) and multivariate approaches such as cluster analysis (Fig. 3 in [39]) and the unmixing approach Non-negative matrix factorization (NMF) (Fig. 4 in [39]). This approach is able to find the most pure aromatics, lipids, carbohydrates, and minerals at once and visualize the chemistry in context with microstructure. Beyond this, by changing laser polarization it was possible to probe the direction of the distribution of the molecule in the cuticle structure with respect to the plant surface (Fig 5 in [39]). The methods commonly used to study cuticles' chemistry and structure, such as SEM, TEM, and extraction procedures, are destructive in nature and can alter cuticle composition and molecular architecture. Furthermore, methods, such as LM, SEM, TEM, and AFM provide mainly morphological and structural information [4, 50, 61]. Most biochemical techniques such as gas and liquid chromatography (GC and LC) alone or combined with mass spectrometry (GC and LC-MS) and liquid chromatography-mass spectrometry (UHPLC-MS) involve destructive chemical analyses through extraction and washing procedures and are time-consuming, limited in mobility, and intensive in labor. Another issue is environmental pollution from the chemicals used, which require special handling and disposal [32, 34, 39, 42, 119, 120]. Raman confocal microscopy (RCM) is a non-destructive method for micro-chemical analysis of plant cells and tissues in their native state and at high resolution [39, 77]. One of the most important advantages of Raman point-by-point mapping is access to the molecular fingerprint at every pixel and average, cluster, and endmember spectra for detailed analysis and verification in addition to the calculated chemical images. The extracted cuticle spectra were effective in interpreting the chemical composition of distinguished layers, and interfaces of the cuticle of spruce needles.

3.5. What is the most suitable sample preparation, experimental, and data analysis approach for Raman imaging of spruce needles?

The Raman imaging was experimented with using both 532 nm and 785 nm excitation, but because of the high sample fluorescence with 532 nm, we settled on using 785nm. However, we used 532 nm measurements to show the potential of laser polarization to regain the setout of the molecules in the outer region of the cuticle. Our published work (Fig. 5 in [39]) showed the orientation of waxes and coumaric acid in the cuticle. The aliphatic chains and aromatic rings in the wax layer are arranged perpendicular to the surface, but compounds in the cuticular layer have an amorphous structure and are without orientation [39].

Moreover, we used two approaches to analyze the data, including univariate (band integration) and multivariate data analysis (cluster analysis and non-negative matrix factorization). The advantage of the multivariate data analysis method is that it simultaneously analyzes the whole wavenumber region (hyperspectral data cube) instead of focusing on selected bands. All three data analysis methods showed that the waxy layer is distinguishable from the underlying cuticle. In addition, the adjacent periclinal epidermal layer is chemically different and thus differentiated from the rest of the epidermis. Greater details and a more comprehensive picture of the cuticle of Norway spruce needles can be found in [39]. Univariate data analysis is a fast method used in almost every Raman imaging study. It works well as long as the different components do not have overlapping or weak bands, and their characteristic bands can be tracked. The second method was cluster analysis, which groups the spectra according to similarity. The isolated cluster average spectra show the chemistry of the identified chemically homogenous regions but do not necessarily explore specific components. The third method was NMF-analysis, which computes a linear combination of endmember spectra to represent the spectra at every pixel. The spectra of the waxy layer from the three approaches obtained were very similar. The unmixing approach could not find a "pure" wax spectrum within all the pixels because of the close conjugation of lipids and coumaric acid. Raman imaging gives insights into cuticle chemistry in context with microstructure [39] and results in new information-rich cuticle models of different plant species [121].

3.6. Can we track differences between resistant and rust infected spruce needles in microchemistry by Raman imaging?

Ganthaler *et al* have reported differences or fluctuations in secondary metabolites between healthy and *Chrysomyxa rhododendri* infected Norway spruce using chemical approaches, such as UHPLC-MS [34]. We used Raman imaging and compared the spatial distribution of the main cuticle components in needle cross sections from trees with different susceptibility to the above-mentioned fungus. True Component Analysis was applied to find and extract the purest spectra representing the main cuticle components (Fig. 9). In the next step, the purest components out of all datasets were selected and used as reference spectra in a basis analysis on datasets of needles with different susceptibility (Fig. 10). The cuticle consists of cuticular waxes and the cutin matrix and in some cases cutan, phenolics and polysaccharides originating from the epidermal cells [39, 122]. Cuticular waxes consist of a long (20–60 carbon atoms) chain of aliphatic compounds like alkanoic acids, primary and secondary alkanols, n-alkanes, alkyl esters, pentacyclic triterpenoids, and sterols [123]. Two characteristic bands at 1122 and 1063 cm $^{-1}$ represent these aliphatic chains in the Raman spectra as seen in the extracted wax spectrum (Fig. 9a, yellow spectrum) [44]. The cutin matrix of the cuticle consists of long-chain ω-hydroxy alkanoic acids, which are esterified into a complex polymeric network with linear and branched domains by primary and secondary ester or bonds with mid-chain lengths of 16 and 18 carbon atoms, like hydroxyl, carbonyl, and epoxy groups [122]. The cutin matrix has a typical band at 1440 cm $^{-1}$, representing CH_2 bend in fatty acids (Fig. 9 a, green spectrum). The second strong Raman band at 1608 cm^{-1} indicated aromatic components associated with cutin, as this band is assigned to aromatic rings in conjugation with C=C/C=O. The band at 1567 cm^{-1} and 1632 cm^{-1} point to flavonoids and phenolic acids, respectively, as shown in paper 2 [39]. Flavonoids are phenolic compounds with aromatic hydrocarbon rings and at least one hydroxyl group and are derived as purer components in the analysis; although again associated with cutin (Fig. 9b, green spectrum) and phenolic acids (Fig. 9 b, red spectrum). The band at 1605 cm^{-1} comes from the aromatic ring and is besides flavonoids also strong in phenolic acids. These can be characterized by additional bands at 1636 cm^{-1} and 1171 cm^{-1} (Fig. 9 b, violet spectrum). Pointwise accumulations have been shown with characteristic Raman bands at 1490 cm^{-1} and 1463 cm^{-1}, which can be assigned to calcium oxalate (Caox) deposits; the different band ratios point to different crystal orientations (Fig. 9 c). The underlying epidermal cell walls are based on carbohydrates (cellulose, hemicellulose, pectin) with characteristic bands at 1378 cm^{-1}, 1120 cm^{-1}, 1095 cm^{-1}, and 380 cm^{-1} (Fig. 9d, blue spectra) and lignin with a typical band at 1657 cm^{-1}, 1269 cm^{-1} beside the strong aromatic ring stretching at 1600 cm^{-1} (Fig. 9 d, turquoise).

In the following, the above-described component spectra were used in a basis analysis to compare Norway spruce needle's from two neighbored trees (PRA 1), one susceptible and one resistant to the fungus (Fig. 10a). The comparison of the distribution map showed that the lipid components layer between resistant and susceptible needles in the cuticle zone are similar, although the waxy layer looks more discontinuous in the susceptible needle (Fig. 10 b). As this waxy layer is very tiny and on the very outside this can also be an effect of sample preparations, as we have not observed such discontinuities in all other samples. Nevertheless, if such discontinuous waxy layers are present in the native state, they might be a weak point and to clarify this the surface of native susceptible cuticles needs to be checked by scanning electron microscopy. The three aromatic reference components have shown different amounts and distributions between healthy and susceptible (Fig. 10 c). More pure phenolic acids are shown in purple color (Fig. 10 b) and have a higher intensity in the healthy needle in comparison with the infected needle. Phenolic acids accumulate in the anticlinal ridges towards the epidermal layer but are also found as a layer below the waxy layer in the healthy cuticle. Flavonoids accompanied by phenolic acids are shown in red color and are found with higher intensities in healthy needles, especially periclinal on top of the epidermal layers. In contrast, the purest flavonoid component (light green) fit more in the susceptible needle than in the healthy needle. The Raman imaging approach showed the complex nature of aromatics in the cuticles and that they might play a role in the defense mechanisms of needles against fungal attacks. The complexity on the microscale makes comparable analysis quite difficult as e.g. higher fluorescence background in the susceptible needle through a chance in the aromatic composition can influence analysis in the way that minor components with lower intensity bands become overlapped. On the other hand, Raman imaging has the advantage that not the overall chemical composition of the whole cuticle or even needle is assessed by extraction, but really in context with the microstructure. The fact that our pixels of 300 nm showed still rather mixtures than completely pure components (Fig. 9), suggests an intimate association of phenolic and flavonoids with cutins and polysaccharides. Similar conclusions have also been drawn from tomato cuticles [124].

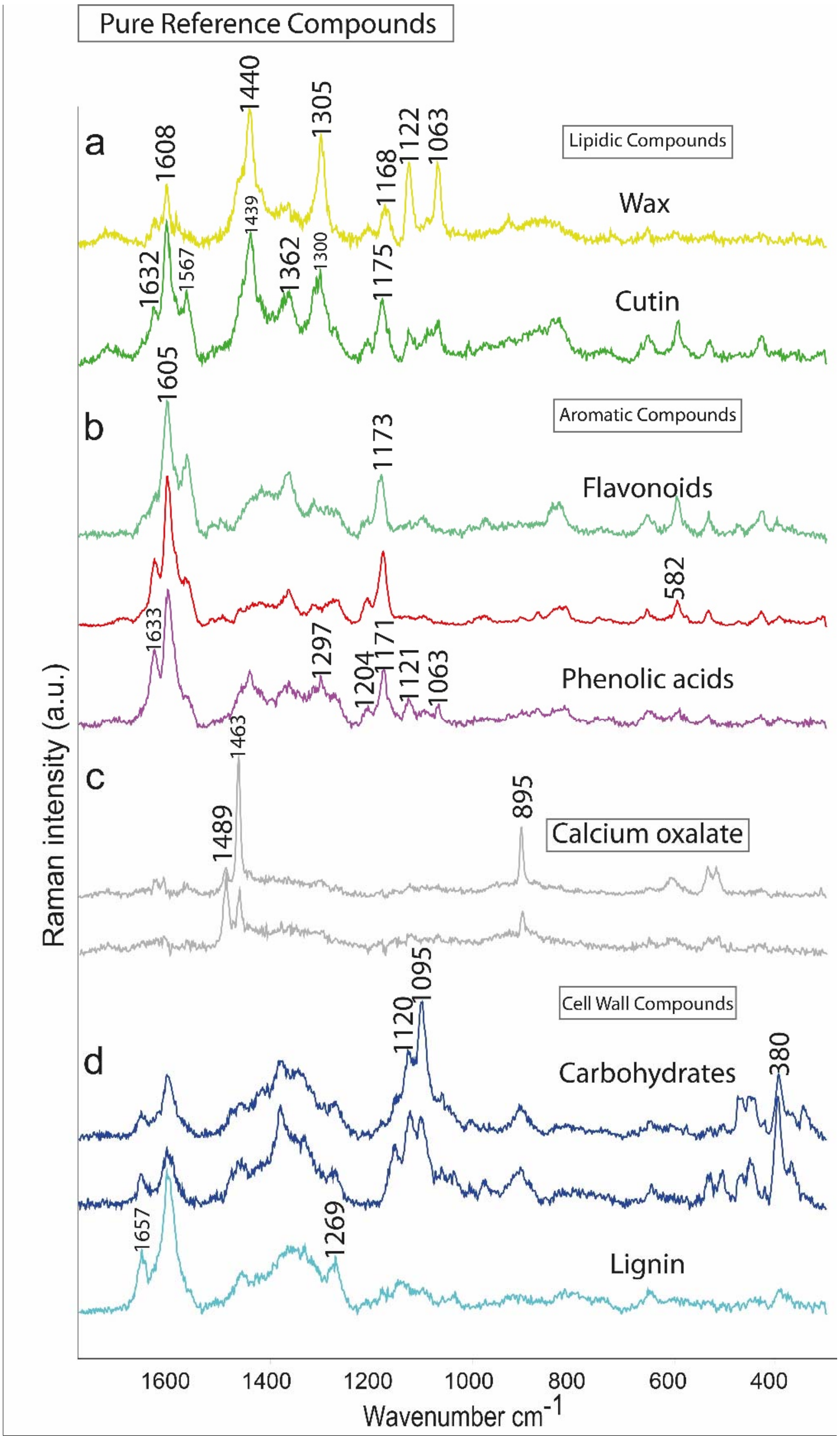

Fig. 9. Tracking the chemical composition, intensity, and spatial distribution of cuticle components in Norway spruce needles by True Component Analysis. (A), extracting the purest average component spectra as reference spectra including the outer lipidic components (waxy, and cutin layer), (B) aromatics components (flavonoid and phenolic acid), (C) Calcium oxalate, (D) and cell wall components (carbohydrates and lignin).

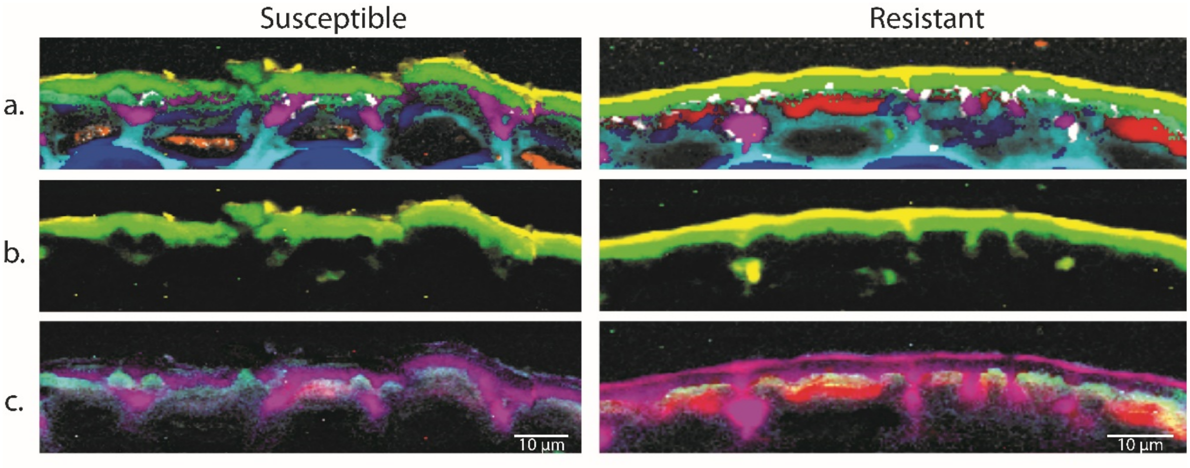

Fig. 10 shows the distribution of cuticle and epidermal layer components of PRA 1 needles with different degrees of susceptibility assessed by basis analysis using the component references shown in Fig. 9. (A), Overlay of all components (B), the distribution of lipidic components (wax (yellow), cutin (green)) throughout the cuticle and epidermal layer. (C), the distribution of aromatic components (flavonoids in light green, flavonoids and phenolic acids in red and phenolic acids in purple) varies between susceptible and resistant needles.

While many studies have confirmed the existence of phenolic substances constitutively in healthy needles, inductive resistance in trees after infection leads to changes in the concentration of phenolic components, which vary depending on the host-pathogen interaction [32, 34, 39, 125]. Ganthaler *et al*. 2017 [34] showed that the concentration of several flavonoids and resveratrol increased after infection with *Chrysomyxa rhododendri* in the needles of Norway spruce, while picein and shikimic acid were reduced. Our Raman imaging results confirm this trend by visualizing more phenolic acids in the healthy needles (purple, Figure 10). Furthermore, phenolic acids are intimately associated with flavonoids (red color), whereas purer and therefore probably easier extractable are flavonoids (light green) in susceptible needles. Phenolic components are secondary metabolites that play a role in both constitutive and induced defense strategies [126].

Raman imaging could be helpful in the detection of concentration changes of aromatic components in the early stages of infection in the first line of the defense system in the plants when they face the pathogen. The method used in our work was applied for detailed imaging studies on needle microsections. Nevertheless, in the future handheld Raman spectrometers could be used for a fast and non-destructive study of the outer surface of the needles. Such studies can have practical benefits, saving time, energy, and money, and can help improve the forest protection system, particularly in breeding trees against pathogens. Raman spectroscopy has been considered a non-destructive method in plant disease detection. There are many reports on successful application of Raman spectroscopy in the diagnosis and analysis of plant diseases, such as identifying citrus infected by bacteria, analyzing tomatoes inoculated with tomato yellow leaf curl Sardinia virus, and tomato spotted wilt virus [127, 128]. Being fast, specific to a particular disease due to noncontact scattering, and sensitive for detection at the early onset of the symptoms; being labeled free means no need for fluorescent marker molecules are some of the advantages of Raman spectroscopy [129-132]. The other distinctive advantage of Raman is the low-intensity bands of the water when water-based material, or other polar solvents analyzing without interfering with its structure [48, 50, 63, 130]. This technique with a rapidly developing technology has been applied to analysis in a wide range of basic and applied science disciplines, such as food chemistry and adulteration, body fluid, illegal drug quantification, electrochemistry, fluid body, and forensics [119, 130, 133]. However, the most critical challenge faced in the Raman spectroscopic analysis is the fluorescence of biological samples when lasers in visible light range are used. Fluorescence excitation can lead to interference with the Raman signal. Additionally, the high intensity of excitation radiation can cause sample decomposition [50]. Therefore, for accuracy of results these limitations have to be overcome in Raman spectroscopic analysis of fluorescent objects.

3. Conclusion

Regarding the abiotic stress response, this thesis added new data on the different adaptations and reactions to drought stress within the genus *Larix*, by investigating three different larch species (EL, JL, and HL). EL took over anisohydric behavior under drought stress with slower growth and hydraulically safer wood, whilst JL and HL have an isohydric strategy with less safe wood design and stronger stomatal control. Transpiration efficiency increased in the latter two by different mechanisms: HL reduced strongly transpiration per leaf surface, whiles JL reduced the leaf surface area. HL with the highest decrease in transpiration rate and lower relative water contents in sapwood reacted most to soil water availability and induced latewood formation earlier than the other two species. Additionally, confocal Raman confocal microscopy was used for microscale analysis of the composition of the three species. The actual stage of lignification was visualized in the last tree ring cells towards the cambium and all three species showed higher lignin levels as a drought reaction.

All presented experimental approaches yielded detailed cellular information on drought responses in different larch species on the tree level and are therefore useful in selective breeding for tree improvement and plantation establishment. The higher drought plasticity in HL was hypothesized to be inherited from JL and its higher growth under drought together with better disease resistance supports its inclusion in pure and mixed lowland plantations. With the anisohydric strategy under drought condition EL could be shifted to higher elevations or more northern regions under climate change.

For biotic stress responses, the outer plant surface, the cuticle, is of utmost importance. The feasibility of Raman imaging and multivariate data analysis approaches to investigate the chemistry of the cuticle in the native state on the microscale was proven on Norway spruce needles. For the first time we visualized aromatic components and minerals within the cuticle, in association with lipidic components and carbohydrates. Even preferred orientation of the molecules was derived in the crystalline wax layer with the help of laser polarization experiments. Aliphatic chains and coumaric acid molecules were revealed to be aligned perpendicular to the plant surface in this outer layer. Calcium oxalate crystals were visualized at the interface between the lipidic cuticle and the carbohydrate rich epidermis. In the upper periclinal epidermal cell wall, strong Raman signals of flavonoids were detected, while in the anticlinal inclusions phenolic acids accumulated. A preliminary comparison of spruce needles sampled from two neighbored trees, one resistant and on sustainable to rust infection, suggests higher phenolic acid content and flavonoids content in resistant needles. The anticlinal peg inclusions were more enriched in phenolic acids as well as the periclinal epidermal wall more impregnated with phenolic acids and flavonoids. These detailed microchemistry studies reveals the cuticle as a barrier impregnated with phenolic substances to get hydrophobised and be better protected against biotic and abiotic threats. Future studies could include handheld Raman instruments directly on the needle or razor blade cut needle cross section to come up with a fast and non-destructive cuticle composition to predict resistance and survival and select the fittest and best-adapted trees for future forests in our changing environment.

5. Literature

1. Madlung, A. and L. Comai, *The effect of stress on genome regulation and structure.* Ann Bot, 2004. **94**(4): p. 481-95.
2. Lichtenthaler, H.K., *The stress concept in plants: an introduction.* Ann N Y Acad Sci, 1998. **851**: p. 187-98.
3. Gull, A., A.A. Lone, and N.U.I. Wani, *Biotic and Abiotic Stresses in Plants*, in *Abiotic and Biotic Stress in Plants*. 2019, IntechOpen.
4. Zhang, Y., et al., *Plant Disease Monitoring With Vibrational Spectroscopy*, in *Vibrational Spectroscopy for Plant Varieties and Cultivars Characterization*, J. Lopes and C. Sousa, Editors. 2018, Elsevier. p. 227-251.
5. Ahmad, P. and M.N.V. Prasad, *Abiotic stress responses in plants: metabolism, productivity and sustainability*. 2011: Springer Science & Business Media.
6. Potters, G., et al., *Stress-induced morphogenic responses: growing out of trouble?* Trends Plant Sci, 2007. **12**(3): p. 98-105.
7. Wu, S., L. Shan, and P. He, *Microbial signature-triggered plant defense responses and early signaling mechanisms.* Plant Sci, 2014. **228**: p. 118-26.
8. Schwessinger, B. and P.C. Ronald, *Plant innate immunity: perception of conserved microbial signatures.* Annu Rev Plant Biol, 2012. **63**(1): p. 451-82.
9. Freeman, B.C. and G.A. Beattie, *An overview of plant defenses against pathogens and herbivores.* The Plant Health Instructor, 2008.
10. Kashyap, B. and R. Kumar, *Sensing Methodologies in Agriculture for Monitoring Biotic Stress in Plants Due to Pathogens and Pests.* Inventions, 2021. **6**(2): p. 29.
11. Shafqat, W., et al., *Effect of Three Water Regimes on the Physiological and Anatomical Structure of Stem and Leaves of Different Citrus Rootstocks with Distinct Degrees of Tolerance to Drought Stress.* Horticulturae, 2021. **7**(12): p. 554.
12. Tyree, M.T. and J.S. Sperry, *Vulnerability of xylem to cavitation and embolism.* Annual review of plant biology, 1989. **40**(1): p. 19-36.
13. Hillabrand, R.M., et al., *Functional xylem anatomy of aspen exhibits greater change due to insect defoliation than to drought.* Tree Physiol, 2019. **39**(1): p. 45-54.
14. Fonti, P., et al., *Studying global change through investigation of the plastic responses of xylem anatomy in tree rings.* New Phytol, 2010. **185**(1): p. 42-53.
15. Qin, F., K. Shinozaki, and K. Yamaguchi-Shinozaki, *Achievements and challenges in understanding plant abiotic stress responses and tolerance.* Plant Cell Physiol, 2011. **52**(9): p. 1569-82.
16. Yang, X., et al., *Response Mechanism of Plants to Drought Stress.* Horticulturae, 2021. **7**(3): p. 50.
17. Jeandroz, S. and O. Lamotte, *Editorial: Plant Responses to Biotic and Abiotic Stresses: Lessons from Cell Signaling.* Front Plant Sci, 2017. **8**(1772): p. 1772.
18. Rossi, S., et al., *Predicting xylem phenology in black spruce under climate warming.* Global Change Biology, 2011. **17**(1): p. 614-625.
19. Piermattei, A., et al., *Functional Relationships of Wood Anatomical Traits in Norway Spruce.* Front Plant Sci, 2020. **11**: p. 683.
20. Zhang, H. and U. Sonnewald, *Differences and commonalities of plant responses to single and combined stresses.* Plant J, 2017. **90**(5): p. 839-855.
21. Borah, N., P.K. Borua, and S.P. Saikia, *Effect of water stress on morphological, physiological, biochemical and molecular responses of plants: A.* 2020.
22. Brodribb, T.J. and H. Cochard, *Hydraulic failure defines the recovery and point of death in water-stressed conifers.* Plant Physiol, 2009. **149**(1): p. 575-84.
23. Tyree, M.T. and M.H. Zimmermann, *Xylem Dysfunction: When Cohesion Breaks Down*, in *Xylem Structure and the Ascent of Sap*. 2002, Springer Berlin Heidelberg: Berlin, Heidelberg. p. 89-141.

24. Růžička, K., et al., *Xylem development - from the cradle to the grave.* New Phytol, 2015. **207**(3): p. 519-35.
25. Chen, K., et al., *MdMYB46 could enhance salt and osmotic stress tolerance in apple by directly activating stress-responsive signals.* Plant Biotechnol J, 2019. **17**(12): p. 2341-2355.
26. Boerjan, W., J. Ralph, and M. Baucher, *Lignin biosynthesis.* Annu Rev Plant Biol, 2003. **54**(1): p. 519-46.
27. Davin, L.B., et al., *Lignins: A Twenty-First Century Challenge*, in *Biomass Recalcitrance*. 2008. p. 213-305.
28. Tenhaken, R., *Cell wall remodeling under abiotic stress.* Front Plant Sci, 2014. **5**: p. 771.
29. Hacke, U.G., et al., *Trends in wood density and structure are linked to prevention of xylem implosion by negative pressure.* Oecologia, 2001. **126**(4): p. 457-461.
30. Sasani, N., et al., *Physiological and anatomical responses to drought stress differ between two larch species and their hybrid.* Trees, 2021. **35**(5): p. 1467-1484.
31. Walters, D. and J. Fountaine, *Practical application of induced resistance to plant diseases: an appraisal of effectiveness under field conditions.* The Journal of Agricultural Science, 2009. **147**(5): p. 523-535.
32. Trujillo-Moya, C., et al., *RNA-Seq and secondary metabolite analyses reveal a putative defence-transcriptome in Norway spruce (Picea abies) against needle bladder rust (Chrysomyxa rhododendri) infection.* BMC Genomics, 2020. **21**(1): p. 336.
33. Eyles, A., et al., *Induced resistance to pests and pathogens in trees.* New Phytol, 2010. **185**(4): p. 893-908.
34. Ganthaler, A., et al., *Foliar Phenolic Compounds in Norway Spruce with Varying Susceptibility to Chrysomyxa rhododendri: Analyses of Seasonal and Infection-Induced Accumulation Patterns.* Front Plant Sci, 2017. **8**(1173): p. 1173.
35. Ganthaler, A., et al., *Effects of the needle bladder rust (Chrysomyxa rhododendri) on Norway spruce: implications for subalpine forests.* European journal of forest research, 2014. **133**(2): p. 201-211.
36. A., D.B., *Aecidium abietinum.* Bot Z, 1879. **37**: p. 761–74 , 777–789, 801–811, 825–830, 840–847.
37. Mayr, S., et al., *Photosynthesis in rust-infected adult Norway spruce in the field.* New Phytol, 2001. **151**(3): p. 683-689.
38. Wang, X., et al., *Update on Cuticular Wax Biosynthesis and Its Roles in Plant Disease Resistance.* Int J Mol Sci, 2020. **21**(15): p. 5514.
39. Sasani, N., et al., *Raman imaging reveals in-situ microchemistry of cuticle and epidermis of spruce needles.* Plant Methods, 2021. **17**(1): p. 17.
40. Agrawal, A.A.T.S.B.E., *Induced plant defenses against pathogens and herbivores : biochemistry, ecology, and agriculture*. 1999, St. Paul, Minn.: APS Press.
41. Strack, D., et al., *Structures and accumulation patterns of soluble and insoluble phenolics from norway spruce needles.* Phytochemistry, 1989. **28**(8): p. 2071-2078.
42. Ganthaler, A., et al., *Association genetics of phenolic needle compounds in Norway spruce with variable susceptibility to needle bladder rust.* Plant Mol Biol, 2017. **94**(3): p. 229-251.
43. Bec, K.B., et al., *Principles and Applications of Vibrational Spectroscopic Imaging in Plant Science: A Review.* Front Plant Sci, 2020. **11**(1226): p. 1226.
44. Colthup, N., *Introduction to infrared and Raman spectroscopy*. 2012: Elsevier.
45. Pelletier, M.J. and C.C. Pelletier, *Spectroscopic Theory for Chemical Imaging*, in *Raman, Infrared, and Near-Infrared Chemical Imaging*. 2011. p. 1-20.
46. Wu, G., *Molecular vibration*, in *Nonlinearity and Chaos in Molecular Vibrations*. 2005. p. 1-14.
47. Gremlich, H.-U., *Infrared and Raman Spectroscopy*, in *Handbook of Analytical Techniques*. 2001. p. 465-507.
48. Gierlinger, N., *New insights into plant cell walls by vibrational microspectroscopy.* Appl Spectrosc Rev, 2018. **53**(7): p. 517-551.

49. Gierlinger, N. and M. Schwanninger, *Chemical imaging of poplar wood cell walls by confocal Raman microscopy.* Plant Physiol, 2006. **140**(4): p. 1246-54.
50. Saletnik, A., B. Saletnik, and C. Puchalski, *Overview of Popular Techniques of Raman Spectroscopy and Their Potential in the Study of Plant Tissues.* Molecules, 2021. **26**(6): p. 1537.
51. Agarwal, U.P., *Raman imaging to investigate ultrastructure and composition of plant cell walls: distribution of lignin and cellulose in black spruce wood (Picea mariana).* Planta, 2006. **224**(5): p. 1141-53.
52. Agarwal, U.P. and R.H. Atalla, *In-situ Raman microprobe studies of plant cell walls: Macromolecular organization and compositional variability in the secondary wall of Picea mariana (Mill.) B.S.P.* Planta, 1986. **169**(3): p. 325-32.
53. Agarwal, U.P., et al. *FT Raman spectroscopic study of softwood lignin*. in *Proceedings of 9th International Symposium on Wood Pulp Chemistry, Canadian Pulp Paper Association*. 1997. Citeseer.
54. Gierlinger, N., T. Keplinger, and M. Harrington, *Imaging of plant cell walls by confocal Raman microscopy.* Nat Protoc, 2012. **7**(9): p. 1694-708.
55. Butler, H.J., et al., *Using Raman spectroscopy to characterize biological materials.* Nat Protoc, 2016. **11**(4): p. 664-87.
56. Stephanos, J.J. and A.W. Addison, *Vibrational Rotational Spectroscopy*, in *Electrons, Atoms, and Molecules in Inorganic Chemistry*, J.J. Stephanos and A.W. Addison, Editors. 2017, Academic Press. p. 505-584.
57. Das, R.S. and Y.K. Agrawal, *Raman spectroscopy: Recent advancements, techniques and applications.* Vibrational Spectroscopy, 2011. **57**(2): p. 163-176.
58. Khaled, A.Y., et al., *Early detection of diseases in plant tissue using spectroscopy – applications and limitations.* Applied Spectroscopy Reviews, 2017. **53**(1): p. 36-64.
59. Agarwal, U.P., *Analysis of Cellulose and Lignocellulose Materials by Raman Spectroscopy: A Review of the Current Status.* Molecules, 2019. **24**(9): p. 1659.
60. Chenery, D. and H. Bowring, *Infrared and Raman spectroscopic imaging in biosciences.* Spectroscopy Europe, 2003. **15**: p. 4.
61. Agarwal, U.P., *1064 nm FT-Raman spectroscopy for investigations of plant cell walls and other biomass materials.* Front Plant Sci, 2014. **5**(490): p. 490.
62. Puppels, G., et al., *Description and performance of a highly sensitive confocal Raman microspectrometer.* Journal of Raman Spectroscopy, 1991. **22**(4): p. 217-225.
63. Craig, A.P., A.S. Franca, and J. Irudayaraj, *Surface-enhanced Raman spectroscopy applied to food safety.* Annu Rev Food Sci Technol, 2013. **4**(1): p. 369-80.
64. Dieing, T. and S. Breuninger, *KEY ELEMENTS OF CONFOCAL RAMAN MICROSCOPY FOR HIGH-RESOLUTION IMAGING.* Spectroscopy, 2017.
65. GmbH, W.I., *Topographic and 3D Raman Imaging.* Application Notebook, 2013. **0**(0).
66. Baiz, C.R., et al., *Vibrational Spectroscopic Map, Vibrational Spectroscopy, and Intermolecular Interaction.* Chem Rev, 2020. **120**(15): p. 7152-7218.
67. Agarwal, U., *An Overview of Raman Spectroscopy as Applied to Lignocellulosic Materials*. 1999. p. 201-225.
68. Everall, N.J., *Confocal Raman microscopy: common errors and artefacts.* Analyst, 2010. **135**(10): p. 2512-22.
69. Everall, N.J., *Confocal Raman Microscopy: Why the Depth Resolution and Spatial Accuracy Can Be Much Worse Than You Think.* Applied Spectroscopy, 2016. **54**(10): p. 1515-1520.
70. Schaeberle, M.D., et al., *Peer reviewed: Raman chemical imaging spectroscopy.* Anal Chem, 1999. **71**(5): p. 175A-81A.
71. Lee, E., *Imaging Modes*, in *Raman Imaging*, A. Zoubir, Editor. 2012, Springer Berlin Heidelberg: Berlin, Heidelberg. p. 1-37.
72. de Juan, A., et al., *Chemometric Tools for Image Analysis*, in *Infrared and Raman Spectroscopic Imaging*. 2009. p. 65-109.

73. Prats-Mateu, B., et al., *Multivariate unmixing approaches on Raman images of plant cell walls: new insights or overinterpretation of results?* Plant Methods, 2018. **14**(1): p. 52.
74. Perera, P.N., et al., *Blind image analysis for the compositional and structural characterization of plant cell walls.* Anal Chim Acta, 2011. **702**(2): p. 172-7.
75. Gierlinger, N., *Revealing changes in molecular composition of plant cell walls on the micron-level by Raman mapping and vertex component analysis (VCA).* Front Plant Sci, 2014. **5**(306): p. 306.
76. Juan, A.d., et al., *Chemometric Tools for Image Analysis*, in *Infrared and Raman Spectroscopic Imaging*. 2014. p. 57-110.
77. Sasic, S. and Y. Ozaki, *Raman, infrared, and near-infrared chemical imaging*. 2011: John Wiley & Sons.
78. Bogeat-Triboulot, M.B., et al., *Additive effects of high growth rate and low transpiration rate drive differences in whole plant transpiration efficiency among black poplar genotypes.* Environmental and Experimental Botany, 2019. **166**: p. 103784.
79. Rosner, S., et al., *Novel Hydraulic Vulnerability Proxies for a Boreal Conifer Species Reveal That Opportunists May Have Lower Survival Prospects under Extreme Climatic Events.* Front Plant Sci, 2016. **7**(831): p. 831.
80. Rosner, S., et al., *Hydraulic and mechanical dysfunction of Norway spruce sapwood due to extreme summer drought in Scandinavia.* Forest Ecology and Management, 2018. **409**: p. 527-540.
81. Evans, R., *A variance approach to the X-ray diffractometric estimation of microfibril angle in wood.* Appita Journal, 1999. **52**(4): p. 283-289.
82. Evans, R., *Rapid Measurement of the Transverse Dimensions of Tracheids in Radial Wood Sections fromPinus radiata.* Holzforschung, 1994. **48**(2): p. 168-172.
83. Fonti, P. and E.A. Babushkina, *Tracheid anatomical responses to climate in a forest-steppe in Southern Siberia.* Dendrochronologia, 2016. **39**: p. 32-41.
84. Fonti, P. and S. Jansen, *Xylem plasticity in response to climate.* New Phytol, 2012. **195**(4): p. 734-736.
85. Losso, A., et al., *Insights into trunks of Pinus cembra L.: analyses of hydraulics via electrical resistivity tomography.* Trees (Berl West), 2020. **34**(4): p. 999-1008.
86. Anfodillo, T., G. Petit, and A. Crivellaro, *Axial conduit widening in woody species: a still neglected anatomical pattern.* IAWA Journal, 2013. **34**(4): p. 352-364.
87. Pâques, L., et al., *Larches (Larix sp.) In: Pâques LE (Ed.), Forest tree breeding in Europe. Current state-of-the-art and perspectives*. 2013, Springer, Dordrecht Heidelberg, New York, London.
88. Levesque, M., et al., *Drought response of five conifer species under contrasting water availability suggests high vulnerability of Norway spruce and European larch.* Glob Chang Biol, 2013. **19**(10): p. 3184-99.
89. Schuster, R. and W. Oberhuber, *Drought sensitivity of three co-occurring conifers within a dry inner Alpine environment.* Trees (Berl West), 2013. **27**(1): p. 61-69.
90. George, J.P., et al., *Genetic variation, phenotypic stability, and repeatability of drought response in European larch throughout 50 years in a common garden experiment.* Tree Physiol, 2017. **37**(1): p. 33-46.
91. Eilmann, B. and A. Rigling, *Tree-growth analyses to estimate tree species' drought tolerance.* Tree Physiol, 2012. **32**(2): p. 178-87.
92. Lévesque, M., et al., *Growth response of five co-occurring conifers to drought across a wide climatic gradient in Central Europe.* Agricultural and Forest Meteorology, 2014. **197**: p. 1-12.
93. Pittermann, J., et al., *Inter-tracheid pitting and the hydraulic efficiency of conifer wood: the role of tracheid allometry and cavitation protection.* Am J Bot, 2006. **93**(9): p. 1265-73.
94. Bouche, P.S., et al., *A broad survey of hydraulic and mechanical safety in the xylem of conifers.* J Exp Bot, 2014. **65**(15): p. 4419-31.

95. Anfodillo, T., et al., *Tree water relations and climatic variations at the alpine timberline: seasonal changes of sap flux and xylem water potential in Larix decidua Miller, Picea abies (L.) Karst. and Pinus cembra L.* Ann. For. Sci., 1998. **55**(1-2): p. 159-172.
96. Swidrak, I., R. Schuster, and W. Oberhuber, *Comparing growth phenology of co-occurring deciduous and evergreen conifers exposed to drought.* Flora, 2013. **208**(10-12): p. 609-617.
97. Klein, T. and S. Niu, *The variability of stomatal sensitivity to leaf water potential across tree species indicates a continuum between isohydric and anisohydric behaviours.* Functional Ecology, 2014. **28**(6): p. 1313-1320.
98. Leo, M., et al., *Evaluating the effect of plant water availability on inner alpine coniferous trees based on sap flow measurements.* European Journal of Forest Research, 2013. **133**(4): p. 691-698.
99. McDowell, N., et al., *Mechanisms of plant survival and mortality during drought: why do some plants survive while others succumb to drought?* New Phytol, 2008. **178**(4): p. 719-739.
100. Lautner, S., *Wood Formation Under Drought Stress and Salinity*, in *Cellular Aspects of Wood Formation*, J. Fromm, Editor. 2013, Springer Berlin Heidelberg: Berlin, Heidelberg. p. 187-202.
101. Carrizo, I.M., et al., *Contrasting adaptive responses to cope with drought stress and recovery in Cenchrus ciliaris L. and their implications for tissue lignification.* Physiologia Plantarum, 2021. **172**(2): p. 762-779.
102. Malavasi, U.C., A.S. Davis, and M.d.M. Malavasi, *Lignin in Woody Plants under Water Stress: A Review.* Floresta e Ambiente, 2016. **23**(4): p. 589-597.
103. Cuny, H.E., et al., *Kinetics of tracheid development explain conifer tree-ring structure.* New Phytol, 2014. **203**(4): p. 1231-1241.
104. Castagneri, D., G. Petit, and M. Carrer, *Divergent climate response on hydraulic-related xylem anatomical traits of Picea abies along a 900-m altitudinal gradient.* Tree Physiol, 2015. **35**(12): p. 1378-87.
105. Sperry, J.S., U.G. Hacke, and J. Pittermann, *Size and function in conifer tracheids and angiosperm vessels.* Am J Bot, 2006. **93**(10): p. 1490-500.
106. Sperry, J. and M. Tyree, *Water-stress-induced xylem embolism in three species of conifers.* Plant, Cell & Environment, 1990. **13**(5): p. 427-436.
107. Zahner, R., *Internal moisture stress and wood formation in conifers.* For. Prod. J, 1963. **13**(24): p. 247.
108. Huang, W., et al., *Annual Variations in Norway Spruce Xylem Studied Using Infrared Micro-spectroscopy.* Forests, 2019. **10**(2): p. 164.
109. Gindl, W., *Cell-Wall Lignin Content Related to Tracheid Dimensions in Drought-Sensitive Austrian Pine (Pinus Nigra).* IAWA Journal, 2001. **22**(2): p. 113-120.
110. Altangerel, N., et al., *In vivo diagnostics of early abiotic plant stress response via Raman spectroscopy.* Proc Natl Acad Sci U S A, 2017. **114**(13): p. 3393-3396.
111. Zhang, M., et al., *Tracheid cell-wall structures and locations of (1 --> 4)-beta-D-galactans and (1 --> 3)-beta-D-glucans in compression woods of radiata pine (Pinus radiata D. Don).* BMC Plant Biol, 2016. **16**(1): p. 194.
112. Wagner, A., L. Donaldson, and J. Ralph, *Lignification and Lignin Manipulations in Conifers*, in *Lignins - Biosynthesis, Biodegradation and Bioengineering*, L. Jouanin and C. Lapierre, Editors. 2012, Academic Press. p. 37-76.
113. Park, Y.-I. and H. Spiecker, *Variations in the tree-ring structure of Norway spruce (Picea abies) under contrasting climates.* Dendrochronologia, 2005. **23**(2): p. 93-104.
114. Gindl, W. and M. Grabner, *Characteristics of Spruce [Picea abies (L.) Karst] Latewood Formed under Abnormally Low Temperatures.* Holzforschung, 2000. **54**(1): p. 9-11.
115. Barros, J., et al., *The cell biology of lignification in higher plants.* Ann Bot, 2015. **115**(7): p. 1053-74.
116. Raven, J.A., *The Role of Vacuoles.* The New Phytologist, 1987. **106**(3): p. 357-422.

117. Cocozza, C., et al., *Do tree-ring traits reflect different water deficit responses in young poplar clones (Populus× canadensis Mönch 'I-214'and P. deltoides 'Dvina')?* Trees, 2011. **25**(6): p. 975-985.
118. Behmann, J., J. Steinrücken, and L. Plümer, *Detection of early plant stress responses in hyperspectral images.* ISPRS Journal of Photogrammetry and Remote Sensing, 2014. **93**: p. 98-111.
119. Farber, C. and D. Kurouski, *Detection and Identification of Plant Pathogens on Maize Kernels with a Hand-Held Raman Spectrometer.* Anal Chem, 2018. **90**(5): p. 3009-3012.
120. Martinelli, F., et al., *Advanced methods of plant disease detection. A review.* Agronomy for Sustainable Development, 2014. **35**(1): p. 1-25.
121. Bock, P., et al., *A Guide to Elucidate the Hidden Multicomponent Layered Structure of Plant Cuticles by Raman Imaging.* Front Plant Sci, 2021. **12**: p. 793330.
122. Leide, J., et al., *Leaf cuticle analyses: Implications for the existence of cutan/non-ester cutin and its biosynthetic origin.* Annals of botany, 2020.
123. Jeffree, C.E., E.A. Baker, and P.J. Holloway, *Ultrastructure and Recrystallization of Plant Epicuticular Waxes.* New Phytologist, 1975. **75**(3): p. 539-549.
124. Moreno, A., et al., *3D (x-y-t) Raman imaging of tomato fruit cuticle: microchemistry during development*. 2022.
125. Metsämuuronen, S. and H. Sirén, *Bioactive phenolic compounds, metabolism and properties: a review on valuable chemical compounds in Scots pine and Norway spruce.* Phytochemistry Reviews, 2019. **18**(3): p. 623-664.
126. Chong, J., A. Poutaraud, and P. Hugueney, *Metabolism and roles of stilbenes in plants.* Plant Science, 2009. **177**(3): p. 143-155.
127. Perez, M.R., et al., *Raman Spectroscopy an Option for the Early Detection of Citrus Huanglongbing.* Appl Spectrosc, 2016. **70**(5): p. 829-39.
128. Mandrile, L., et al., *Nondestructive Raman Spectroscopy as a Tool for Early Detection and Discrimination of the Infection of Tomato Plants by Two Economically Important Viruses.* Anal Chem, 2019. **91**(14): p. 9025-9031.
129. Lopez, M.M., et al., *Innovative tools for detection of plant pathogenic viruses and bacteria.* Int Microbiol, 2003. **6**(4): p. 233-43.
130. Weng, S., et al., *Advanced Application of Raman Spectroscopy and Surface-Enhanced Raman Spectroscopy in Plant Disease Diagnostics: A Review.* J Agric Food Chem, 2021. **69**(10): p. 2950-2964.
131. Sankaran, S., et al., *A review of advanced techniques for detecting plant diseases.* Computers and Electronics in Agriculture, 2010. **72**(1): p. 1-13.
132. Jones, R.R., et al., *Raman Techniques: Fundamentals and Frontiers.* Nanoscale Res Lett, 2019. **14**(1): p. 231.
133. Tahir, M.A., et al., *Surface-enhanced Raman spectroscopy for bioanalysis and diagnosis.* Nanoscale, 2021. **13**(27): p. 11593-11634.

Trees (2021) 35:1467–1484
https://doi.org/10.1007/s00468-021-02129-4

ORIGINAL ARTICLE

Physiological and anatomical responses to drought stress differ between two larch species and their hybrid

Nadia Sasani[1] · **Luc E. Pâques**[2] · **Guillaume Boulanger**[3] · **Adya P. Singh**[1] · **Notburga Gierlinger**[1] · **Sabine Rosner**[4] · **Oliver Brendel**[3]

Received: 3 September 2020 / Accepted: 7 April 2021 / Published online: 7 May 2021

Abstract

Key Message **Hybrid saplings were more reactive to soil water deficit than Japanese and European larch. European larch had hydraulically safer wood and anisohydric behavior, Japanese and hybrid larch showed isohydric strategy.**

Abstract Deciduous larch species could be an alternative to evergreen conifers in reforestation, but little is known about drought sensitivity of their saplings. The effect of an experimental drought on hydraulics and quantitative wood anatomy was tested on saplings of European larch (EL, *Larix decidua*), Japanese larch (JL, *Larix kaempferi*) and their hybrid (HL). Across species, biomass, transpiration rate and relative water content were higher in controls than in drought stressed trees, but transpiration efficiency was lower. JL had the highest transpiration efficiency under drought, and EL the lowest, coinciding with slower growth of EL. Wood of EL formed before drought was hydraulically safer as shown by higher wall/lumen ratio and lower pit cavity area. EL neither had a significant increase in transpiration efficiency nor a reduction in transpiration rate under drought, suggesting that the stomata remained open under soil water deficit. HL saplings were the most reactive to water shortage, indicated by intra-annual density fluctuations and a decrease in relative water content of the sapwood. Significant reduction in transpiration by HL suggested a higher stomatal sensitivity, while the same leaf surface area was maintained and radial growth was still similar to its best parent, the JL. The latter showed a significantly lower leaf surface area under drought than controls. EL, with its hydraulically safer wood, followed an anisohydric behavior, while JL and HL revealed an isohydric strategy. Altogether, our results suggest species dependent acclimations to drought stress, whereby HL followed the strategy of JL rather than that of EL.

Keywords Constitutive wood anatomy · Drought stress · Hybrid larch · *Larix decidua* · *Larix kaempferi* · Reaction to drought · Water use efficiency

Introduction

Climate change has drastic effects on the survival, reproduction, growth and productivity of trees. High temperatures together with water shortage are major stress factors, which cause physiological as well as structural changes (Breda et al. 2006; Allen et al. 2015; McDowell and Allen 2015; Mencuccini and Binks 2015; McDowell et al. 2016; Klein et al. 2019; Rozenberg et al. 2020). There is an expectation for forests to mitigate climate change through carbon storage and sequestration, protect against erosion, soil and snow slides; however, the demand for wood, particularly from conifers such as larch, has never been higher.

Species from the sub-family of the *Laricoideae*, European larch (*Larix decidua*) and Japanese larch (*Larix kaempferi*) are of high environmental and

---

Communicated by De Micco.

✉ Sabine Rosner
sabine.rosner@boku.ac.at

[1] Institute of Biophysics, University of Natural Resources and Life Sciences, Vienna, Austria

[2] INRAE, UMR BIOFORA, 45160 Ardon, France

[3] Université de Lorraine, AgroParisTech, INRAE, UMR Silva, 54000 Nancy, France

[4] Institute of Botany, University of Natural Resources and Life Sciences, Gregor Mendel Strasse 33, 1180 Vienna, Austria

socio-economical importance in several parts of the northern hemisphere (Geburek 2002; Pâques et al. 2013; Caudullo et al. 2018). The native range of both species is mostly mountainous, but some populations of European larch grow at elevations lower than 400 m. Their cultivation range has been successfully extended north- and westwards mostly in oceanic and continental climates, including lowland areas across Europe (Geburek 2002; Pâques et al. 2013). With less than 700,000 ha across its native range, European larch is considered as a minor species among conifers but it plays a major ecological (protection against snow and soil slides) and economical (timber production) role at regional levels particularly in the Alps (Geburek 2002; Pâques et al. 2013). Larch wood is much appreciated for its high density, mechanical properties, natural durability (outdoor use) and the aesthetics (indoor use) of its heartwood (Pâques et al. 2013). The use of alpine European larch provenances for plantation in lowland regions resulted in local maladaptation at the beginning of the twentieth century (Jansen and Geburek 2016). Japanese larch, which proved less susceptible to European larch canker (*Lachnellula willkommii* HARTIG), was thereafter used as an alternative but it failed in many locations due to its sensitivity to summer drought (Boudru 1986; Masson 2005). It is native to Japan and its natural distribution covers only about 390 km^2, where it grows in elevations from 500 up to 2900 m. Japanese larch prefers cold temperate to subarctic climates with high rainfall in summer and snowy winters (Caudullo et al. 2018). Foresters and breeders discovered in the first years of the twentieth century that the hybrid between European and Japanese larches (*Larix* x *eurolepis*) was much more vigorous than either of the parental species. From then on larch hybrids have been bred for improvement of growth, stem form, wood quality or disease resistance (Schneck et al. 2002; Pâques et al. 2013). Besides a greater vigour, hybrid larch successfully combines favourable traits from both its parental species; e.g., resistance to larch canker and *Meria laricis* VUILL as well as fast juvenile growth from Japanese larch and stem straightness as well as finer branching from European larch (Pâques et al. 2013; Caudullo et al. 2018). While European larch prefers a more continental climate, plantations of Japanese larch are restricted to oceanic conditions (e.g., Western France, UK, Ireland, Denmark, Belgium). In contrast, their inter-specific hybrid has proved suitable in a much wider spectrum of sites, ranging from maritime to continental and from sea level to low mountain ranges (Pâques et al. 2013; Greenwood et al. 2015). Hybrid larch can be thus successfully cultivated, wherever European or Japanese larches would have been cultivated. The use of larch or their hybrids outside their native ranges raises specific questions in terms of deployment and maladaptation. Facing the pressure of predicted climate change, an important goal to improve breeding of larch is to integrate drought responses from different species and their crosses.

The drought response of European larch has been extensively studied on mature trees (e.g., Anfodillo et al. 1998; Beikircher et al. 2010; Eilmann and Rigling 2012; Schuster and Oberhuber 2013; Swidrak et al. 2013; Dietrich et al. 2019), with the constraint that the level of drought stress can only be approximately determined. European larch has been considered as an anisohydric species (Swidrak et al. 2013), showing little stomatal response at the onset of drought and maintaining transpiration and carbon assimilation, while plant water potential is on the decrease (Streit et al. 2014). A high stomatal conductance during favourable conditions would optimise CO_2 fixation and, therefore, carbon accumulation and biomass growth, but might unduly increase water losses due to transpiration, thus resulting in low intrinsic water use efficiency (WUE, ratio between net CO_2 assimilation rate and stomatal conductance to water vapour). As a mature tree, European larch is known to have a lower WUE compared to other conifer species (Schuster and Oberhuber 2013). Similar observations were made by Anfodillo et al. (1998) on mature European larch trees in the Alps, where sap flow did not diminish despite an ongoing soil water deficit, by tolerating decreasing water potential. However, with increasing drought severity, sap flow strongly decreases and growth declines (Leo et al. 2014; Obojes et al. 2018). With a hydraulic safety margin lower than other native conifers, the decreasing plant water potential greatly increases the risk of xylem cavitation in European larch, as has been shown by Beikircher et al. (2010). Nevertheless, the study by Dietrich et al. (2019) on several tree species including European larch showed that after a severe drought period as in 2015, there was little indication of xylem embolism or carbohydrate depletion. Other studies indicated lower diameter growth of European larch during drought events than other native conifer species (Eilmann and Rigling 2012; Schuster and Oberhuber 2013; Lévesque et al. 2013, 2014a; Feichtinger et al. 2014; Streit et al. 2014).

Under the impact of drought, Japanese larch shows both isohydric and anisohydric strategies, with a stronger tendency towards isohydry (Bhusal et al. 2020). Japanese larch is rather drought sensitive (Boudru 1986; Masson 2005; Huang et al. 2017) and might be in danger when predicted climate change scenarios will take place; nevertheless, differences in growth response to drought do exist among provenances (Nagamitsu et al. 2018).

For hybrid larch, some reports exist, where the impact of drought on growth was investigated (Haasemann 1986; Cazaux et al. 1993; Marchal et al. 2019). Little information is, however, available on the strategy of hybrid larch to acclimate to drought. So far, we know that hybrid larch survival and growth are highly sensitive to soil water reserves

(Cazaux et al. 1993). In a nursery experiment combining the two parental larch species and their hybrid, three types of soil and three water regimes, Haasemann (1986) observed the overall superiority for height growth at age two of the hybrid even in the drier situation. However, its growth was optimal in the treatment with an average water supply, whereas optimal conditions for Japanese and European larches were, respectively, the moistest and the driest water regimes. More recently, Marchal et al. (2019) compared the radial growth of mature trees across sites and along gradients of soil water availability: not only did the hybrid have superior growth—except at the lowest levels of water availability—but it also showed a higher phenotypic plasticity and overall better site stability than both parental species. The success of the hybrid over European and Japanese larches clearly depends on water availability, where soil water reserves below 75 mm become critical with more severe mortality and reduced growth (Cazaux et al. 1993). However, a better understanding of the behaviour of European, Japanese larch and their hybrid under soil water deficit is critical for deployment recommendations and breeding strategies.

For effective breeding strategies for drought resistance, detailed knowledge about a species' ecological requirements during the whole rotation length will be necessary, especially as the hybrid might have inherited the drought sensitivity of Japanese larch (Boudru 1986; Masson 2005; Huang et al. 2017). The first years after plantation have been shown to be critical in tree development, in terms of resistance to drought in later stages and thus of the final plantation success (McDowell et al. 2008). Controlled greenhouse experiments on saplings allow simulation of drought stress and the direct comparison of the reaction of different species. As far as we know, drought stress experiments under controlled greenhouse conditions comparing different larch species or their crosses have not yet been performed.

The aim of our study was to characterise and to compare the drought response of saplings of two larch species, European larch and Japanese larch, and their hybrid under controlled drought conditions. The combination of these species was chosen, because European larch plays a major ecological role in, e.g., protection against snow and soil slides, and the hybrid of European and Japanese larch is of economical interest for timber production in plantations but we lack information on ecological requirements while in a juvenile state. Knowledge of their respective ecological requirements in the juvenile state would provide guidelines for their optimal deployment in forests. We address two main research questions: first, did the hybrid inherit drought sensitivity from the Japanese larch, and second, which anatomical traits are responsible for lower drought sensitivity? We hypothesise, that Japanese larch is more drought sensitive than European larch and that the hybrid shows higher drought plasticity during growth. Potential differences in drought sensitivity were examined with regard to whole plant transpiration response (plant water use, transpiration efficiency), biomass increase and wood formation. To infer hydraulic vulnerability, constitutive wood anatomy (anatomy before drought stress) including pit structural parameters was analysed. For the European larch, we hypothesise that its slower growth is associated with a hydraulically safer wood design, allowing a more anisohydric strategy, whereas a less safe design in the Japanese larch and the hybrid demands stronger stomatal control and thus a more isohydric strategy.

Materials and methods

Plant experimental setup

Three-year-old saplings of European larch (*Larix decidua* Mill., EL, seed source: Sudetan larch seed orchard Theil-FR), 4-year-old saplings of Japanese larch (*Larix kaempferi* (Lamb.) Carrière, JL, seed orchard Flensborg-DK) and 2-year-old saplings of hybrid larch (HL, *Larix* x *eurolepis*, parents of family REVE-VERT-FR) were used in our work. Due to different growth characteristics of the three species (especially the fast growth of the hybrid), saplings of similar age would have had very different sizes, whereas a selection purely on the size would have resulted in largely different ages. The tree height of European larch at the beginning of the experiment was 812.67 ± 101.67 mm, of hybrid larch 1236.50 ± 71.16 mm and of Japanese larch 1350.50 ± 88.77 mm. Prior to the experiment, plants were grown in two chambers of a glasshouse located at Champenoux, France (48°45′09.3″ N, 6°20′27.6″ E), under natural light conditions with daily maxima of irradiance ranging from 150 to 1000 µmol/m^2/s PAR. Environmental conditions in the greenhouse were affected by weather conditions, but the temperature was maintained between 15 and 26 °C. Three plants from each group were grown at similar soil water content conditions with two different water regimes, respectively. The field capacity (FC) at planting was estimated at 30% ± 1.7% soil volumetric humidity (SVH). The automatic watering was adjusted to that; the control plants (C-trees) remained at 80% of the field capacity of the soil. This corresponds to 24% relative extractable soil water content (REW = (SVH-WP)/(FC-WP), considering a wilting point (WP) at 2% SVH). Forest trees are considered to be under drought constraint at relative water content below 40% relative extractable soil water content; therefore, a final target SVH for drought-stressed plants (S-trees) was below this value at 30% of the field capacity of the soil, corresponding to 10% SVH (Granier et al. 1999). The potted plants were put on a robotic weighing and watering system (Bogeat-Triboulot et al. 2019) after all trees had flushed on March 22, 2015 (day 80). The soil surface of each pot was covered with white marble gravel (diameter about 1 cm) to reduce soil water evaporation and four pots without plants, each for control and drought conditions, were used to estimate residual soil evaporation with the same frequency as the transpiration estimates for the plants. Cumulative transpiration over the whole experimental period (TRcum) was calculated by summing the water losses between two weighings of each plant. Plant transpiration rate (Trp, Online Resource 1) was calculated by dividing the water loss by the time between two weighings. The target drought level of 10% SVH was approached in a controlled stepwise way by not watering the pots until the target was reached. Bigger plants with a larger leaf surface use the available water reserve in the pots more rapidly, allowing more rapid approach of the final SVH target level. Thus, four levels of SVH (25%, 20%, 15%, 10%) were used and the advancement from one level to the next was constrained until all plants had reached this drought level; 25% SVH was reached on day 100, 20% on day 107, 15% on day 110 and 10% on day 160. The trees were under moderate drought conditions from day 107 to day 176, thus for 70 days. The number of irrigations per day was adjusted to the transpiration of the plants, so that overall each watering level was less than 100 ml water, starting with two irrigations per day at the beginning of the experiment, and five irrigations per day at the end. Plants were harvested on June 26, 2015 (day 176). For the determination of the relative water content (see below), a 5 cm long stem segment was cut just above the root collar. Stem samples with a length of 5 cm were collected adjacent to these segments and stored frozen at − 20 °C until the anatomical investigation. The sample set comprised three trees per treatment and species ($n = 18$, Online Resource 2).

Biomass determination

To estimate initial biomass, allometric relationships were estimated from three individuals, representative of the size range, from each species. Stems and branches were measured for basal and apical diameters and length (overall $n = 520$). Roots were separated and washed. All parts were dried at 65 °C to constant mass and weighed. Dry mass (DM) was determined for each tree for each compartment (stem or branch) and volumes were summed up. Density was estimated as mass/volume, and an ANOVA analysis (separately for stem and branches) showed that there was no significant species effect for density and only a slight increment effect for the stem. It was, therefore, decided to estimate one allometry for stems, using a power equation ($\mathrm{DM} = 0.95145 \times V^{0.92404}$, $R^2 = 0.94$, $n = 26$) and one for branches ($\mathrm{DM} = 0.6569 \times V^{1.0008}$, $R^2 = 0.92$, $n = 16$). These allometries were applied to all measured stems and branches at the beginning of the experiment ($n = 1105$). Initial root biomass was estimated using the estimated stem mass ($\mathrm{DM} = 86.80 \times \mathrm{stem} - \mathrm{DM}^{0.642}$; $R^2 = 0.66$, $n = 26$). Stem, branch and root DM were used to calculate the initial dry mass of each tree.

During the final harvest, stems, branches and roots were separated. The roots were washed and all plant organs were dried as described above. For the harvested plants, the main stem, last year's branches, new branches, needles from last year's branches, needles from new branches and roots (washed) were separated and dried as indicated above. Final biomass was calculated as the sum of the dry masses of the different plant organs.

The biomass increment (BMinc) was calculated as the difference between the final biomass and the initial biomass (BMini). The relative biomass increment was calculated as BMinc/BMini and is given as a percentage.

Needle surface area and plant transpiration per leaf surface area

To estimate final needle surface area (NSF), needles were harvested to establish an allometric relationship between needle dry mass (DM) and needle surface. The surface of all needles from three current year (2015) and three 1-year-old (2014) branches from each tree were measured using a flatbed scanner. ANOVA showed that there was neither a significant species effect nor a significant treatment effect on leaf mass per area. However, a significant needle age effect was detected. Therefore, we used two different allometric equations to convert needle dry mass into needle surface. Thus, power equations were established between needle mass and needle surface (for 1-year-old needles, $\mathrm{NSF} = 0.2358 \times \mathrm{DM}^{0.8585}$; for current year needles: $\mathrm{NSF} = 0.0145 \times \mathrm{DM}^{1.0534}$ with DM = needle dry mass). Total needle surface was estimated as the sum of the two needle generations (2014 and 2015).

Transpiration traits

The assessment of the cumulative transpiration over the whole experimental period (TRcum) and the plant transpiration rate (Trp) is described in the section "Plant experimental setup". The transpiration efficiency (TE) was calculated as the total biomass increase (BMinc) divided by the cumulative transpiration (TE = BMinc/TRcum).

Plant transpiration per hour and per leaf surface (TR) was calculated as the plant transpiration rate (Trp) divided by the total final needle surface (TR = Trp/NSF).

Relative water content

The relative water content (RWC) of the trunk was estimated from a 5 cm section of the main stem just above the root collar. At the harvest, the bark was taken off and the fresh mass determined (FM), then the stem parts were infiltrated by keeping them under water in a closed glass container under vacuum, until air bubbles from stem parts had completely subsided. Then surface water was dried off and the water-saturated mass determined (SM). Subsequently, the samples were dried at 65 °C until constant weight to measure the dry mass (DM). RWC was calculated as RWC (%) = 100 × (FM-DM)/(SM-DM).

Carbon isotope composition (δ^{13}C)

At the final harvest, several needles from apical shoots were sampled, dried for 48 h at 70 °C and ground into a fine powder using a ball mill (Retsch GmbH, Haan, Germany). Subsamples of 1 mg ± 0.1 mg were weighed into tin capsules and the carbon isotopic composition was measured with an isotope ratio mass spectrometer (Thermo-Finnigan, Delta S, Bremen, Germany). The carbon isotope composition (δ^{13}C) was calculated according to the international standard (Vienna Pee Dee Belemnite, VPDB) using the following equation: $\delta^{13}\mathrm{C} = (R_s - R_{std})/R_{std} \times 1000$, where R_s and R_{std} are the isotopic ratios ^{13}C/^{12}C of the sample and the standard, respectively. The precision of spectrometric analysis (standard deviation of δ^{13}C) was assessed with a calibrated, internal laboratory reference material with a matrix close to the measured samples ($n = 16$, SD = 0.05‰).

Wood formation of control and drought stressed trees (tracheidograms)

To evaluate the impact of drought on anatomical traits, radial lumen diameters and the tangential double cell wall thickness were measured in one complete radial cell row of the latest wood increment, for each tree. Dissected pieces of normal wood (avoiding compression wood) harvested at 5 cm from the ground were mounted in the sample holder of a cryo-microtome (CM 3050 S, Leica Biosystems Nussloch GmbH, Germany) keeping the orientation perpendicular to the main fiber axis. Disposable microtome blades (N35HR Blade 35, Feather, Japan) were used to cut 10–20-µm-thick transverse sections. Sections were stained with safranine/astra-blue. Lignified cell walls appear red after safranine staining, and non-lignified cell walls acquire blue colour after astra-blue staining. For anatomical analysis, sections were dehydrated in ethanol and mounted on slides in Canada balsam. Images were acquired with a Leica DM4000 M microscope equipped with a Leica DFC 320 R2 digital camera. Leica IM 500 image manager analyzing software was used for digital stitching (Leica, Weltzlar, Germany) and Image J software (https://imagej.nih.gov) for quantitative anatomical measurements. Mean values of radial lumen diameters and the tangential double cell wall thickness were thereafter calculated for 5% radial distance steps, with the whole wood increment as 100% reference. Means of anatomical traits measured in the region of 90–95% of the increment (radial lumen diameter, b_r 90–95% and tangential cell wall thickness, t_t 90–95%) were used for comparisons within and among species. The cell walls were still thickening in the region between 95 and 100% of the increment; we thus avoided analysing this part statistically.

Constitutive wood anatomy: tracheid dimensions and quantitative pit anatomy

We refer "constitutive wood anatomy" to quantitative anatomical traits before plants were impacted by drought. This approach is based on Rosner et al. (2016) who found that the wood formed before drought stress impacts the sensitivity to drought in conifers. To elucidate whether the variation in anatomical functional traits, such as tracheid and pit dimensions, affected species' performance of the trees under drought stress, we assessed such traits in the first formed early wood tracheids of the latest annual ring. ANOVA indicated no influence of initial biomass and treatment (drought stress) on the traits investigated, indicating that before stress started, no anatomical differences were present which were related to the size of the saplings or treatment. Therefore, statistical analysis on species differences of tracheid dimensions, conduit wall reinforcement and pit traits were done by pooling all trees from a given species.

Tracheid dimensions and conduit wall reinforcement were assessed on wood sections stained with safranine/astrablue (details in an earlier section). Double cell wall thickness (t) and lumen diameter (b) of early wood cells were measured in radial (t_r, b_r) and tangential (t_t, b_t) directions in the first 10 cell rows of the 2015 growth ring using Image J software. For each of the four traits, a tree mean value was calculated from 20 single measurements that were performed on four different positions around the whole circumference. Conduit wall reinforcement was calculated in the radial ($(t_r/b_r)^2$) and tangential ($(t_t/b_t)^2$) direction (Rosner et al. 2018).

Light microscopy images were used for the determination of the pit cavity area (Fig. 1a, right). SEM images (Fig. 1a, left; Fig. 1b) were used for all other measurements, such as the pit membrane diameter (PMD) torus diameter (TD) and the pit aperture diameter (AD).

For light microscopy, sections (5–10 µm thick) were cut from frozen samples using a cryo-microtome. Preliminary work undertaken to select the most effective stain indicated that toluidine blue, which stains wood cell wall, including the pit border, greenish blue and the pit torus pink–magenta, to be the most suitable stain. The sections were stained for 2 min, then washed with water and mounted on glass slides in a drop of water. Nail polish was used to seal the cover glass. The sections were

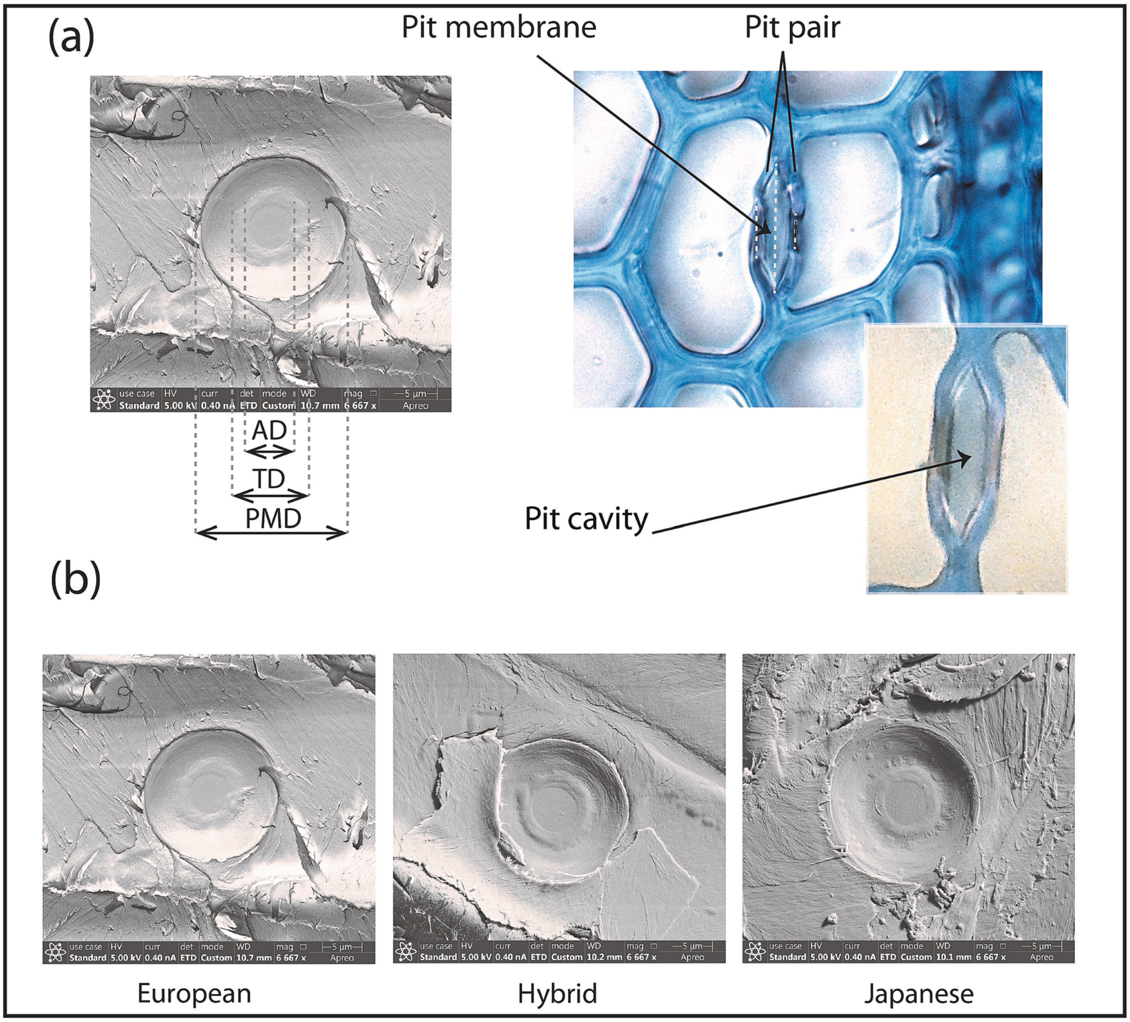

Fig. 1 Documentation of measurements on bordered pits. **a** left side, SEM image of a radial wood section showing a bordered pit with pit aperture diameter (AD), torus diameter (TD) and pit membrane diameter (PMD). **a** right side, light microscopy photo of a transverse wood section stained with toluidine blue; the insert shows the pit cavity at higher magnification. **b** SEM images of bordered pits of European, hybrid and Japanese larch

examined with a light microscope (Nikon, Japan) and the images were captured with a digital camera. For each sample, 20 intact pits were selected in early wood of the 2015 wood increment. Pit cavity was defined and measured using image J (Fig. 1a, right).

For SEM, air-dried wood blocks were split longitudinally, exposing the radial face. The samples were mounted on stubs and coated with gold particles in a sputter coater (LEICA EM SCD005). Images were acquired using the Apreo SEM (ThermoFisher Scientific, Massachusetts, USA) at 5 kV. Measurements of membrane diameter (PMD), torus diameter (TD) and pit aperture diameter (AD) were done using the ImageJ software. Twenty pits were used for each tree sample. Torus overlap (TO, torus–aperture overlap, torus to aperture ratio) was determined as (TD-AD)/TD (Fig. 1a, left).

Statistical analyses and sample numbers

Traits investigated and analysed as well as their abbreviations are listed in Table 1. Differences between species and the drought treatment effects of biomass- and transpiration-related traits were analysed using an ANCOVA model (R Core Team 2020) in particular for taking into account the different sizes of trees at the beginning of the experiment:

$$Y = \text{BMini} + \text{species} + \text{treatment} + \text{species} \times \text{treatment},$$

BMini is the covariate for initial biomass differences among plants, species is the effect for European, hybrid or Japanese larch, treatment is the control vs. drought effect and species × treatment is their interaction (only included in the model when significant). BMini was only significant

Table 1 List of investigated growth parameters, physiological- and anatomical traits and their abbreviations

Abbreviation	Trait	Unit
AD	Aperture diameter of bordered pits	µm
BMinc	Biomass increase	g
BMinc%	Relative biomass increase	%
BMini	Initial biomass	g
b_r	Radial lumen diameter of tracheids	µm
b_r 90–95%	b_r in 90–95% of the radial increment 2015	µm
b_t	Tangential lumen diameter of tracheids	µm
DS	Diameter of the stem	mm
PC	Pit cavity	μm^2
PMD	Pit membrane diameter	µm
RWC	Relative water content	%
NSF	Needle surface area	cm^2
TD	Torus diameter	µm
TE	Transpiration efficiency	g/kg
TO	Torus overlap	%
t_r	Radial double cell wall thickness	µm
$(t_r/b_r)^2$	Conduit wall reinforcement radial direction	
TR	Transpiration rate per needle surface	$g/h/m^2$
t_t	Tangential double cell wall thickness	µm
t_t 90–95%	t_t in 90–95% of the radial increment 2015	µm
$(t_t/b_t)^2$	Conduit wall reinforcement tangential direction	
$\delta^{13}C$	Carbon isotope composition current year shoots	‰

($P < 0.05$) for few traits (TR, TRcum, TE, NSF, BMinc%). The normality of the residuals of the ANCOVA analyses was tested using the Shapiro–Wilks test. We detected a significant deviation from normality for TR and Trcum. A Box–Cox transformation was applied. As the ANOVA on the transformed variables resulted in similar significance levels for the different factors, it was decided to only present the untransformed results. Means and group differences for species, treatment and species × treatment were estimated using the HSD test function (Tables 2, 3 and 4, HSD.test, agricolae package, R Core Team 2020) to reflect the measured data. However, when an influence of the initial biomass was observed, within factor significant pairwise differences were estimated using also marginal means (emmeans, emmeans package, R Core Team 2020).

We investigated three trees per species and treatment, respectively. In total, 18 trees were investigated (Online Resource 2). For analyses of constitutive wood- and pit anatomy, six trees per species were pooled. Tree mean values for constitutive wood- and pit anatomy were calculated from 20 single measurements per tree, respectively. Final statistical analyses were then performed with tree mean values.

Results

Effects of initial biomass, species and drought and their interaction on growth and physiology

Significant species effects were found for biomass at the beginning of the experiment (Fig. 2f). Therefore, to take this into account in the following analyses, initial biomass was tested as a covariate. Transpiration rate, needle surface area and relative biomass increase showed a significant effect of the initial biomass (Table 2).

Significant species effects were found for absolute- and relative biomass increase, transpiration efficiency and $\delta^{13}C$, with JL having the highest values, followed by HL and EL. No significant overall species effect was found for transpiration rate, RWC, needle surface area and stem diameter (Table 2).

A significant drought effect was found for all traits except for initial biomass, indicating an even distribution of plants across treatments before the stress was applied (Table 2).

Species*treatment interaction effects were significant for all transpiration traits and the absolute biomass increase (Table 2).

Information on the impact of drought within and among species on physiological and growth traits can be found in Table 3. Transpiration rate (Fig. 2a) and transpiration efficiency (Fig. 2b) had a significant drought effect in HL and JL (marginal means, Table 3). Drought stressed HL had a similar transpiration rate as JL, but it showed a much stronger decline in transpiration rate than JL (Table 3, Fig. 2a) and a lower increase of transpiration efficiency (Table 3, Fig. 2b). Within species, $\delta^{13}C$ was significantly higher (less negative) in drought stressed than in control trees (Table 3). RWC was also lower in stressed trees than in control trees (Fig. 2c), but a significant decrease was solely found for HL (Table 3). Needle surface area (Fig. 2d) was significantly lower in stressed JL; EL showed a similar trend, whereas HL had similar measured values in both groups (Table 3). Absolute biomass increase (Fig. 2g) was significantly lower in HL and JL. Even though relative biomass increase (Fig. 2h) was affected by the initial biomass (Table 2), we found a significant decrease for the marginal means of drought stressed HL and JL (Table 3). Stem diameter was significantly affected by drought in all three species (Fig. 2e, Table 3).

Characteristics of wood produced under the impact of drought

Differences in wood anatomy were analysed in 5% steps along the latest radial increment. Stressed trees showed a decrease in radial lumen starting at about 50% of the

Table 2 Means and standard errors of physiological traits and biomass parameters for the three species, as well as for control vs. drought plants; letters are representing significant differences in the measured means and marginal means

Trait	Unit	BMini	Species	European larch	Hybrid larch	Japanese larch	Treatment			Int
		P	*P*				*P*	Control	Drought stressed	*P*
TR	g/h/m^2	*	–	0.0116 ± 0.0008a	0.0107 ± 0.0024a	0.0076 ± 0.0009b	***	0.0128 ± 0.0010a	0.0071 ± 0.0009b	**
				0.0086 ± 0.0011A	0.0105 ± 0.0005A	0.0107 ± 0.0012A		0.0130 ± 0.0004A	0.0068 ± 0.0004B	
TE	g/kg	–	**	4.01 ± 0.33c	4.90 ± 0.46b	6.15 ± 0.81a	***	3.92 ± 0.21b	6.13 ± 0.50a	*
δ^{13}C	‰	–	**	– 27.89 ± 0.40b	– 27.45 ± 0.44ab	– 27.05 ± 0.44a	***	– 28.37 ± 0.18b	– 26.55 ± 0.15a	–
RWC	%	–	–	95.9 ± 1.7a	90.8 ± 3.1a	91.0 ± 1.3a	**	96.0 ± 1.0a	89.1 ± 1.9b	–
NSF	cm^2	***	–	1594 ± 295c	2605 ± 311b	4617 ± 544a	**	3536 ± 601a	2342 ± 380b	–
				3312 ± 396A	2692 ± 189A	2813 ± 411A		3370 ± 158A	2508 ± 158B	
BMini	g	–	***	61.2 ± 4.1c	108.5 ± 8.4b	163.3 ± 8.5a	–	115.9 ± 17.4a	106.2 ± 13.8a	–
BMinc	g	–	***	106.9 ± 14.5c	190.0 ± 28.8b	309.5 ± 34.0a	***	255.4 ± 37.2a	148.8 ± 23.5b	*
BMinc%	%	***	**	172.4 ± 15.8a	186.0 ± 40.0a	187.7 ± 13.8a	***	225.4 ± 18.3a	138.7 ± 7.6b	–
				76.8 ± 25.3C	181.2 ± 12.1B	288.0 ± 26.3A		234.6 ± 10.1A	129.5 ± 10.1B	
DS	mm	–	–	17.7 ± 1.1c	21.7 ± 1.2b	24.8 ± 1.7a	***	24.1 ± 1.3a	18.7 ± 1.0b	–
b_r 90–95%	µm	–	***	22.17 ± 2.34a	12.59 ± 2.24b	13.72 ± 2.06b	***	20.59 ± 1.85a	11.73 ± 1.56b	–
t_t 90–95%	µm	–	*	4.03 ± 0.43b	6.33 ± 0.68a	6.09 ± 0.76ab		4.85 ± 0.52a	6.12 ± 0.64a	–

Marginal means can be found below the measured means in case there was a significant effect of initial biomass. Significant differences in the mean values at the $P < 0.05$ level for either species or treatment are indicated by different letters, for marginal means by capital letters. Abbreviations are explained in Table 1

Results of ANCOVA analysis including effects of initial biomass (BMini), treatment and interaction (Int) factors are indicated with “-” for $P \geq 0.5$, “*” for $P < 0.05$, ** for $P \leq 0.01$ and “***” for $P \leq 0.001$, n = 6 trees/species and 9 trees/treatment

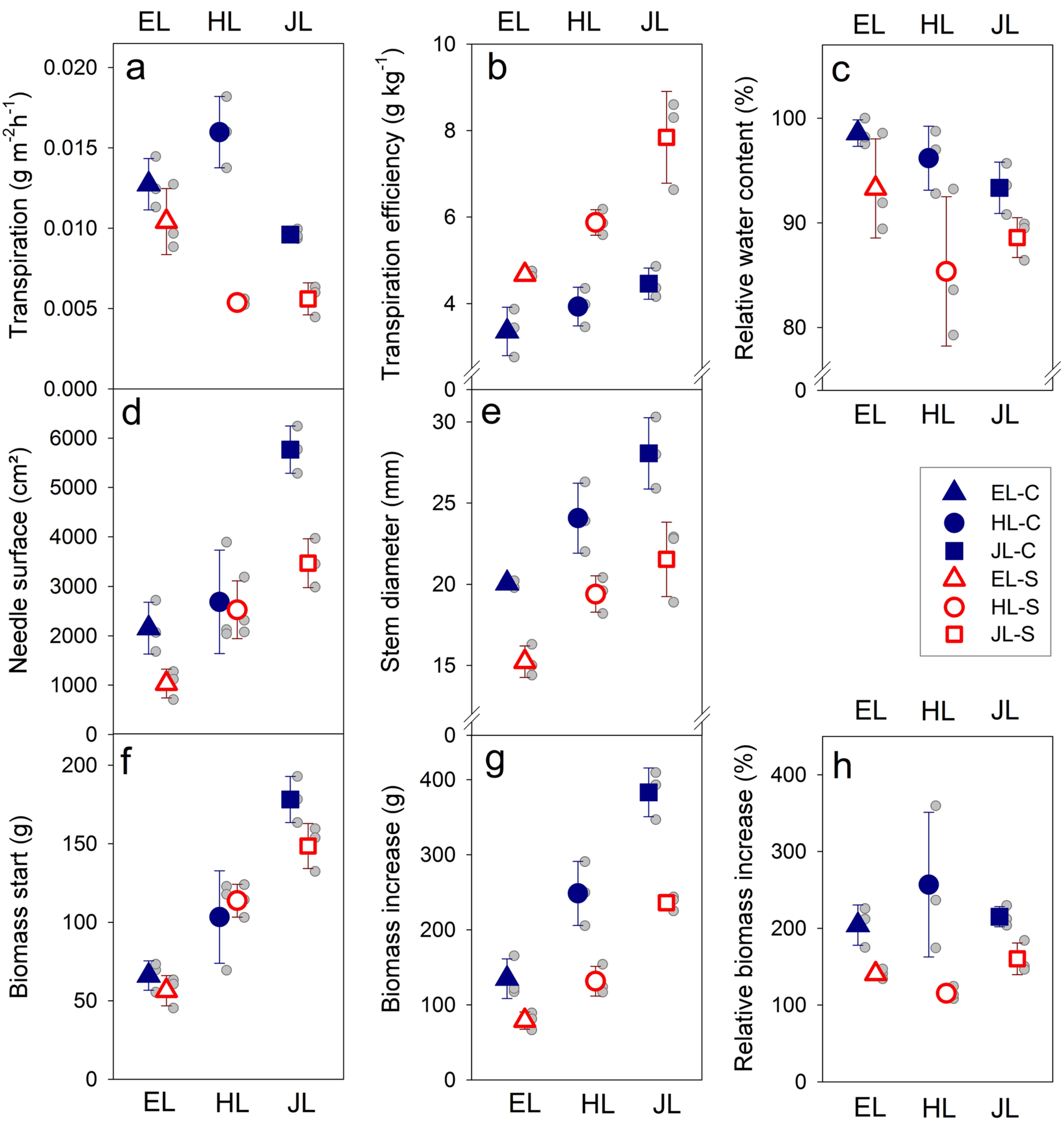

Fig. 2 Transpiration rate per needle surface (**a**), transpiration efficiency (**b**), relative water content (**c**), needle surface area (**d**), stem diameter at the beginning of the experiment (**e**), biomass at the beginning of the experiment (**f**), biomass increase (**g**) and relative biomass increase (**h**) of three different larch species. Whiskers indicate the standard deviation and grey dots data for each single tree. Closed symbols indicate "control" trees, open symbols indicate drought stressed trees. *EL* European larch; *HL* hybrid larch, *JL* Japanese larch

increment for all species (Fig. 3). When lumen diameters were plotted against the absolute distance from pith to bark (tracheidograms), the extreme reaction of HL to drought stress became obvious (Online Resource 3): in addition to a decrease in radial increment, lumen diameters decreased (see also examples in Fig. 4). In the region of the last 90–95% of the increment, radial lumen diameters significantly decreased due to drought in all species, but drought stressed EL had significantly larger lumens than stressed HL and JL (Table 3). Cell

Table 3 Mean values and standard errors of physiological traits and biomass parameters for interaction of species and treatment (C Control, S Drought stress)

Trait	Units	BMini P	European C	European S	Hybrid C	Hybrid S	Japanese C	Japanese S
TR	$g/h/m^2$	*	0.0127 ± 0.0009b	0.0104 ± 0.0012b	0.0160 ± 0.0013a	0.0054 ± 0.0001c	0.0096 ± 0.0002b	0.0056 ± 0.0006c
			0.0101 ± 0.0011BC	0.0072 ± 0.0013BC	0.0155 ± 0.0007A	0.0055 ± 0.0007B	0.0136 ± 0.0015AC	0.0078 ± 0.0010B
TE	g/kg	–	3.36 ± 0.32c	4.67 ± 0.04bc	3.93 ± 0.26c	5.88 ± 0.17b	4.46 ± 0.21bc	7.84 ± 0.61a
$\delta^{13}C$	‰	–	– 28.74 ± 0.24c	– 27.03 ± 0.17ab	– 28.44 ± 0.14c	– 26.47 ± 0.06a	– 27.94 ± 0.39bc	– 26.16 ± 0.18a
RWC	%	–	98.6 ± 0.7a	93.3 ± 2.7ab	96.2 ± 1.8a	85.4 ± 4.1b	93.3 ± 1.4ab	88.6 ± 1.1ab
NSF	cm^2	***	2156 ± 303 cd	1032 ± 169d	2686 ± 603bc	2525 ± 337bc	5767 ± 276a	3468 ± 284b
			3383 ± 438AB	2525 ± 502AB	2897 ± 263AB	2451 ± 257AB	3934 ± 589A	2444 ± 392B
BMini	g	–	66.1 ± 5.4c	56.4 ± 5.6c	103.3 ± 17.0bc	113.8 ± 6.0b	178.2 ± 8.5a	148.6 ± 8.3ab
BMinc	g	–	134.8 ± 1.5c	78.9 ± 6.6c	248.5 ± 24.6b	131.5 ± 11.4c	382.9 ± 18.8a	236.1 ± 5.7b
BMinc%	%	***	204.2 ± 15.1ab	140.6 ± 3.7bc	256.8 ± 54.4a	115.3 ± 4.7c	215.1 ± 7.6ab	160.2 ± 12.0bc
			122.2 ± 29.8ABC	40.9 ± 34.1BC	242.7 ± 17.9DE	120.2 ± 17.5B	337.5 ± 40.0AD	228.6 ± 26.6CE
DS	mm	–	20.1 ± 0.1bc	15.2 ± 0.6d	24.1 ± 1.2ab	19.4 ± 0.6 cd	28.1 ± 1.3a	21.5 ± 1.3bc
b_r 90–95%	µm	–	27.1 ± 0.4a	17.2 ± 1.6b	17.5 ± 0.4b	7.7 ± 1.1c	17.1 ± 2.9b	10.3 ± 1.1c
t_t 90–95%	µm	–	3.8 ± 0.7a	4.3 ± 0.5a	5.2 ± 0.1a	7.4 ± 1.0a	5.6 ± 1.3a	6.6 ± 0.9a

Marginal means are provided below the measured means when there was a significant effect of initial biomass. Significant differences in the mean values at the $P < 0.05$ level for either species or treatment are indicated by different letters, for marginal means by capital letters

Abbreviations are explained in Table 1

For comparison, significant biomass effects from the ANCOVA (BMini P), shown already in Table 2, are indicated with "-" for $P \geq 0.5$, "*" for $P < 0.05$, ** for $P \leq 0.01$ and "***" for $P \leq 0.001$, $n = 3$ trees/species/treatment

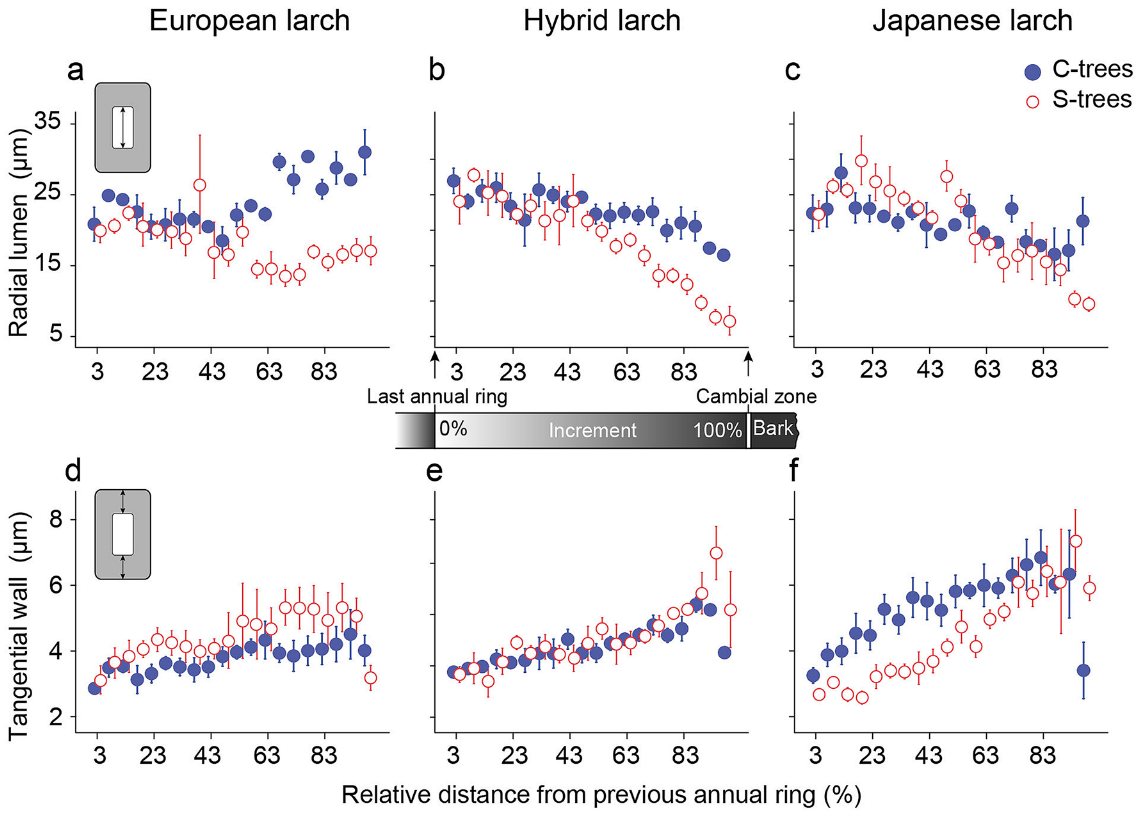

Fig. 3 Tangential wall thickness and radial lumen diameter in 5% steps of the 2015 increment of European, hybrid and Japanese larch trees with two treatments (control and drought stress). Each stepwise mean value of radial lumen diameter of European larch (**a**), hybrid larch (**b**), and Japanese larch (**c**), and tangential wall thickness of European larch (**d**), hybrid larch (**e**), and Japanese larch (**f**) is shown with standard deviation for the two treatments "control" (C-trees, closed symbols) and drought stressed trees (S-trees, open symbols). Whiskers indicate the standard deviation

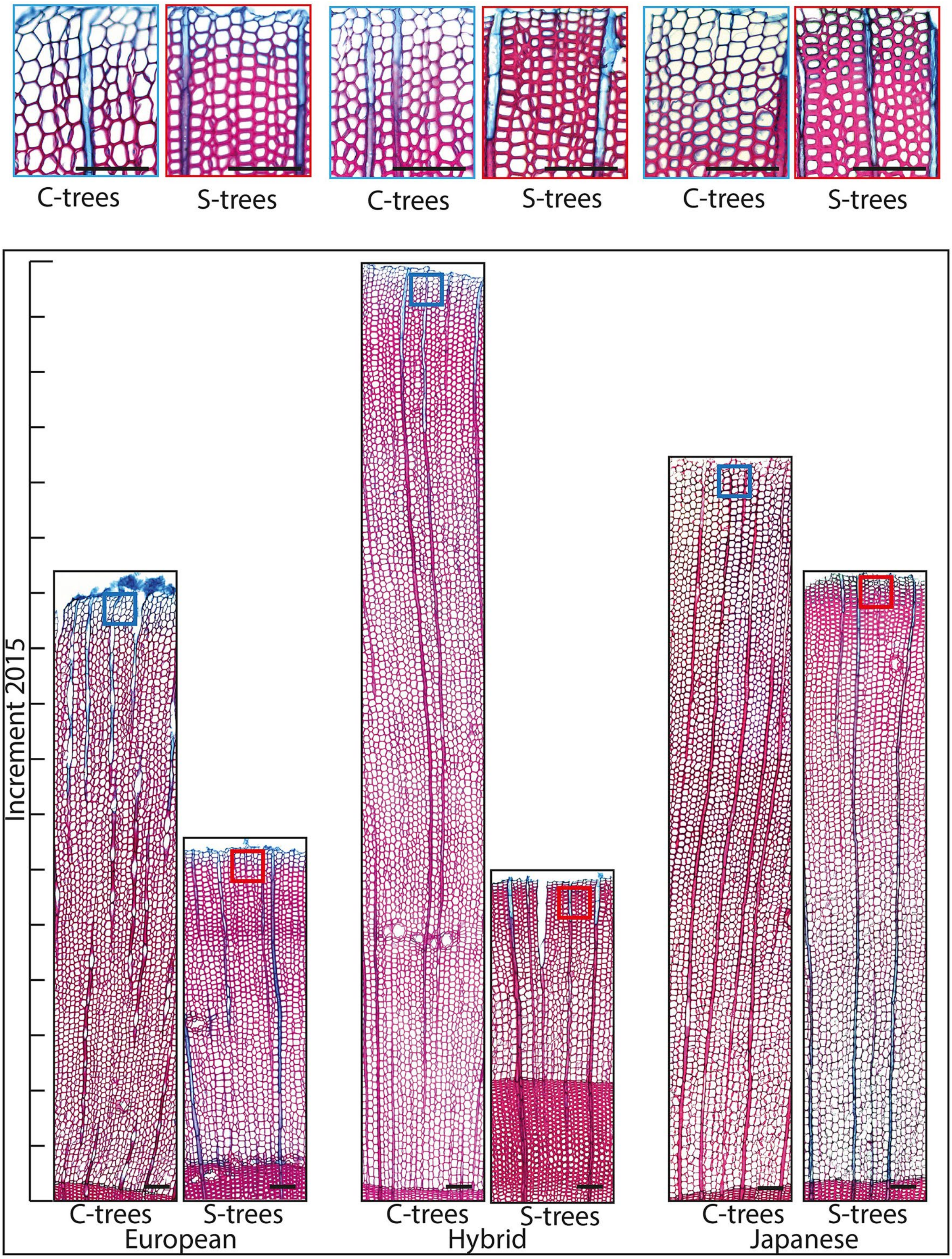

Fig. 4 Selected transverse sections of the wood increment 2015 of control trees (C-trees) and drought stressed trees (S-trees) of European larch (EL), hybrid larch (HL) and Japanese larch (JL). Boxed regions show the rear part of the increment in higher magnification. Sections were stained with safranin and astrablue. The scale bar is 100 µm

wall thickness in 90–95% of the increment also showed a tendency (treatment factor in ANOVA $P = 0.08$, Table 2) for higher values under drought, especially in HL (Table 3, Fig. 3). Smaller lumen diameters together with an increase in cell wall thickness in stressed trees resulted in a denser wood produced towards the end of the experiment (Fig. 3). We found negative correlations between radial lumen diameters in 90–95% of the increment and transpiration efficiency (Fig. 5a) as well as with carbon isotope compositions of the current year shoot (δ^{13}C) (Fig. 5b).

Constitutive wood anatomy

In the wood formed before the start of the experimentation, we found no significant differences between Japanese larch (JL) and hybrid larch (HL) in lumen diameter or cell wall thickness traits (Table 4). However, European larch (EL) had significantly smaller tangential lumen diameters, which implied higher theoretical hydraulic safety against implosion of the tangential cell walls ($(t_t/b_t)^2$) compared to the other two species (Fig. 6a, Table 4). The conduit wall reinforcement of the radial cell walls ($(t_r/b_r)^2$) (Fig. 6b) showed no significant differences between species. The mean tangential lumen diameter was positively related to the initial

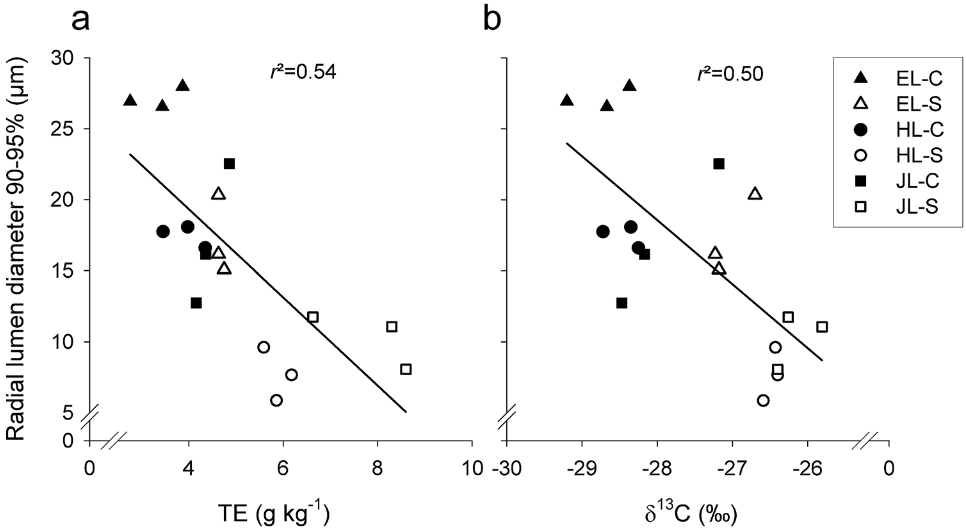

Fig. 5 Relationships between radial lumen diameters in 90–95% of the latest formed annual ring and physiological traits such as transpiration efficiency (**a**) and δ^{13}C (**b**). Triangles indicate European larch (EL-C, EL-S), circles hybrid larch (HL-C, HL-S) and squares Japanese larch (JL-C, JL-S) of control (closed symbols, EL-C, HL-C, JL-C) and drought stressed (open symbols, EL-S, HL-S, JL-S) trees, respectively

Table 4 Means and standard errors of anatomical traits for three larch species; letters represent significant differences in the mean values at the $p < 0.05$ level for either species (n = 6 trees/species) or treatment (n = 9 trees/treatment)

Trait	Unit	Species *P*	European larch	Hybrid larch	Japanese larch	Control	Drought stressed	Int *P*
b_r	µm	*	25.37 ± 0.92b	29.41 ± 0.57a	26.52 ± 1.02ab	26.50 ± 0.63a	27.70 ± 1.08a	–
b_t	µm	***	19.18 ± 0.77b	22.06 ± 0.31a	23.81 ± 0.42a	21.68 ± 0.78a	21.69 ± 0.81a	–
t_r	µm	–	2.30 ± 0.13a	2.28 ± 0.11a	2.19 ± 0.17a	2.31 ± 0.10a	2.21 ± 0.12a	–
t_t	µm	–	2.39 ± 0.12a	2.03 ± 0.15a	1.93 ± 0.22a	2.21 ± 0.14a	2.02 ± 0.16a	–
$(t_r/b_r)^2$			0.0094 ± 0.0012a	0.0066 ± 0.0007a	0.0086 ± 0.0019a	0.0088 ± 0.0011a	0.0076 ± 0.0011a	*
$(t_t/b_t)^2$		**	0.0174 ± 0.0010a	0.0096 ± 0.0016b	0.0080 ± 0.0021b	0.0125 ± 0.0019a	0.0108 ± 0.0019a	–
PMD	µm	–	14.71 ± 0.71a	15.27 ± 0.33a	15.80 ± 0.30a	15.28 ± 0.48a	15.24 ± 0.33a	–
TD	µm	–	7.94 ± 0.46a	8.31 ± 0.12a	8.71 ± 0.19a	8.27 ± 0.31a	8.37 ± 0.21a	–
AD	µm	–	4.53 ± 0.18a	4.85 ± 0.17a	4.57 ± 0.21a	4.78 ± 0.16a	4.53 ± 0.14a	–
TO		–	0.420 ± 0.036a	0.416 ± 0.022a	0.475 ± 0.021a	0.417 ± 0.026a	0.457 ± 0.019a	–
PC	µm^2	**	43.50 ± 1.30b	48.24 ± 0.69a	47.59 ± 0.91a	46.08 ± 1.06a	46.81 ± 1.09a	–

Significant differences in the mean values at the $P < 0.05$ level for either species or treatment are indicated by different letters

Abbreviations are explained in Table 1

Species and species x treatment effects (Int) are indicated with “-” for $P \geq 0.5$, “*” for $P < 0.05$, ** for $P \leq 0.01$ and “***” for $P \leq 0.001$. We found neither an effect of initial biomass nor of the treatment on the constitutive anatomical traits

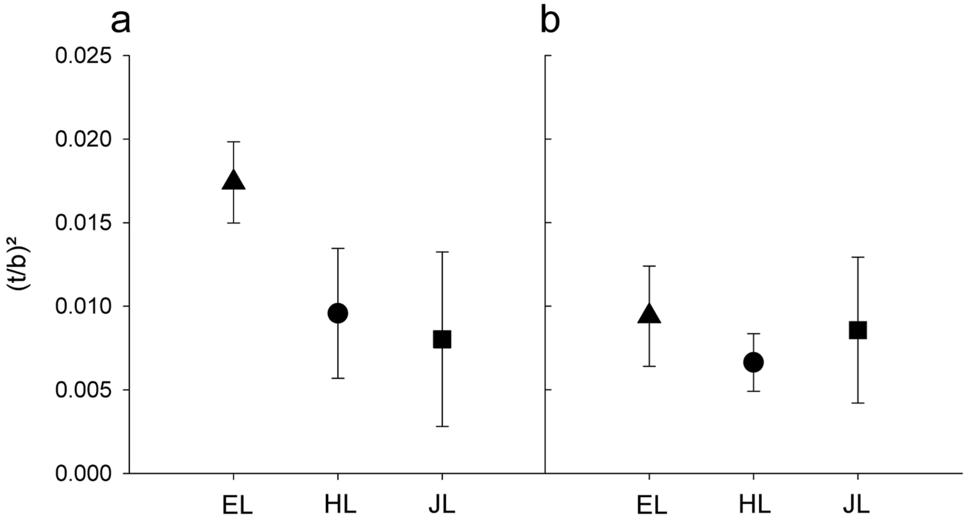

Fig. 6 Conduit wall reinforcement in the tangential direction (**a**) and in the radial direction (**b**) in the first formed earlywood tracheids of European larch (EL), hybrid larch (HL) and Japanese larch (JL). Whiskers indicate the standard deviation ($n = 6$ trees/species)

biomass ($r = 0.80$, $P < 0.0001$, $n = 18$) across species (Online Resource 4a). Accordingly, $(t_t/b_t)^2$ was negatively related to the initial biomass ($r = 0.60$, $P < 0.01$, $n = 18$) (Online Resource 4b).

There were no significant differences in pit membrane-, aperture-, and torus diameters as well as in the torus overlap between the species. Pit cavity area was, however, significantly smaller in EL than in HL or JL (Table 4).

Discussion

Influence of initial biomass on species specific transpiration and water use efficiency

The known large differences in growth rate between European larch (EL), Japanese larch (JL) and hybrid larch (HL) (Pâques et al. 2013) render experimentation as well as interpretation of biomass data and constitutive wood anatomy (Anfodillo et al. 2013; Piermattei et al. 2020) of young saplings challenging. Using younger HL plants resulted in an intermediary starting biomass, instead of much larger individuals than the parental species if older HL would have been used. The variation within the initial biomass, and thus the size of the plants, clearly had a significant effect on the final total needle surface, on the transpiration rate and on the relative biomass increase. Including the initial biomass into the ANCOVA allowed taking into account the size differences among plants. Still, relative biomass increase was significantly higher for HL than for EL, even though HL saplings were only in their 3rd growing season, compared to EL, which was in its 4th growing season. The faster growth of HL compared to one or both of its parents is generally observed (Pâques et al. 2013; Greenwood et al. 2015) but depends on parental varieties used. In sites, where (summer) water supply is not limited, JL growth can be close to that of HL (Philippe et al. 2016).

Transpiration rate per leaf surface was highest for EL and lowest for JL. The latter result is similar to a tendency for higher stomatal conductance, shown by Matyssek and Schulze (1987) for EL compared to JL, with HL showing intermediate values. Initial biomass clearly affected needle surface area and eventually total plant transpiration rate but we found no statistically significant impact on transpiration efficiency, suggesting that the differences in initial biomass did not affect the relative amounts of biomass growth vs. transpiration. As far as we know, there is no comparison of transpiration efficiency (TE) estimates either for EL and JL or their hybrid in the literature. The only estimate for a *Larix* species was for *L. occidentalis* with a TE at 3.6 g/kg (Marshall and Zhang 1994). For *Pseudotsuga menziesii*, which is in the same subfamily Laricoidae as *Larix*, Smit and van den Driessche (1992) estimated a TE of 6.2 g/kg. For other species from the Pinaceae family, low TE around 2.5 g/kg have been estimated for different *Abies* species (Becker 1977), whereas Guehl et al. (1995) estimated a TE of 5.3 g/kg to 6.6 g/kg for *Pinus pinaster*. Compared to the latter estimates, EL saplings (4.0 g/kg) appeared to have a medium, and JL saplings (6.1 g/kg) a rather high TE. Accordingly, leaf matter δ^{13}C values were more negative for EL (suggesting lower WUE at leaf level), medium for HL and less negative for JL. This again is similar to the results from Matyssek and Schulze (1987), who showed a tendency for higher WUE of HL and JL compared to EL at the leaf level. Kloeppel et al. (1998) compared five different *Larix* species, including *L. decidua*, to a second sympatric evergreen conifer species growing on the same site, and all *Larix* species showed a tendency towards more negative δ^{13}C values, thereby suggesting a lower WUE at the leaf level. Similarly, Gower and Richards (1990) showed more negative δ^{13}C values for *L. occidentalis* and *L. lyallii* also compared to sympatric evergreen conifers (*Pinus*, *Abies* or *Tsuga* species). Overall, our results corroborate that EL has a relatively low WUE compared to HL and JL (but also compared to other conifer species) due to a higher transpiration or stomatal conductance per leaf surface and also lower growth.

Species specific physiological responses to drought

There are no detailed ecophysiological studies comparing drought responses of the two parental *Larix* species and their hybrid; however, the drought response of EL has been regularly compared to other conifer species (e.g., Eilmann and Rigling 2012; Schuster and Oberhuber 2013; Peters et al 2019). Eilmann and Rigling (2012) showed that the growth of EL was fairly low during drought, and that EL lacked the ability to recover from drought. This was confirmed by Schuster and Oberhuber (2013), who showed a stronger decline in the basal area index of EL (compared to *P. abies* and *P. sylvestris*) in response to a decrease in soil moisture. Similarly, Lévesque et al. (2013, 2014a) showed that EL was more vulnerable to drought (in terms of ring growth) than *P. sylvestris* and *Pinus nigra*. Overall, the literature suggests that the growth of EL is strongly affected by soil drought (George et al. 2016). The drought stress applied in our study had a significant effect on stem diameter (radial growth) in all species, but a lower absolute biomass increment and relative biomass was only significant in JL and even more so in HL. These results are in line with a stronger dependence of HL ring growth to precipitation compared to EL, as observed by Oleksyn and Fritts (1991). Marchal et al. (2019) had shown a stronger plasticity of HL in response to soil water deficit in terms of ring width compared to EL and JL, where more stressful conditions did decrease its level of performances to a level comparable to parental species. In our study, only EL showed no significant reduction in transpiration rate under drought. In contrast, HL and JL had a significant decrease in transpiration, which was proportionally higher compared to biomass increase, resulting in an increase in transpiration efficiency with drought. Lévesque et al. (2014b) showed highest increase in WUE between a mesic and a xeric site for EL, compared to evergreen conifer species. Here, the strong drought effect on growth for HL was mainly due to a strong reduction in the transpiration rate, suggesting a higher stomatal sensitivity of HL to drought. Drought stressed saplings of JL showed a significant decrease in needle surface area, whereas HL did show a quite similar needle surface area in control and stressed trees. Maintenance of a large leaf surface by HL under drought can explain the observed severe reduction in transpiration rate and, therefore, implies stronger stomatal control of HL. Thus, a significant increase of transpiration efficiency was only observed for HL and JL, the increase being much stronger for JL. These results suggest that EL was better able to maintain stomatal opening under soil water deficit and thus maintain photosynthesis. At the leaf level, HL showed the biggest shift in δ^{13}C values (nearly 2‰) under drought, indicating either strong stomatal closure or an increase in photosynthesis. As the latter is unlikely under drought conditions, the δ^{13}C measurements confirm the strong stomatal reaction to drought by HL. Several authors suggest an anisohydric stomatal behaviour of EL in response to soil water deficit; compared to evergreen conifer species (Anfodillo et al. 1998; Swidrak et al. 2013; Klein 2014; Leo et al. 2014), it is able to maintain high transpiration under drought conditions, thus keeping stomata open (Streit et al. 2014) even at very low levels of leaf water potential. We confirm this behaviour at the whole plant level, as EL maintained its transpiration rate under drought. Furthermore, the strong reduction in transpiration of HL under drought would indicate its isohydric behaviour to increasing soil water deficit. However, during a mild drought stress, anisohydric behaviour of HL might be possible, since HL solely showed a significant decrease in relative water content in sapwood under the impact of prolonged drought stress. The observed relative water loss of 15% in drought stressed HL corresponds to more than 40% of loss in hydraulic conductivity (Rosner et al. 2019), which is quite considerable for conifers. Bhusal et al. 2020 recently reported that JL shows both isohydric and anisohydric drought response, however, with a stronger tendency towards isohydry.

In response to drought, not only the production of the wood volume is reduced, but anatomical traits, such as the diameter and cell wall thickness of tracheids, are also affected. Reduction in lumen diameters and an increase in cell wall thickness are important anatomical features for a trees' drought adaptability, because higher wall/lumen relationships would promote greater mechanical support to stems while preventing xylem cell collapse (Hacke et al. 2001; Domec et al. 2008; Rosner et al. 2018). Towards the end of the drought stress experiment, lumen diameters in the sapwood of stressed HL and JL decreased much more than in EL. In HL, a trend in cell wall thickness increase was also observed. These structural modifications indicate either an earlier production of transition wood, which has a higher hydraulic safety than earlywood and latewood (Dalla-Salda et al. 2014) or intra-annual density fluctuations such as the formation of a "false ring". Since the decrease in radial lumen diameter was more observed in individuals with higher δ^{13}C and transpiration efficiency, we suggest that anatomical modifications were triggered by physiological processes such as the earlier closure of the stomata. Intra-annual density variations in earlywood ("false rings") develop under the impact of early summer drought. When water is again available, the tree starts to produce wood that resembles earlywood (Fritts 1976; Wimmer et al. 2000; Rosner et al. 2018; George et al. 2019). Sugar investment for cell wall thickening and lignification exceeds other growth processes (Cartenì et al. 2018) and the production of "false rings" that resemble latewood cells in their cell wall thickness might be related to biomechanical demands of the tree. Concerning the production of "false rings", HL seems to be the most sensitive of the investigated larch species and if this behaviour is relevant for recovery after drought, further investigation in this context is needed.

Investment in hydraulic safety impacts reaction to drought in larch species

Structural modifications in wood developed to prevent or minimize cavitation include: pit structure (Pittermann et al. 2006; Delzon et al. 2010; Bouche et al. 2014), conduit wall reinforcement by decreasing lumen diameter or by increasing wall thickness (Hacke et al. 2001; Domec et al. 2009) and possibly also differences in cell wall lignification (Rosner et al. 2018). One of the anatomical traits that shows a positive correlation with embolism resistance is the conduit wall reinforcement, i.e., the cell wall thickness to span ratio $(t/b)^2$, because it influences the resistance against hydraulic failure (Hacke et al. 2001). For example, in mature *Larix decidua* trunks, $(t/b)^2$ values of earlywood increase toward the apex, where water potential is known to become more negative (Prendin et al. 2017). In our study, there were differences among species in $(t/b)^2$ measured in the tangential direction of non-stressed sapwood, with EL showing significantly higher values than HL and JL. This suggests that the hydraulic safety of EL was superior to the other two species in terms of resistance against cavitation (Rosner et al. 2016), which would allow for the observed higher transpiration per leaf area under drought for EL. Higher growth, as generally observed in juvenile HL and JL (Pâques et al. 2013; Caudullo et al. 2018), comes at the cost of lower hydraulic safety, because tracheids become bigger (and thus more prone to cavitation) with distance from the apex (Anfodillo et al. 2013; Piermattei et al. 2020). To take into account such structure–function relationships, future experiments should include same-age as well as same-size saplings across species, so that age and size effects can be clearly separated from species differences.

The significantly smaller pit cavities we observed for EL compared to HL and JL might be related to higher hydraulic safety; however, this anatomical trait has so far not been tested as a proxy for vulnerability to cavitation. Pit anatomy plays an important role in cavitation resistance and the most commonly used proxy is the torus overlap (Delzon et al. 2010; Bouche et al. 2014). Torus overlap values obtained in our study suggest that juvenile larch wood is hydraulically quite safe when compared to other conifer species (Bouche et al. 2014). We found a trend for higher torus overlap in JL followed by EL and HL. However, regarding conduit wall reinforcement in the tangential direction (Rosner et al. 2016), JL was the most cavitation sensitive species. The higher torus overlap might be thus a compromise between hydraulic efficiency and hydraulic safety in this species.

Overall, EL had higher hydraulic safety, in terms of conduit wall reinforcement and pit cavity size, than JL and HL, which comes at the cost of slower growth. This corresponds to the classification of EL as an anisohydric species (Anfodillo et al. 1998; Swidrak et al. 2013; Klein 2014; Leo et al. 2014), which can cope with lower water potentials than isohydric species (McDowell et al. 2008), but their wood must be constructed more safely to avoid implosion (Hacke et al. 2001). From the constitutive structure–function point of view, wood of EL is designed to keep stomata open at more negative water potentials than JL or HL, because cavitation occurs at lower water potentials. Accordingly, EL had a lower conductivity loss, indicated by a tendency to higher RWC (Rosner et al. 2019), compared to JL and HL.

Conclusions

Our study showed that young saplings of the three larch species (EL, JL and HL) adopted different strategies towards drought. As hypothesised, the slower growth and hydraulically safer wood of EL allows anisohydric behaviour under drought stress, whereas the less safe wood design in JL and HL demands stronger stomatal control and an isohydric strategy. Both JL and HL had an increase in transpiration efficiency induced by drought, but in HL, the increase was due to a strong reduction in transpiration per leaf surface, whereas in JL it was due to a reduction in the leaf surface. HL was the most reactive to soil water availability; it showed the highest decrease in transpiration rate, had significantly lower relative water contents in sapwood and started to produce denser wood much earlier than the other two species. We hypothesised higher drought plasticity during growth in HL, for now, we cannot reject this hypothesis, but we conclude for the HL analysed in the present study, that their strategy towards drought stress was inherited from JL rather than from EL. The anisohydric drought response strategy of EL could allow a range shift under climate change from its native range to higher elevations or more northern regions. The observed higher growth of HL, even under drought, and its higher resistance against diseases, supports its inclusion in pure and mixed lowland plantations in regions, where EL is native. HL is a "man-made" construction obtained by controlled crosses between both parents selected for their superiority. Using connected pedigrees at intra- and interspecific levels through crossing of common parents such as in diallel mating design would allow drawing a clearer conclusion on the genetic determinism of the observed differences between hybrids and parental species. To investigate a species' strategy for its response to drought we suggest both quantitative anatomical and physiological investigations, whereby the relative water loss of the sapwood is a fast and easily assessable functional trait.

Author contribution statement LEP provided plant material; OB set up the green house experiment and supervised GB, who performed the physiological experiments. GB wrote the first report on the physiology results. SR, AS and NG were responsible for the anatomical trait dataset design and supervision of NS, who did the practical histological work. OB performed statistical data analyses for all traits. SR and NS did statistical data analyses for selected anatomical traits. NS and SR produced the figure plots. The first draft of the manuscript was written by NS and AS. SR, OB, LEP and NG reviewed this draft in several rounds. After input of the editor and two reviewers, all authors contributed to two revised versions. All authors agree on the content of this manuscript.

Supplementary Information The online version contains supplementary material available at https://doi.org/10.1007/s00468-021-02129-4.

Acknowledgements This work is supported by the START Project [Y-728-B16] from the Austrian Science Fund (FWF). We like to thank Cyril Buré, who managed the experimental setup and running of the robotic system. We also thank the entire PHARE ecophysiology group of the SILVA unit, who helped with the final harvest. Isotopic measurements were performed by C. Hossann at SILVATECH facility (Structural and functional analysis of tree and wood facility) located at the research center INRAE Nancy-Lorraine. SILVATECH facility is supported by the French National Research Agency through the Laboratory of Excellence ARBRE (ANR-11-LABX-0002-01). Prof. Lüttge and two anonymous reviewers are thanked for their useful comments on a first and second version of the manuscript.

Funding Open access funding provided by University of Natural Resources and Life Sciences Vienna (BOKU).

Availability of data and material Datasets will be provided to colleagues on demand.

Declarations

Conflict of interest None declared.

References

Allen CD, Breshears DD, McDowell NG (2015) On underestimation of global vulnerability to tree mortality and forest die-off from hotter drought in the Anthropocene. Ecosphere 6:1–55. https://doi.org/10.1890/ES15-00203.1

Anfodillo T, Rento S, Carraro V, Furlanetto L, Urbinati C, Carrer M (1998) Tree water relations and climatic variations at the alpine timberline: seasonal changes of sap flux and xylem water potential in *Larix decidua* Miller, *Picea abies* (L.) Karst, and *Pinus cembra* L. Ann Des Sci For 55:159–172. https://doi.org/10.1051/forest:19980110

Anfodillo T, Petit G, Crivellaro A (2013) Axial conduit widening in woody species: a still neglected anatomical pattern. IAWA J 34:352–364. https://doi.org/10.1163/22941932-00000030

Becker M (1977) Contribution to the study of transpiration and adaptation to drought in young conifers: Studies on three circum-mediterranean firs (*Abies alba*, *A. nordmanniana* and *A. numidica*)". Ann Sci Forest 34:137–158. https://doi.org/10.1051/forest/19770203

Beikircher B, Ameglio T, Cochard H, Mayr S (2010) Limitation of the Cavitron technique by conifer pit aspiration. J Exp Bot 61:3385–3393. https://doi.org/10.1093/jxb/erq159

Bhusal N, Lee M, Reum Han AR, Han A, Kim HS (2020) Responses to drought stress in *Prunus sargentii* and *Larix kaempferi* seedlings using morphological and physiological parameters. Forest Ecol Manag 465:118099. https://doi.org/10.1016/j.foreco.2020.118099

Bogeat-Triboulot MB, Buré C, Gerardin T, Chuste PA, Le Thiec D, Hummel I, Durand M, Wildhagen H, Douthe C, Molins A, Galmés J, Smith HK, Flexas J, Polle A, Taylor G, Brendel O (2019) Additive effects of high growth rate and low transpiration rate drive differences in whole plant transpiration efficiency among black poplar genotypes. Environ Exp Bot 166:103784. https://doi.org/10.1016/j.envexpbot.2019.05.021

Bouche PS, Larter M, Domec J-C, Burlett R, Gasson P, Jansen S, Delzon, (2014) A broad survey of hydraulic and mechanical safety in the xylem of conifers. J Exp Bot 65:4419–4431. https://doi.org/10.1093/jxb/eru218

Boudru M. 1986. Forêt et silviculture. Sylviculture appliquée. Ed. Presses Agronomiques de Gembloux. Gembloux. 122–131.

Breda N, Huc R, Granier A, Dreyer E (2006) Temperate forest trees and stands under severe drought: a review of ecophysiological responses, adaptation processes and long-term consequences. Ann For Sci 63:625–644. https://doi.org/10.1051/forest:2006042

Cartenì F, Deslauriers A, Rossi S, Morin H, De Micco V, Mazzoleni S, Giannino F (2018) The physiological mechanisms behind the earlywood-to-latewood transition: a process-based modeling approach. Front Plant Sci 9:1053. https://doi.org/10.3389/fpls.2018.01053

Caudullo G., Nakada R., Da Ronch F. 2018. *Larix kaempferi* (Lambert) Carrière, 1856. III. Monographien von Baum- und Straucharten. 1. Nadelbaumarten der temperierten Klimazonen. Enzyklopädie der Holzgewächse – 70. Erg. Lfg. 01/18. https://doi.org/10.1002/9783527678518.ehg2017003

Cazaux JP, Chevalier R, Gilbert JM, Ginisty C (1993) Le mélèze hybride en plantation: résultats provisoires sur 17 sites en France. Informations techniques du Cemagref nr 91:8. https://hal.inrae.fr/hal-02576271. Assessed on 26 Mar 2021

Dalla-Salda G, Fernández ME, Sergent A-S, Rozenberg P, Badel E, Martinez-Meier A (2014) Dynamics of cavitation in a Douglas-fir tree-ring: transition-wood, the lord of the ring? J Plant Hydraul 1:e-0005. https://doi.org/10.20870/jph.2014.e005

Delzon S, Douthe C, Sala A, Cochard H (2010) Mechanism of water-stress induced cavitation on conifers: bordered pit structure and function support the hypothesis of seal capillary-seeding. Plant Cell Environ 33:2101–2111. https://doi.org/10.1111/j.1365-3040.2010.02208.x

Dietrich L, Delzon S, Hoch G, Kahmen A (2019) No role for xylem embolism or carbohydrate shortage in temperate trees during the severe 2015 drought. J Ecol 107:334–349. https://doi.org/10.1111/1365-2745.13051

Domec JC, Lachenbruch B, Meinzer FC, Woodruff DF, Warren JM, McCulloh KA (2008) Maximum height in a conifer is associated with conflicting requirements for xylem design. Proc Natl Acad Sci (USA) 105:12069–12074. https://doi.org/10.1073/pnas.0710418105

Domec JC, Warren JM, Meinzer FC, Lachenbruch B (2009) Safety factors for xylem failure by implosion and air-seeding within roots, trunks and branches of young and old conifer trees. IAWA J 30:101–120. https://doi.org/10.1163/22941932-90000207

Eilmann B, Rigling A (2012) Tree-growth analyses to estimate tree species drought tolerance. Tree Physiol 32:178–187. https://doi.org/10.1093/treephys/tps004

Feichtinger LM, Eilmann B, Buchmann N, Rigling A (2014) Growth adjustments of conifers to drought and to century-long irrigation. For Ecol Managem 334:96–105. https://doi.org/10.1016/j.foreco.2014.08.008

Fritts H (1976) Tree rings and climate. Academic Press

Geburek T (2002) *Larix decidua*. III. Monographien von Baum- und Straucharten. 1. Nadelbaumarten der temperierten Klimazonen. Enzyklopädie der Holzgewächse – 29. Erg. Lfg. 9/02

George J-P, Grabner M, Karanitsch-Ackerl S, Mayer K, Weißenbacher L, Schueler S (2016) Genetic variation, phenotypic stability, and repeatability of drought response in European larch throughout 50 years in a common garden experiment. Tree Physiol 37:33–46

George J-P, Grabner M, Campelo F, Karanitsch-Ackerl S, Mayer K, Klumpp RT, Schueler S (2019) Intra-specific variation in growth and wood density traits under water-limited conditions: Long-term-, short-term-, and sudden responses of four conifer tree species. Sci Total Environ 660:631–643. https://doi.org/10.1016/j.scitotenv.2018.12.478

Gower ST, Richards JH (1990) Larches: deciduous conifers in an evergreen world. Bioscience 40:818–826. https://doi.org/10.2307/1311484

Granier A, Bréda N, Biron P, Villette S (1999) A lumped water balance model to evaluate duration and intensity of drought constraints in forest stands'. Ecol Modeling 116:269–283. https://doi.org/10.1016/S0304-3800(98)00205-1

Greenwood MS, Roth BE, Maass D, Irland LC (2015) Near rotation-length performance of selected hybrid larch in Central Maine, USA. Silvae Genet 64(1–2):73–80. https://doi.org/10.1515/sg-2015-0006

Guehl J-M, Nguyen-Queyrens A, Loustau D, Ferhi A (1995) Genetic and environmental determinants of water-use efficiency and carbon isotope discrimination in forest trees. In: Sandermann H, Bonnet-Masimbert M (eds) Eurosilva: Contribution to forest tree physiology. results from eurosilva projects. les colloques. Editions Colloques de l'INRA, Paris, pp 297–321. https://hal.inrae.fr/hal-02779528. Assessed on 26 Mar 2021

Haasemann W (1986) Untersuchungen zur Ökologie der Europäerlärche, Japanerlärche und ihrer Hybriden im Nass-Trockenfeld. Beitr Forstwirtschaft 20:184–188

Hacke UG, Sperry JS, Pockman WT, Davis SD, McCulloch KA (2001) Trends in wood density and structure are linked to prevention of xylem implosion by negative pressure. Oecologia 126:457–461. https://doi.org/10.1007/s004420100628

Huang WW, Fonti P, Larsen JB, Raebild A, Callesen I, Pedersen NB, Hansen JK (2017) Projecting tree-growth responses into future climate: A study case from a Danish-wide common garden. Agric For Meteor 247:240–251. https://doi.org/10.1016/j.agrformet.2017.07.016

Jansen S, Geburek T (2016) Historic translocations of European larch (*Larix decidua* Mill.) genetic resources across Europe—a review from the 17th until the mid-20th century. Forest Ecol Managem 379:114–123. https://doi.org/10.1016/j.foreco.2016.08.007

Klein T (2014) The variability of stomatal sensitivity to leaf water potential across tree species indicates a continuum between isohydric and anisohydric behaviours. Funct Ecol 28:1313–1320. https://doi.org/10.1111/1365-2435.12289

Klein T, Cahanovitc R, Sprintsin M, Herr N, Schiller G (2019) A nation-wide analysis of tree mortality under climate change: Forest loss and its causes in Israel 1948–2017. For Ecol Manag 432:840–849. https://doi.org/10.1016/j.foreco.2018.10.020

Kloeppel BD, Gower ST, Treichel IW, Kharuk S (1998) Foliar carbon isotope discrimination in *Larix* species and sympatric evergreen conifers: A global comparison. Oecologia 114:153–159

Leo M, Oberhuber W, Schuster R, Grams TEE, Matyssek R, Wieser G (2014) Evaluating the effect of plant water availability on inner alpine coniferous trees based on sap flow measurements. Eur J For Res 133:691–698. https://doi.org/10.1007/s10342-013-0697-y

Lévesque M, Saurer M, Siegwolf R, Eilmann B, Brang P, Bugmann H, Rigling A (2013) Drought response of five conifer species under contrasting water availability suggests high vulnerability of Norway spruce and European larch. Global Change Biol 19:3184–3199. https://doi.org/10.1111/gcb.12268

Lévesque M, Rigling A, Bugmann H, Weber P, Brang P (2014a) Growth response of five co-occurring conifers to drought across a wide climatic gradient in central Europe. Agric For Meteor 197:1–12. https://doi.org/10.1016/j.agrformet.2014.06.001

Lévesque M, Siegwolf R, Saurer M, Eilmann B, Rigling A (2014b) Increased water-use efficiency does not lead to enhanced tree growth under xeric and mesic conditions. New Phytol 203:94–109. https://doi.org/10.1111/nph.12772

Marchal A, Schlichting CD, Gobin R, Balandier P, Millier F, Munoz F, Pâques LE, Sanchez Rodriguez L (2019) Deciphering hybrid larch reaction norms using random regression. G3 Genes Genomes Genet 9(1):21–32. https://doi.org/10.1534/g3.118.200697

Marshall JD, Zhang JW (1994) Carbon-isotope discrimination and water-use efficiency in native plants of the north central Rockies. Ecology 75:1887–1895. https://doi.org/10.2307/1941593

Masson G (2005) Autoécologie des essences forestières. Lavoisier, Paris

Matyssek R, Schulze E-D (1987) Heterosis in hybrid larch (*Larix decidua* x *leptolepis*). II Growth characteristics. Trees 1:225–231. https://doi.org/10.1007/BF01816820

McDowell NG, Allen CD (2015) Darcy's law predicts widespread forest mortality under climate warming. Nat Clim Change 5:669–672. https://doi.org/10.1038/NCLIMATE2641

McDowell N, Pockman WT, Allen CD, Breshears DD, Cobb N, Kolb T, Plaut J, Sperry J, West A, Williams DG, Yepez EA (2008) Mechanisms of plant survival and mortality during drought: why do some plants survive while others succumb to drought? New Phytol 178:719–739. https://doi.org/10.1111/j.1469-8137.2008.02436.x

McDowell NG, Williams AP, Xu C, Pockman WT, Dickman LT, Sevanto S, Pangle R, Limousin J, Plaut J, Mackay DS, Ogée J, Domec J-C, Allen CD, Fisher RA, Jiang X, Muss JD, Breshears DD, Rauscher SA, Koven C (2016) Multi-scale predictions of massive conifer mortality due to chronic temperature rise. Nat Clim Change 6:295–300. https://doi.org/10.1038/NCLIMATE2873

Mencuccini M, Binks O (2015) Tall leafy conifers lose out. Nat Clim Change 5:625–626

Nagamitsu T, Matsuzaki T, Nagasaka K (2018) Provenance variations in stem productivity of 30-year-old Japanese larch trees planted in northern and central Japan are associated with climatic conditions in the provenances. J For Res 23:270–278. https://doi.org/10.1080/13416979.2018.1490520

Obojes N, Meurer A, Newesely C, Tasser E, Oberhuber W, Mayr S, Tappeiner U (2018) Water stress limits transpiration and growth of European larch up to the lower subalpine belt in an inner-alpine dry valley. New Phytol 220:460–475. https://doi.org/10.1111/nph.15348

Oleksyn J, Fritts HC (1991) Influence of climatic factors upon tree rings of *Larix decidua* and *L. decidua* × *L. kaempferi* from Pulawy. Poland Trees 5:75–82. https://doi.org/10.1007/BF00227488

Pâques LE, Foffová E, Heinze B, Lelu-Walter MA, Liesebach M, Philippe G (2013) Larches (*Larix* sp.). In: Pâques, L.E. (eds.) Forest tree breeding in Europe. Managing Forest Ecosystems, 25. Springer, Dordrecht, p 52

Peters RL, Speich M, Pappas C, Kahmen A, von Arx G, Graf Pannatier E, Steppe K, Treydte K, Stritih A, Fonti P (2019) Contrasting stomatal sensitivity to temperature and soil drought in mature alpine conifers. Plant Cell Environ 42:1674–1689. https://doi.org/10.1111/pce.13500

Philippe G, Buret C, Matz S, Pâques LE (2016) Composition of hybrid larch (*Larix* × *eurolepis* Henry) forest reproductive materials: How much does hybrid percentage affect stand performance? New For 47:541–564. https://doi.org/10.1007/s11056-016-9530-z

Piermattei A, von Arx G, Avanzi C, Fonti P, Gärtner H, Piotti A, Urbinati C, Vendramin GG, Büntgen U, Crivellaro A (2020) Functional relationships of wood anatomical traits in Norway spruce. Front Plant Sci. https://doi.org/10.3389/fpls.2020.00683

Pittermann J, Sperry JS, Hacke UG, Wheeler JK, Sikkema EH (2006) Inter-tracheid pitting and the hydraulic efficiency of conifer wood: The role of tracheid allometry and cavitation protection. Am J Bot 93:1265–1273. https://doi.org/10.3732/ajb.93.9.1265

Prendin AL, Petit G, Fonti P, Rixen C, Dawes MA, von Arx G (2017) Axial xylem architecture of *Larix decidua* exposed to CO2 enrichment and soil warming at the tree line. Funct Ecol 32:273–287. https://doi.org/10.1111/1365-2435.12986

R Core Team (2020) A Language and environment for Statistical Computing. R Foundation for Statistical Computing, Vienna, Austria. https://www.r-project.org. Assessed on 26 Mar 2021

Rosner S, Svetlik J, Andreassen K, Borja I, Dalsgaard L, Evans R, Luss S, Tveito OE, Solberg S (2016) Novel hydraulic vulnerability proxies for a boreal conifer species reveal that opportunists may have lower survival prospects under extreme climatic events. Front Plant Sci 7:1–14. https://doi.org/10.3389/fpls.2016.00831

Rosner S, Gierlinger N, Klepsch M, Karlsson B, Evans R, Lundqvist SO, Svetlik J, Borja I, Dalsgaard L, Andreassen K, Solberg S, Jansen S (2018) Hydraulic and mechanical dysfunction of Norway spruce sapwood due to extreme summer drought in Scandinavia. For Ecol Manag 409:527–540. https://doi.org/10.1016/j.foreco.2017.11.051

Rosner S, Johnson DM, Voggeneder K, Domec J-C (2019) The conifer-curve: Fast prediction of hydraulic conductivity loss and vulnerability to cavitation. Ann For Sci 76:82p15. https://doi.org/10.1007/s13595-019-0868-1

Rozenberg P, Chauvin T, Escobar-Sandoval M, Charpentier J-P, Pâques L (2020) Climate warming differently affects *Larix decidua* ring formation at each end of a French Alps elevational gradient. Ann For Sci 77:54. https://doi.org/10.1007/s13595-020-00958-w

Schneck V, Schneck D, Grotehusmann H, Pâques LE (2002) Testing of hybrid larch over a broad range of site conditions. In: Improvement of larch (*Larix* sp.) for better growth, stem form and wood quality, Proceedings of the International Symposium Improvement of larch (*Larix* sp.) for better growth, stem form and wood quality, Gap, FRA, pp119–126. https://hal.inrae.fr/hal-02763854. Assessed on 26 Mar 2021

Schuster R, Oberhuber W (2013) Drought sensitivity of three co-occurring conifers within a dry inner Alpine environment. Trees 27:61–69. https://doi.org/10.1007/s00468-012-0768-6

Smit J, van den Driessche R (1992) Root Growth and Water Use Efficiency of Douglas-Fir (*Pseudotsuga menziesii* (Mirb.) Franco) and Lodgepole Pine (*Pinus Contorta* Dougl.) Seedlings. Tree Physiol 11:401–410. https://doi.org/10.1093/treephys/11.4.401

Streit K, Siegwolf RTW, Hagedorn F, Schaub M, Buchmann N (2014) Lack of photosynthetic or stomatal regulation after 9 years of elevated CO_2 and 4 years of soil warming in two conifer species at the alpine treeline. Plant Cell Environ 37:315–326. https://doi.org/10.1111/pce.12197

Swidrak I, Schuster R, Oberhuber W (2013) Comparing growth phenology of co-occurring deciduous and evergreen conifers exposed to drought. Flora 208:609–617. https://doi.org/10.1016/j.flora.2013.09.004

Wimmer R, Strumia G, Holawe F (2000) Use of false rings in Austrian pine to reconstruct early growing season precipitation. Can J For Res 30(11):1691–1697. https://doi.org/10.1139/x00-095

Sasani *et al. Plant Methods* (2021) 17:17
https://doi.org/10.1186/s13007-021-00717-6

Plant Methods

RESEARCH

Open Access

Raman imaging reveals in-situ microchemistry of cuticle and epidermis of spruce needles

Nadia Sasani, Peter Bock, Martin Felhofer and Notburga Gierlinger*

Abstract

Background: The cuticle is a protective layer playing an important role in plant defense against biotic and abiotic stresses. So far cuticle structure and chemistry was mainly studied by electron microscopy and chemical extraction. Thus, analysing composition involved sample destruction and the link between chemistry and microstructure remained unclear. In the last decade, Raman imaging showed high potential to link plant anatomical structure with microchemistry and to give insights into orientation of molecules. In this study, we use Raman imaging and polarization experiments to study the native cuticle and epidermal layer of needles of Norway spruce, one of the economically most important trees in Europe. The acquired hyperspectral dataset is the basis to image the chemical heterogeneity using univariate (band integration) as well as multivariate data analysis (cluster analysis and non-negative matrix factorization).

Results: Confocal Raman microscopy probes the cuticle together with the underlying epidermis in the native state and tracks aromatics, lipids, carbohydrates and minerals with a spatial resolution of 300 nm. All three data analysis approaches distinguish a waxy, crystalline layer on top, in which aliphatic chains and coumaric acid are aligned perpendicular to the surface. Also in the lipidic amorphous cuticle beneath, strong signals of coumaric acid and flavonoids are detected. Even the unmixing algorithm results in mixed endmember spectra and confirms that lipids co-locate with aromatics. The underlying epidermal cell walls are devoid of lipids but show strong aromatic Raman bands. Especially the upper periclinal thicker cell wall is impregnated with aromatics. At the interface between epidermis and cuticle Calcium oxalate crystals are detected in a layer-like fashion. Non-negative matrix factorization gives the purest component spectra, thus the best match with reference spectra and by this promotes band assignments and interpretation of the visualized chemical heterogeneity.

Conclusions: Results sharpen our view about the cuticle as the outermost layer of plants and highlight the aromatic impregnation throughout. In the future, developmental studies tracking lipid and aromatic pathways might give new insights into cuticle formation and comparative studies might deepen our understanding why some trees and their needle and leaf surfaces are more resistant to biotic and abiotic stresses than others.

Keywords: Cuticle, Waxes, Epidermis, Norway spruce, Confocal Raman microscopy, Non-negative matrix factorization, Cluster analysis, Microchemistry

Background

Norway spruce (*Picea abies*) is the most abundant tree species in forests of the European Alps. High biomass accumulation, straight growth and a satisfactory rejuvenation account for its high popularity in forestry. Trees

---

*Correspondence: burgi.gierlinger@boku.ac.at
Department of Nanobiotechnology (DNBT), Institute for Biophysics, University of Natural Resources and Life Sciences (BOKU), Muthgasse 11-II, 1190 Vienna, Austria

are exposed to tough environmental conditions and various abiotic and biotic stresses, which assigns a key role to the needle cuticle as first line of defense [1–6]. It is composed of waxes and lipids [7]. The main function is to prevent the loss of water to the atmosphere, enable mechanical protection and to mitigate abiotic and biotic stresses such as UV light, changing relative humidity, temperature and microorganisms [4, 8–12]. A wealth of studies regarding cuticle chemistry, mechanics and functions is available. However, most of these studies used more or less destructive methods to study the cuticle. For description, SEM [13–21] and TEM [14, 16, 22–28] were extensively used, while chemistry was mostly examined after extraction procedures [21, 29–48]. These extraction and washing procedures destroy the native structure of the cuticle and do not allow insights into the spatial distribution of cuticle components. Recently, several reviews recognized this shortcoming and expressed the need for in-situ methods to link chemical with spatial information [49–51]. Yet, only a few studies use methods like confocal laser scanning microscopy [52, 53], IR or Raman microscopy [13, 54–56]. Unfortunately, none of these studies showed detailed information about the cuticular layers and their respective chemistry.

In this study, we show high resolution Raman images depicting the composition of the cuticle in the needles of Norway spruce (*Picea abies*). Microsections were mapped at two excitation wavelengths and polarization measurements were conducted to probe the alignment of the molecules with respect to the plant surface. The mappings include the cuticle together with the epidermal layer beneath and reveal chemical heterogeneity using univariate as well as multivariate data analysis.

Results

This study sheds new light on spruce cuticles by using high-resolution (~ 300 nm) confocal Raman spectroscopy (CRM). Cutting 20 µm thick microsections of the needles with a cryo-microtome enabled to scan pointwise across the native cuticle and including the underlying epidermal layer. Based on the acquired Raman spectra (hyperspectral data cube), chemical images were generated using univariate as well as multivariate data analysis (Fig. 1). Plotting the peak intensity of selected Raman bands (Fig. 2), grouping the Raman spectra based on their similarity using cluster analysis (Fig. 3) and retrieving the purest chemical components using the unmixing approach Non-negative matrix factorization (NMF) (Fig. 4) revealed the chemically different regions and the corresponding Raman spectra. The endmember spectra from non-negative matrix factorization (NMF) were compared with spectra of pure references to proof the assignment of the Raman bands. Due to high sample fluorescence (with 532 nm), we used 785 nm excitation for the Raman imaging experiments. But we also include 532 nm measurements, which show the potential of laser polarization to retrieve preferred alignments of the molecules in the outer region of the cuticle (Fig. 5).

Integrating specific Raman bands to highlight chemical differences

The very outer epicuticular wax layer is displayed by integrating the Raman band at 1120 cm^{-1}, while the whole cuticle shows up by integrating the CH$_2$ bend at 1440 cm^{-1} [57] (Fig. 2a). The spectrum of the outermost epicuticular wax layer shows two pronounced bands at 1122 cm^{-1} and 1062 cm^{-1} (Fig. 2b). The sharpness of these bands is indicative of a crystalline, highly ordered state. Below the cuticle two sharp bands are discovered at 1490 cm^{-1} and 1463 cm^{-1} and their integration displays pointwise accumulations of Calcium oxalate deposits (Fig. 2c, d), as Calcium oxalate monohydrate (Caox) shows strong Raman bands at 1498 cm^{-1}, 1474 cm^{-1} and 902 cm^{-1} [58]. In all spectra of the cuticle (Fig, 2b, d) a strong band is found at 1603 cm^{-1}, which can be attributed to aromatic ring stretching vibrations [59]. Integration of this band reveals that aromatic components play a role in the cuticle as well as in the underlying epidermal layer (Fig. 2e, f). Integrating the neighboring band at 1632 cm^{-1} highlights the upper cuticle and protrusions towards the epidermal layer (Fig. 2e). Integrating the other aromatic bands at 1567 cm^{-1} and 1660 cm^{-1}, displays the upper and lower epidermal layer, respectively (Fig. 2e). Hence, the different integrations and derived average spectra (Fig. 2e, f) show that aromatics are found in all layers, but their composition changes. The spectra of the epidermal layers (Fig. 2f) show additionally bands at e.g. 380 cm^{-1} and 1094 cm^{-1}, which can be assigned to cellulose [60]. Integrating the 380 cm^{-1} band depicts the epidermal layer and plant cell wall spectra are derived with strong aromatic bands at 1600 cm^{-1} and 1175 cm^{-1} (Fig. 2g, h). Integration of the 860 cm^{-1} band is commonly used for visualization of pectin [61], but in these spectra this band is too weak or overlapped by other components to be used for pectin imaging.

Multivariate approaches: analyzing all bands at once

Cluster analysis

Multivariate data analysis methods have the advantage to analyze the whole wavenumber region (hyperspectral data cube) at once, instead of focusing on selected bands. Cluster analysis extracts pixels based on their spectral similarity and displays chemically similar regions (clusters) and their average spectra (Fig. 3). Based on the results by band integration, a division into more than four clusters (water, waxes, cuticle, epidermal layer) to detect

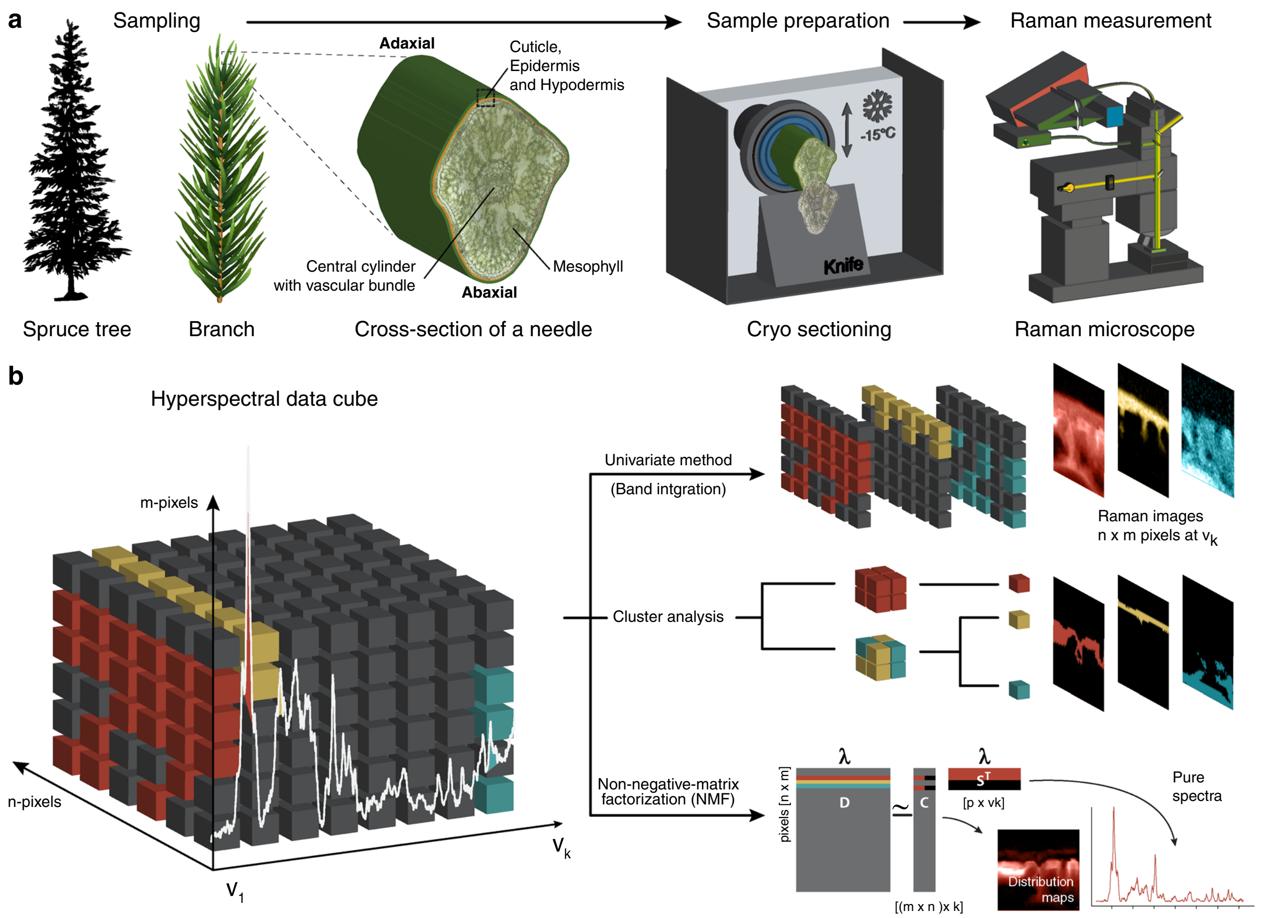

Fig. 1 Raman imaging of native plant cuticles. **a** After sampling the needles are kept frozen, also during cutting of microsections with the cryo-microtome. Cross sections (20 µm thick) are scanned using a Confocal Raman microscope. The region of interest included the adaxial cuticle together with the underlying epidermal layer. **b** The resulting hyperspectral data cube is analysed using three different approaches: Univariate band integration, clustering spectra based on similarity and retrieving the most pure components based on Non-negative-matrix-factorizations

differences in chemistry within the cuticle and epidermal layer was expected. From the analysis based on four to eight clusters, we finally show the results based on seven clusters (Fig. 3 and Additional file 1: Fig. S1) to include the most chemically different regions. The waxy layer on the upper side (cluster 1) is clearly distinguished from the lower cuticle (cluster 2) (Fig. 3a, b). Within the cuticle the Calcium oxalate deposits are included and only differentiated by further subclustering of the lower cuticular layer (Additional file 1: Fig. S1). The average spectrum shows beside the Calcium oxalate bands also bands attributed to aromatics and lipids and the distribution seems more layer like (Fig. 3c, d). Within the epidermal layer three clusters are separated with decreasing intensity of the aromatic 1175 cm^{-1} contribution and increasing signal of the carbohydrates (1095 cm^{-1}, 380 cm^{-1}) (Fig. 3c, d). Cluster 5 represents the lower epidermal layer and shows a typical secondary cell wall spectrum with carbohydrates and aromatics. All retrieved cluster average spectra include many different bands and components: in the upper layers, lipids are mixed with aromatics, below these, Calcium oxalate is mixed with lipids and aromatics and in the epidermal layer on the bottom, aromatics are mixed with carbohydrates (Fig. 3).

Non-negative-matrix factorization (NMF)

In a next step, an unmixing algorithm, Non-negative-matrix factorization (NMF) was applied to retrieve the purest spectral signatures of the different components together with their distribution [62]. These purest component spectra are called endmember (EM) spectra and are compared to spectra of reference compounds to verify components and Raman band assignments (Fig. 4 and Table 1). The outer epicuticular wax layer

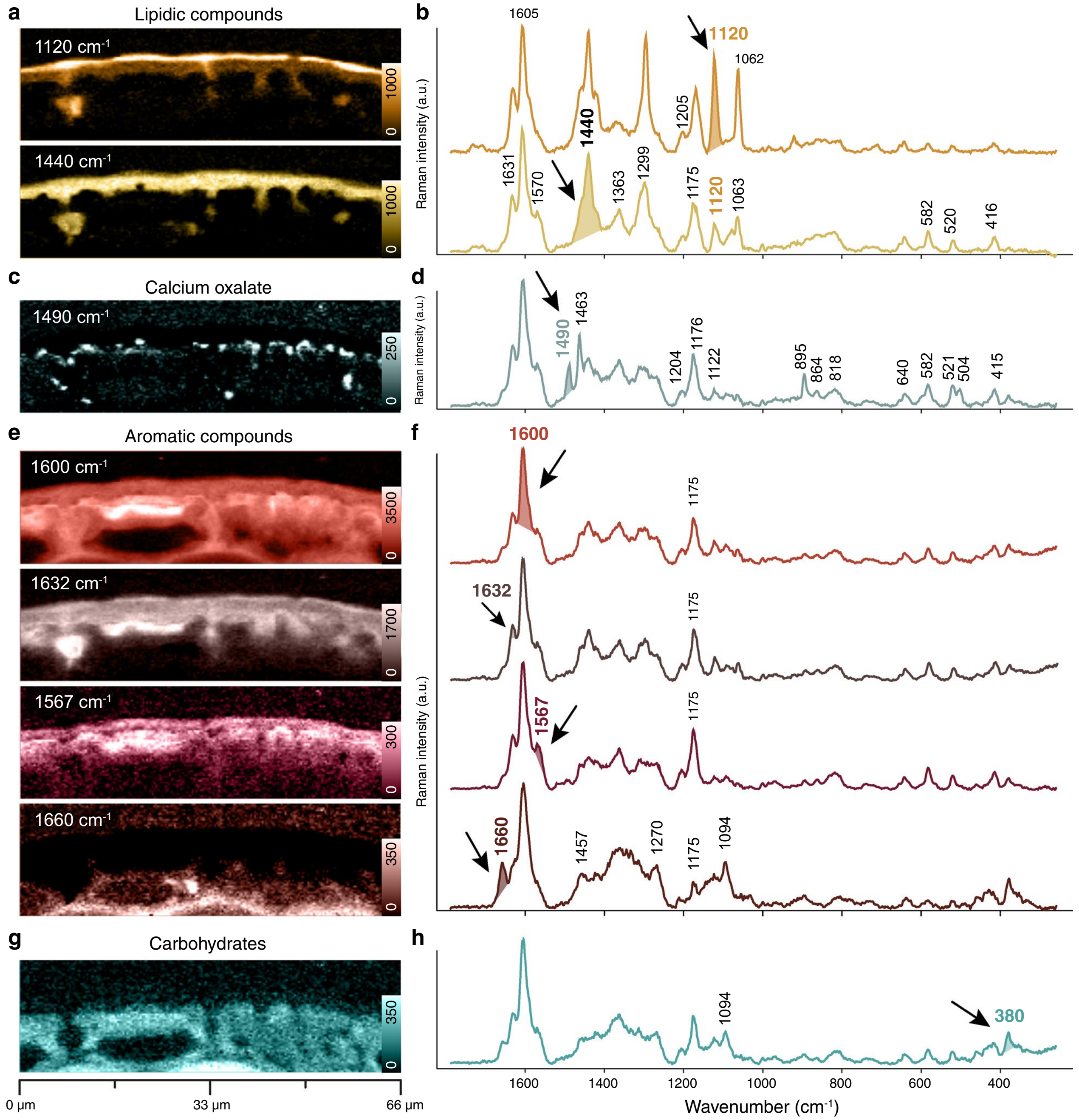

Fig. 2 Raman imaging of the cuticle of Norway spruce based on band integration and extracted average spectra of the visualized chemically different regions **a** The outer lipidic layers are visualized by integrating the band at 1120 cm^{-1} and 1440 cm^{-1} and **b** the extracted average spectra confirm the lipidic character, but also include bands attributed to aromatics. **c** Integrating the band at 1490 cm^{-1} visualizes a pointwise accumulation of Calcium oxalate **d** as confirmed by the bands at 1490, 1463 and 895 cm^{-1}. **e** Integrating different aromatic bands shows their distribution throughout the cuticle and epidermal layer and **f** extracted average spectra confirm that different aromatic components play a role **g** Integrating the characteristic cellulose band at 380 cm^{-1} displays the lower cuticle and **h** the derived average spectrum confirms carbohydrates together with aromatics

of the cuticle is distinguished by EM1 and the spectrum includes typical bands of crystalline waxes (doublet at 1122 and 1063 cm^{-1}) as also observed in solid 1-hexadecanol (Fig. 4a, b). EM2 displays calcium oxalate as almost all bands match with a spectrum of pure calcium oxalate (Fig. 4c, d). Accumulations are often

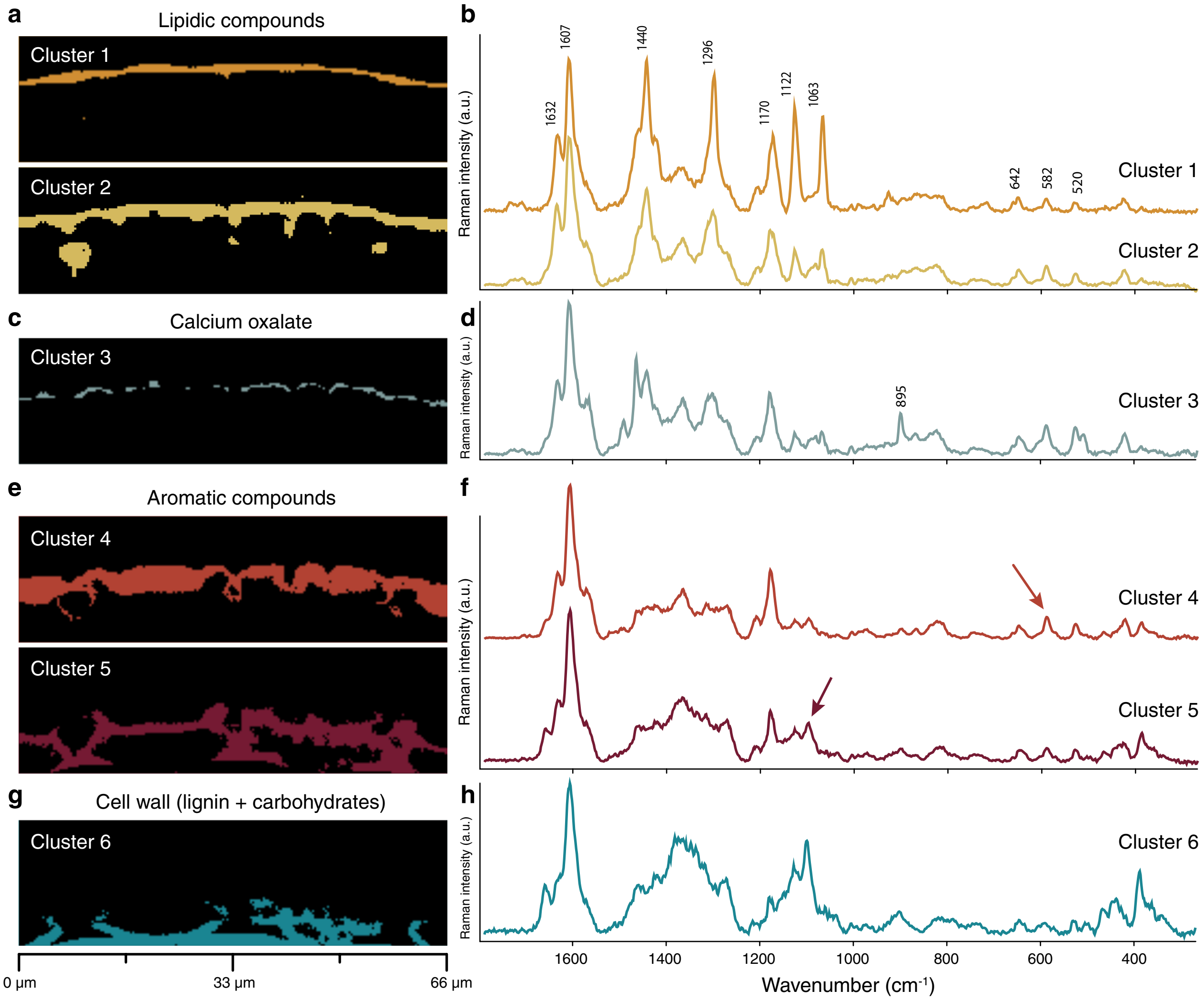

Fig. 3 Cluster analysis performed on the hyperspectral dataset of spruce cuticle (same as shown in Fig. 2). **a**, **b** Two outer lipidic clusters (1 and 2) are distinguinshed. **c**, **d** Subclustering the lower lipidic layer displays the Calcium oxalate accumulation (see also Additional file 1: Fig. S1). **e**–**h** Epidermal layer is divided into three clusters based on changes in amount and composition of aromatic components and carbohydrates

pointwise and mainly below the lipidic layer and a few protrusions in between the epidermal cells-similar to that observed by band integration (Fig. 2c, d). EM3 represents the lipidic layer below the wax layer and the spectrum shows beside lipid bands strong aromatic signals, which partly coincide with Kaempferol (Fig. 4e, f). EM4 highlights the upper epidermal layer and the strongest aromatic bands coincide with the bands of coumaric acid. EM 4 and EM 5 were mutually excluding each other. EM 5 reflects lignin and shows highest concentration in the middle lamella between the epidermal cells. EM6 finally displays secondary cell walls of the epidermal cells with strong carbohydrate bands (1378 cm^{-1}, 1120 cm^{-1}, 1095 cm^{-1}) and less lignin (1600 cm^{-1}) (Fig. 4g, h). Overall, the unmixing method results in more pure component spectra, but still aromatic contributions are revealed in all of them, reflecting the intimate mixing of aromatics with lipids and carbohydrates.

Polarization dependent intensity changes probe molecular orientation

Most Raman microscopes work with linear-polarized lasers. Acquiring spectra with different laser polarization direction (0° and 90° with respect to the sample/molecule orientation, Fig. 5a) detects whether chemical components are ordered or not. Two subsequent measurements were run on the same area: one image scan with the laser

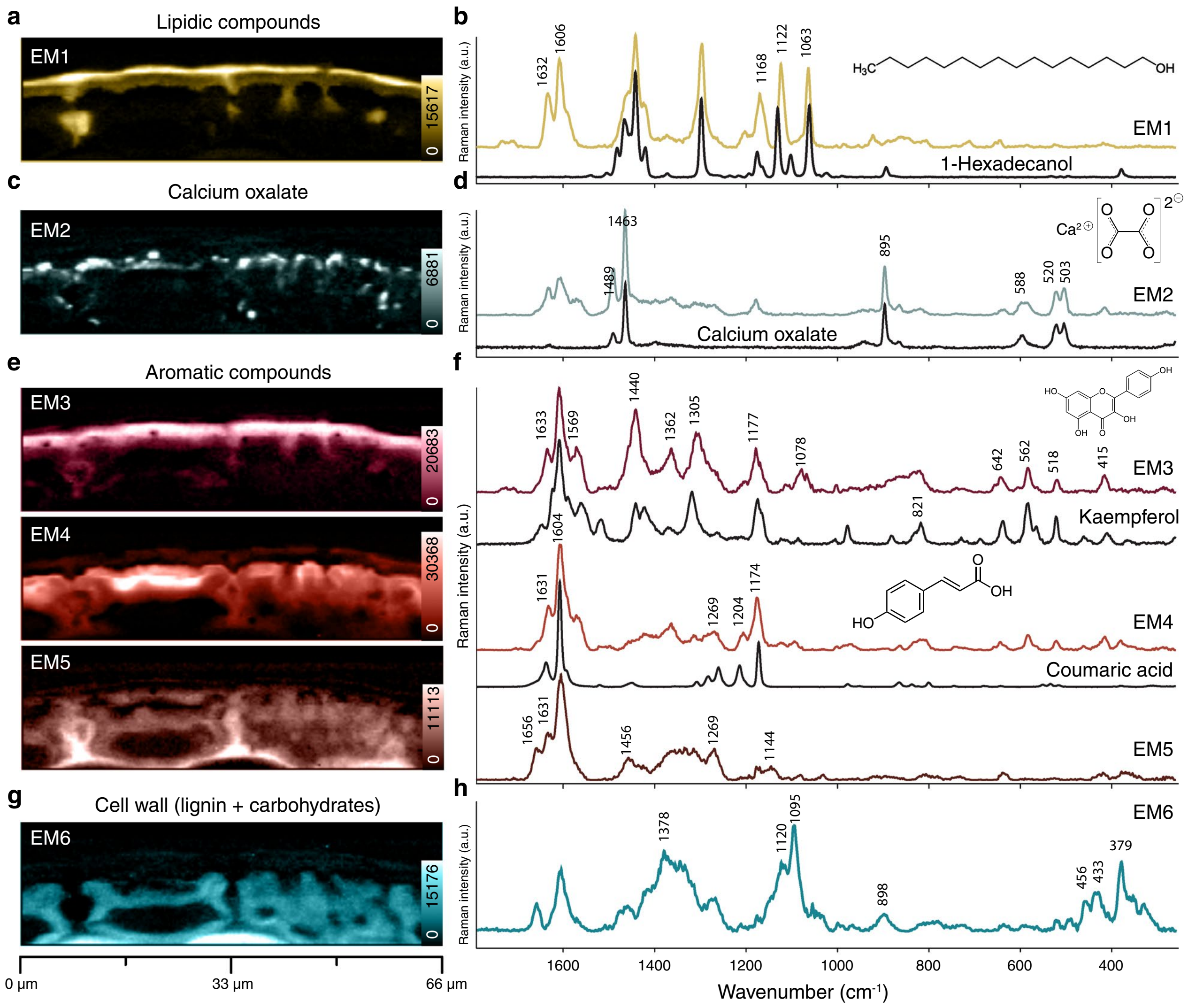

Fig. 4 Non-negative matrix factorization analysis of the cuticle of Norway spruce. **a–h** Shown are abundance maps depicting the distribution of the six end members. End members spectra are compared with spectra of pure reference compounds. The brightest color corresponds to the highest intensity

polarization aligned in parallel to the cuticle of the needle and the other perpendicular to it (Fig. 5a). As the 532 nm laser can induce artefacts in the spectra of subsequent measurement [62], mappings were started with either parallel or perpendicular laser polarization to estimate any potential damage. Although a notable increase in background attributed to the second measurement was seen in the spectra (Fig. 5b), there were no signs of laser degradation. Regardless of which polarization was used first, the spectra differed in the same way between polarization runs. The spectra of the outermost wax layer differ with respect to parallel (0°) and perpendicular (90°) laser polarization. The C–H stretches of waxes (~ 2900 cm^{-1}) were captured when the laser polarization was parallel (red spectrum), while C–C stretching of waxes and aromatic ring stretches were most intense with perpendicular orientation (blue spectrum) (Fig. 5b). A similar orientation dependence was recorded on neat fatty acids (see Additional file 1: Fig. S2), showing either the C–H stretching (~ 2900 cm^{-1}) or "in-line" modes (CH_2-twisting, C–C stretching) intensified if chains are aligned parallel to each other and the laser. In the cuticular layer underneath no polarization dependence was observed. The spectra were identical (Fig. 5b), proofing also that no laser damage occurred. Thus, orientation of lipids and aromatics is proven in the epicuticular wax layer, while in the layer underneath no preferred alignment of the molecules is detected (Fig. 5c).

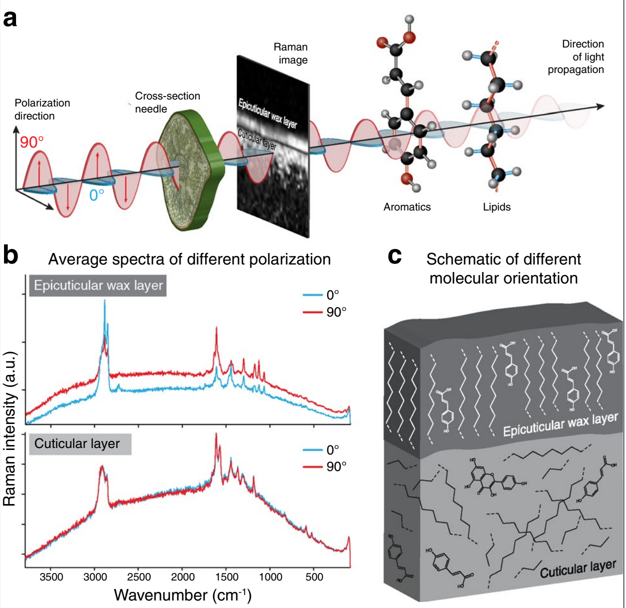

Fig. 5 Probing molecule orientation in spruce cuticle by mapping with different laser polarization. **a** The same region of interest was mapped with laser polarization direction parallel (0°) and perpendicular (90°) with respect to the cuticle surface **b** Raman spectra are extracted selectively from the epicuticular wax layer and the underneath cuticular layer. In the top layer higher intensities are observed for C–H stretches of waxes (2900 cm^{-1}) at 0° laser polarization (blue spectrum), while C–C stretching of waxes and aromatic ring stretches are most intense with 90° (red spectrum). In the cuticular layer beneath no orientation dependence is observed as the spectra are identical. **c** Schematic representation of the orientation of waxes and coumaric acid in the cuticle. The aliphatic chains and aromatic rings are oriented perpendicular to the surface in the wax layer, while compounds in the cuticular layer are not oriented, comprising an amorphous structure

Discussion

Assessing cuticle chemistry by techniques like NMR, gas chromatography or mass spectrometry requires depolymerization prior to analysis and the native cuticle structure is destroyed [63]. For a complete understanding of this outer protective layer more in-situ methods and studies are needed to reveal the chemistry in context with microstructure [49–51]. In this work, we show that confocal Raman microscopy probes the cuticle in the native state and gives access to aromatics, lipids, carbohydrates and minerals at once. The acquired hyperspectral dataset is the basis to image the chemical heterogeneity using univariate- and multivariate data analysis (Fig. 6). Mapping with changed laser polarization direction even probes the orientation of the molecules with respect to the plant surface (Fig. 5). One major advantage of Raman point-by-point mapping is the fact that one has not to rely only on “images”. Behind every pixel is a molecular fingerprint, and average, cluster and endmember spectra help to interpret and verify the chemical composition of distinguished layers, interfaces and agglomerations.

Table 1 Assignment of different components of the cuticle. Wavenumbers derived from NMF

Wavenumber (cm^{-1})			Assignment
Wax	Cutin	CaOx	
1734	1723		ν C=O (fatty acid esters)
1712	1707		ν C=O (coumaric acid, midchain carbonyls)
	1654		ν C=C (anthoxanthins)
1632	1634		ν C=C (coumaric acid, stilbenes); Φ8 (anthoxanthins)
1607	1607		Φ8 (all rings)
	1570		ν C=O (anthoxanthins)
		1488	ν C=O (Calcium oxalate) [107]
		1463	ν C=O (Calcium oxalate) [107]
1455			δ C–H (aliphatic chains) [57]
1441	1440		δ C–H (aliphatic chains) [57]
1423			δ C–H (aliphatic chains) [57]
1372			γ_w CH_2 (aliphatic chains) [57]
	1362		Φ20a (anthoxanthins(A-ring))
	1308		γ_t CH_2 (aliphatic chains) [57]
1295			γ_t CH_2 [57]
1201	1205		Φ7a (coumaricacid)
	1177		Φ9a (anthoxanthins with p-subst. C-Ring)
1169			Φ9a (coumaric acid)
1123			ν C–C (aliphatic chains)
	1112		
	1077		ν C–C (aliphatic chains)
1062	1066		ν C–C (aliphatic chains)
	1001		Φ12 (stilbenes)
921			ν C–C (aliphatic chains)
		895	ν_s C–C + δ O–C=O (Calcium oxalate) [107]
864	870	864	ν C–C + γ_r CH_2 (aliphatic chains) [108]; (Calcium oxalate)
	831		ν C–C + γ_r CH_2 (aliphatic chains) [108]
	738		(Kaempferol)
710			
653			
642	642		Φ6a (anthoxanthins (A-ring))
		593	Water libration (Calcium oxalate) [107]
	582		Φ1 (anthoxanthins (A-ring))
524		520	ν Ca-O + ν C–C (Calcium oxalate) [107]
	518		Φ6b (anthoxanthins (A-ring))
		503	
418	414		

ν: stretching; δ: bending; γ_t: twisting; γ_r: rocking, γ_w: wagging; Φ: ring mode in Varsanyi notation [59]

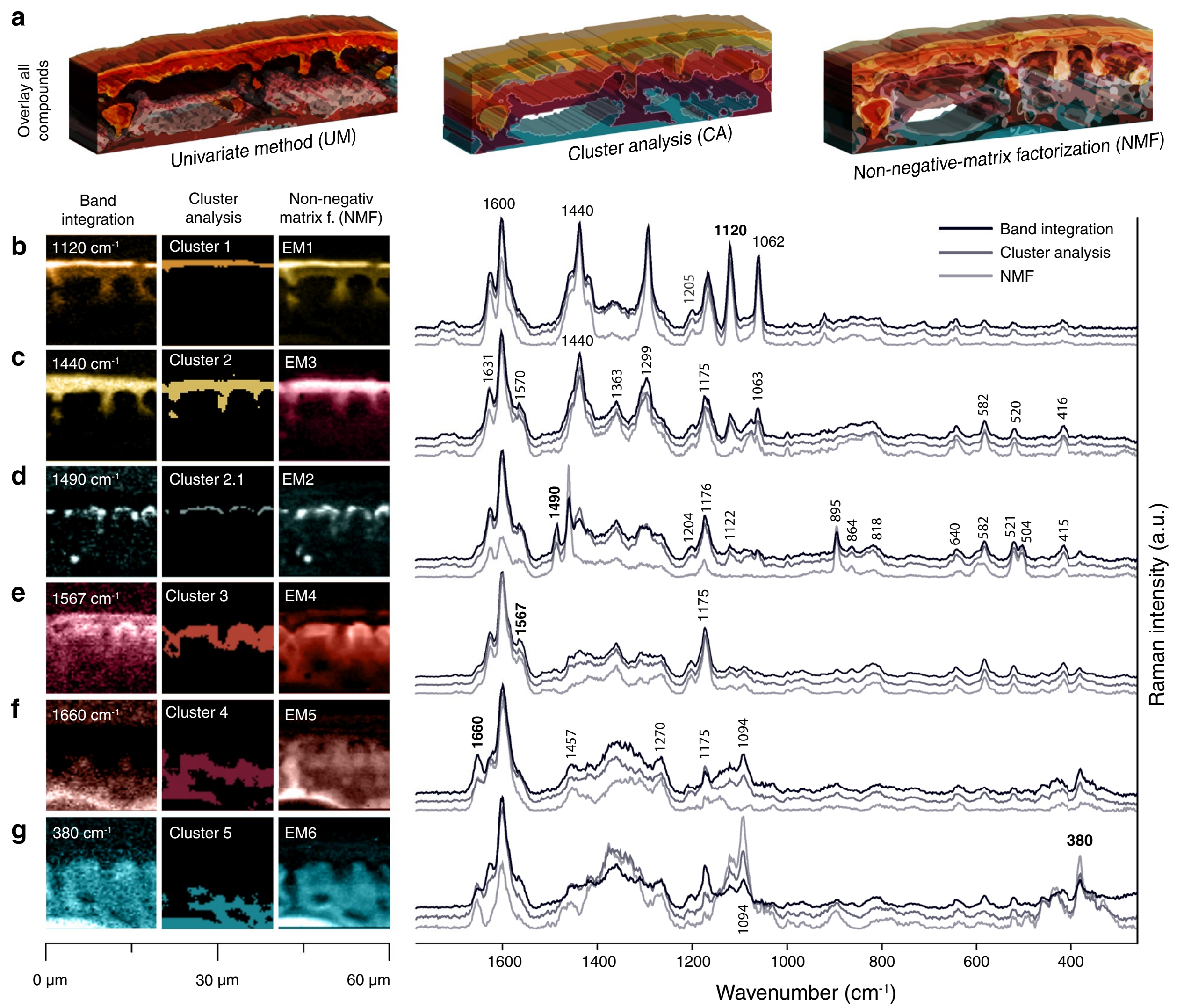

Fig. 6 Comparison of the three different methods (Band integration, Cluster analysis, and Non-negative-matrix factorization (NMF)). **a** Overlay of all compounds from each method. The Raman images were rasterized, and 3D extruded for better visualizing the overlaying nature of the different compounds. **b–g** Sections of the Raman images (Figs. 2, 3, 4) from each method to compare each extracted layer. On the right the corresponding spectra

Which aromatic components are represented in cuticle Raman spectra?

The phenolic nucleus gives rise to strong Raman bands, which can be used to image the distribution of aromatics along the whole cuticle and epidermis. The strongest band at 1605 cm^{-1} is present throughout the whole cuticle and epidermis. It indicates aromatic rings in conjugation with C=C/C=O [64, 65]. In needles, coumaric acid, stilbenes and flavonoids are reported [66–69]. To assign specific bands to these different aromatics and track them selectively, a critical survey of reference spectra is necessary (Additional file 1: Fig. S3–S9). Coumaric acid has prominent bands at 1636, 1606 and 1171 cm^{-1}, which have also been detected in EM4 (Fig. 4e, f and Table 1). Comparing the EM4 spectrum with different coumaric acid derivatives (Additional file 1: Fig. S3), we can clearly assign it to coumaric acid. Our interpretation therefore is that the majority of coumaric acid is present as individual molecules and that only minor parts may be esterified. The band at 1175 cm^{-1} represents aromatic CH bending of para-substituted rings (Φ9a) and is therefore not unique to coumaric acid. Benzoic acid and its derivates show this band as well as flavonoids with para-substituted C-rings. Of all substitution variants, only 4-methoxybenzoic acid achieves a satisfactorily overlap (see Additional file 1: Fig. S4).

The strong Raman band around 1570 cm^{-1} serves as a marker band for anthoxanthins (flavonoids) [70] and can be found in the whole cuticle (Fig. 2e, f, EM3 in Fig. 4e, f), except for the epicuticular wax layer. While the band at 1175 cm^{-1} hints to a para-substituted C-Ring (Φ_{para} 9a), the bands at 642 ($\Phi_{asym\text{-}tetra}$ 6a), 582 ($\Phi_{asym\text{-}tetra}$ 1), and 520 cm^{-1} ($\Phi_{asym\text{-}tetra}$ 6b) show an A-ring with two hydroxyl groups (Table 1). Such a flavone would be kaempferol and its reference spectrum matches well with the EM3 spectrum (Fig. 4e, f, and Additional file 1: Fig. S5). The spectrum of (+)-Catechin, the flavanol we tested, cannot be matched with the cuticle spectra. Stilbenes, previously found in needles of spruce (piceatannol, astringin or isorhapontin) [66, 71] have a characteristic Raman line at 1000 cm^{-1} ($\Phi_{sym\text{-}tri}$ 12) [57, 72]. Interestingly, spectra of pinosylvin and pinosylvin monomethylether can be matched best, although these are not reported for spruce needles, while those of resveratrol, piceatannol, isorhapontigenin and astringin show additional bands and based on these cannot be fitted to the cuticle spectra (see Additional file 1: Fig. S6). Stilbenes have large Raman cross-sections enabling their identification even in small amounts [72]. Due to only a weak band at 1000 cm^{-1} being present in the cuticle spectra, we conclude that the amount of stilbenes must be rather low. Also picein and piceol were found in spruce needles in comparatively high amounts [66], but can be fitted to the spectra only with low intensity. Dehydroabietic acid cannot be fitted to the spectrum at all, and therefore does not occur in the needle's cuticle (see Additional file 1: Fig. S7).

Lignin is well separated from cuticle-specific phenolics by the band at 1660 cm^{-1} (Figs. 2e, f, 4e, f) which is attributed to lignin monolignols [64, 73]. Contrary to [74], we do not regard the band at 1630 cm^{-1} as a lignin band, instead we primarily assign it to coumaric acid (ethylenic C=C stretch) (see Table 1).

Epicuticular waxes align with coumaric acid perpendicular to the surface

Epicuticular waxes build the outer layer of plant cuticles to prevent transpiration and water loss [7]. They are composed of long-chain aliphatic compounds with several functional groups (e.g. hydroxyls and esters). Hydroxy derivatives of nonacosan-10-ol, e.g. nonacosane-4, 10-diol, nonacosane-7, 10-diol or nonacosane-10, 13-diol have been identified in needle waxes from various conifers, e.g. *Picea abies* [75], *Pinus radiata* [37] or *Juniperus scopularum* [47]. Epicuticular waxes can appear film-like or as crystalloids [76], but always in their solid crystal forms [16, 17]. The Raman spectra of the epicuticular wax layer (Fig. 2a, b: 1120 cm^{-1}, Fig. 3a, b: cluster 1, and Fig. 4a, b: EM1) show sharp bands typical for crystalline substances with limited degrees of rotational freedom [57]. The characteristic doublet at 1122 and 1063 cm^{-1} is only visible in solid wax (see Additional file 1: Fig. S8). Reference spectra of C_{16} and C_{18} alcohols match well, yet this does not confirm the chain length because aliphatic chains with similar carbon counts display similar spectra. The epicuticular wax bands are always observed together with aromatic bands, even in the EM spectrum based on the unmixing NMF-algorithm (Fig. 4, EM1). The strong bands at 1632 and 1606 cm^{-1} are of aromatic origin and the bands at 1201 and 1169 cm^{-1} point to coumaric acid. Such hydroxycinnamic acids protect the underlying tissue by absorbing UV-light [77]. This and the fact that we revealed even a preferred alignment of the aromatic rings along with the aliphatic chains (Fig. 5) suggests strong association of aromatics and waxes.

To derive the orientation of molecules with respect to the laser polarization direction is an unparalleled advantage of Raman microscopy. The polarizability of a normal mode is anisotropic and therefore differs with the incident angle of the electromagnetic field [57, 59] (Fig. 5a). Laser polarization experiments have been used to estimate the orientation of cellulose fibrils in the cell wall [78, 79] as well as to reveal different orientations of a lignin monomer [64]. In this study, polarization measurements show a clear orientation of waxes in the epicuticular layer, but no orientation preference in the subjacent cuticle layer (Fig. 5b, c). A model of perpendicular oriented waxes with respect to the surface of the cuticle is shown in [76]. Based on Raman we show that this orientation can actually be found in the native cuticle and moreover that aromatic rings are oriented the same way (Fig. 5c). The bands at 1600 and 1173 cm^{-1} are more intense when the laser is oriented perpendicular to the surface (Fig. 5b). In para-substituted rings, both modes Φ8a and Φ9a have the greatest polarizability change along the line connecting both substituent atoms, so that this result clearly demonstrates that the ring, and therefore coumaric acid, is aligned parallel to the aliphatic chains in the wax layer (Fig. 5c).

Amorphous cuticle layer is impregnated with aromatics

Cutin is a polymer created from saturated hydroxylated aliphatic acids, usually a mixture of C_{16} and C_{18} ω-hydroxyl fatty acids [80, 81]. Midchain hydroxyl or epoxy groups are reported as well as additional end-groups like aldehyde, ketone and carboxyl [82–85]. In addition, glycerol, glyceryl esters, coumaric and ferulic acids have been reported [86–89]. This results in a wide variety of chemical types depending on organ (leaf or fruit), location (adaxial or abaxial surfaces of the same leaf) and stages of maturity [51, 85, 89]. The Raman spectrum of the cutin layer shows the expected bands for fatty acids (1440 and 1305 cm^{-1}), which appear broader than the corresponding peaks of waxes in the overlying layer. Sharp bands indicating crystallinity are missing (Fig. 2a, b: 1440 cm^{-1}, Fig. 3a, b: cluster 2, Fig. 4e, f: EM3, and Additional file 1: Fig. S8) and polarization measurements yield similar spectra (Fig. 5b). This suggests aliphatic chains in a multitude of conformations without any preferential orientation. Indeed, cutins can be viewed as a non-ordered mesh with cavities filled by other cuticle components [63]. Such components can be phenolics as confirmed by aromatic bands found in the cutin layer (Fig. 4e, f, EM3). The marker band for flavonoids at 1570 cm^{-1} is most pronounced in this layer (Fig. 6b, 2nd row) and Kaempferol was found to match the spectrum very well (Fig. 4f and Additional file 1: Fig. S5). A weak signal of stilbenes is also observed, but their actual structure remains unclear. Lipid spectra include always aromatic bands, corroborating the idea that clusters of aromatics are inserted into the cutin network [90, 91].

Calcium oxalate accumulates at the interface between cuticle and epidermal layer

Calcium oxalate crystals exist in many plants and they appear in many tissues and organs. They are diverse in shape, size, number of crystals and hydration [92]. They play various roles such as cation regulation, CO_2 and H_2O supply, tissue support, herbivore protection, detoxification, and light manipulation [93–103].

In spruce needles, calcium oxalate was found in vascular bundles, in intercellular spaces, inside of cell walls and as many tiny pure calcium oxalate crystals in the cuticular layer [96, 104]. Our Raman approach detects these crystals in a layer-like fashion below the cutin layer (Fig. 6b, third row). The EM3 spectrum proves with sharp bands at 1490, 1463, 895 and 503 cm^{-1} calcium oxalate monohydrate as the main component (Figs. 4c, d, 6b), but still aromatic bands are present from the surrounding tissue. The crystals enhance light transmission and probably most of the "pure" crystals are smaller than 600 nm, which is about the limit of depth resolution. The Calcium oxalate crystals are mainly at the interface between the lipidic cuticle and the aromatic rich upper epidermal layer, but some are also visualized in the lumen of the epidermal cells (Fig. 6b).

Outer epidermal cell wall: enhancing protection by aromatics

Bound flavonoids and their derivatives and other aromatics have been detected in the cell walls of the outer epidermal cell layer of spruce needles by confocal laser scanning microscopy [105]. In this work, Raman imaging reveals in the periclinal upper epidermal cell wall a strong accumulation of aromatics, which leads to a separation from the lower epidermal layer by cluster analysis and NMF (Fig. 6b). The high intensity of the aromatic band 1600 cm^{-1} (Fig. 2e) comes from the fact that coumaric acid as well as flavonoids accumulate in this region (Fig. 4, EM 4). Raman bands of cellulose together with almost zero signal of lipid components confirm the epidermis classification of this layer. In a recently published review, the authors suggest "the plant cuticle as a lipidized epidermal cell wall region" [51]. Based on our Raman imaging results the epidermal layer seems not to get "lipidized", but "aromatized". Thus, if this special "epidermal" layer with high accumulation of aromatics should belong to the cuticle, a definition based on coumaric acid would be necessary. Regardless of definition, our results show the importance of aromatics in linking the lipidic cuticle and carbohydrate rich epidermal layer as the same aromatic components are found in both layers. The high accumulation of flavonoids in this outwards epidermal cell wall, will enhance protection of the plant surface. Flavonoids and other aromatics in the epidermal layer of cuticles are reported to mediate a highly complex UV-screening mechanisms of Norway spruce needles [105].

Polysaccharides detected in the epidermal layer, but hardly in the cuticle

Raman spectroscopy is sensitive to molecular vibrations of any chemical compound. However, differentiating carbohydrates in secondary plant cell walls by Raman spectroscopy can be challenging due to relatively small Raman cross sections when compared to conjugated aromatic molecules [64]. Whether carbohydrates should be regarded as authentic cuticle constituents is still debated in the field [51]. The main polysaccharides in the cuticle of Norway spruce, found by immune-gold labeling, were cellulose, mannans and pectin [27]. They were also found in similar quantities in the cuticles of tomato [14], eucalyptus, poplar and prunus [23]. Additionally, in the case of tomato, no preferred orientation or crystallinity of the polysaccharides could be found [14]. For visualization of pectin and cellulose, the Raman marker bands at 856 cm^{-1} [106] and 380 cm^{-1} can be used [61]. Pectin could not be unambiguously identified, because its marker band overlapped with another band (864 cm^{-1}) probably originating from an aromatic compound. The Signal of cellulose was mainly found in the walls of the epidermal cells, but was hardly seen in the cuticle.

Potential of Raman imaging: univariate and/or multivariate analysis?

Probing the cuticle and epidermis together, all chemical components at once and in context with the microstructure results in "comprehensive pictures" of the plant surface (Fig. 6a). The hyperspectral dataset offers many possibilities for data analysis and we show and discuss one univariate and two multivariate approaches. All three separated the wax layer from the underlying cuticle and highlighted the adjacent periclinal epidermal layer as chemically different from the rest of the epidermis (Fig. 6a).

The first approach is univariate data analysis by integrating the individual Raman bands to produce intensity-dependent heat maps and extracting average spectra based on intensity thresholds for detailed analysis (Fig. 2). As it is fast and captures well chemical heterogeneity band integration was also used in the first Raman imaging experiments on wood [15, 109] and is nowadays included in almost every Raman imaging study. On our examples band integration worked well to highlight the waxy layer on top of the cuticle based on the sharp crystalline band at 1120 cm^{-1} in a similar way to the unmixing algorithm NMF (Fig. 6b, EM1). Cluster analysis separates the wax layer (cluster 1) from the cuticle, as with this approach no intensity threshold (overlay of layers) is possible, and spectra are sorted by spectral similarity either in one or the other cluster (Fig. 6b, c). The derived cluster average spectrum reflects directly the chemistry of the displayed region, similar like average spectra derived based on band integration. On contrast, NMF-analysis calculates a set of endmember spectra, which are combined to reproduce the experimental spectra of the plant sample at every pixel [62]. The spectra of the waxy layer derived from the three approaches are very similar and include bands of lipids, but also aromatics (e.g. 1606 and 1632 cm^{-1}). As the unmixing approach is not capable of finding a "pure" wax spectrum within all the pixels, we can conclude that lipids and coumaric acid are tightly intermixed. A conclusion, which would not be possible based on the other two approaches. This tight association is also seen in EM3, in which flavonoids and coumaric acids are together with lipids in the amorphous cuticle layer (Fig. 6c). These results are in full agreement with reported clusters of aromatics that are inserted into the cutin network [90, 91].

On the Calcium oxalate layer beneath, the performance of three approaches differed most (Fig. 6d). Although seven clusters have been chosen (Additional file 1: Fig. S1), the detection of the crystals was only possible by subclustering. The NMF algorithm achieved the purest Calcium oxalate spectrum: lipid bands were absent and aromatic bands smaller compared to the other two methods (Fig. 6c). The crystals are tiny and thus other components dominate the spectra in most of the pixels. So, if not known a priori and searched for with a marker band or continued with subclustering, it might be difficult to detect this layer by band integration and cluster analysis.

In contrast, the fact that aromatics play a role throughout the investigated plant surface, becomes immediately clear by integration of the strongest band at 1605 cm^{-1}, (aromatic rings in conjugation with C=C/C=O; [64, 65] (Fig. 2e, f). Band integration of the neighboring bands at 1660, 1635, and 1570 cm^{-1} highlights lignin, coumaric acid and flavonoids, respectively (Fig. 2e, f). Although different distributions are derived, overall intensities must be taken with care as the overlapping bands will influence each other. Peak fitting might be a solution for such overlapping bands, but pitfalls come along with this approach [110]. If components are present at some of the pixels more "purer" or at least with changing amounts, the unmixing algorithm results in endmembers, which are characteristic for flavonoids and coumaric acid (EM 4) or lignin (EM 5) and shows their distribution (Fig. 6e, f). The high accumulation of flavonoids in the periclinal epidermal cell wall was confirmed by all three methods (Fig. 6e). The distinction of the whole epidermal layer (including the upper "aromatized" layer) was only possible by NMF (EM5 lignin and EM6 cell wall) and integration of the cellulose band at 380 cm^{-1} (Fig. 6f, g). The cellulose integration image is noisy as the band is relatively weak. Carbohydrate bands often get overlapped by aromatic bands due to the high Raman cross section of conjugated aromatic molecules [64]. Cluster analysis separates the epidermal layer into three clusters (EM3-5)—due to the changing amount of aromatics and carbohydrates (Fig. 6e–g).

Our example on the spruce needle shows that the quick band integration approach works very well as long as bands of the different components do not overlap too much, and bands are not too weak. The main component classes (waxes, lipids, aromatics, minerals, carbohydrates) can be tracked by finding marker bands. Cluster analysis groups similar spectra and results in chemically most different regions and thus does not necessarily track specific components. The NMF algorithm looks for the purest component spectra and models their distribution. The result are clear images and distinction of layers and endmember spectra coinciding best with spectra acquired from reference components (Additional file 1: Fig. S2–S8). This helped to attribute the bands to different components and their molecular vibrations (Table 1).

Conclusions

Raman imaging of the cuticle and epidermis probed all chemical components at once in context with the microstructure and gave new insights into spruce needle surfaces:

- A crystalline wax layer, with aliphatic chains and coumaric acid aligned perpendicular to the plant surface, is distinguished from the more amorphous lipidic cuticle, which is impregnated with coumaric acid and flavonoids.

- Aromatic components are co-located with lipids (within 300 nm) in the cuticle and wax layer as even endmember spectra derived by the NMF unmixing approach showed Raman bands of both component classes.
- Calcium oxalate crystals accumulate at the interface between the lipidic cuticle and the carbohydrate rich epidermis.
- The upper periclinal epidermal cell wall is distinguished by all three data analysis approaches as a chemically different layer due to the strong Raman signals of aromatics.

The aromatic impregnation of cuticle starts in the anticlinal middle lamellae of the epidermal cells and together with the strong periclinal cell wall impregnation it is reminiscent of the casparian strip. Looking with our approaches at different developmental stages of plant surfaces will give new insights into the development of the cuticle by tracking lipid and aromatic pathways during development.

The strong impregnation of the epidermal layer offers additional protection and Raman imaging now gives a comprehensive picture of both layers as well as the Calcium oxalate interface. Future comparative studies might help to answer why some trees and their needle and leaf surfaces are more resistant to biotic and abiotic stresses than others.

Materials and methods

Material and preparation

Four branches of a Norway spruce tree were received from Praxmar (Tyrol, 47° 09′ N/11° 07′ E, see also [111]). The harvest took place in August 2019 and samples were immediately frozen to -20 °C after harvesting. Needles on top of the branches were selected (young needle) and a piece of the center was cut out (see also Fig. 1a). These pieces were subsequently cut into 15–20 µm thick cross sections by a cryo-microtome (CM 3050 S, Leica Biosystems Nussloch GmbH, Germany). The sections were washed with distilled water afterwards and put on a standard microscopy glass slide with a drop of distilled water, covered with a standard microscopy coverslip (0.16 mm thick) and sealed with nail polish to prevent water evaporation during Raman imaging experiments.

Confocal Raman microscopy

We used a confocal Raman microscope (alpha300RA, WITec GmbH, Germany) with a 100 × oil immersion objective (NA 1.4, 0.17 mm with coverslip correction) (Carl Zeiss, Germany) to obtain Raman images from the aforementioned needle thin sections. A microscopical overview of every section was obtained and then suitable areas for measurement selected in the cuticle zone of the needle. A linear polarized (0°) $\lambda_{ex} = 785$ nm laser (WITec, Germany) and a $\lambda_{ex} = 532$ nm laser (WITec, Germany) were used for the experiments. The scattered Raman signal was detected with an optic multifiber (100/50 nm diameter, respectively) directed to a spectrometer UHTS30 (WITec, Germany) (600gmm^{-1} grating) and to a CCD camera (DU401DD/DU401BV, respectively) (Andor, Belfast, NorthIreland). The Control Four acquisition software (WITec, Germany) was used for control of the measurement. The laser power was set to 150 mW and integration time to 0.1 s for 785 nm experiments and to 44.7 mW and to 0.1 s for 532 nm experiments. No destructive effects of the laser on the samples were observed. A spectrum was taken every 0.3 µm to reach the maximum possible diffraction limited spatial resolution ($r = 0.61 \times \lambda/NA$). The maximum theoretical spatial resolution obtainable therefore was about 342 nm for the 785 nm laser and 230 nm for the 532 nm laser. Routinely, before starting the Raman measurements, calibration of the instrument to the silicon band of 520 cm^{-1} was performed.

Data analysis

Spectra were cropped (300–1800 cm^{-1}), cosmic rays removed and the baseline corrected before calculating Raman images by integrating specific bands (univariate), cluster analysis and non negative matrix factorization (NMF) using the WITec Project plus 4.1 software (WITec, Germany). By integrating specific Raman bands a fast overview about the chemical heterogeneity was achieved. Average spectra were extracted from selected regions of the images by using an intensity threshold to include only the pixels with signal of the Raman band of interest. Cluster analysis takes into account the whole wavenumber range and segments the hyperspectral dataset in clusters according spectral similarity. As a measure for the spectral similarity Euclidean distance was chosen. The analysis was performed with 4–8 clusters, and finally the results based on 7 clusters are shown. For control, a sub-clustering into another 2 clusters was performed within every cluster (Additional file 1: Fig. S1). Cluster average spectra were extracted for detailed analysis. To find the most pure components within the dataset the unmixing algorithm non negative matrix factorization (NMF) was applied. Hyperspectral images obey a natural chemically meaningful bilinear model, the Beer–Lambert law ($D = CS^T + E$) with D as the raw Raman image, S^t the matrix of pure spectra, C the stretched concentration profiles and E the error [112]. Thus, an unmixing algorithm aims to retrieve the pure components or endmember spectra and their concentration profile to be displayed distribution maps. NMF was calculated based on 4 to 8 endmembers (pure components) with up to 100,000 iterations and finally the results based on 7 endmembers are shown. Average spectra based on the integration approach, based on cluster analysis as well as endmember spectra from NMF are exported into OPUS 7.5 (Bruker, Germany) for further analysis and comparison with spectra acquired from reference components.

Supplementary Information

The online version contains supplementary material available at https://doi.org/10.1186/s13007-021-00717-6.

Additional file 1. Cluster analysis of spruce cuticle and reference Raman spectra of lipidic and aromatic components.

Acknowledgements

We thank Stefan Mayr and Andrea Ganthaler for sampling of the spruce needles. We want to express our gratitude to Tayebeh Saghaei for the extensive discussions leading to this manuscript.

Authors' contributions

NS made microsections and acquired hyperspectral data set. NS, NG performed univariate and multivariate data analysis PB did the polarization experiment, acquired reference Raman spectra and compared with sample spectra. NS, PB, MF made the Figures. NS, PB and NG wrote the manuscript. All authors read and approved the final manuscript.

Funding

Austrian Science Fund (FWF): START Project [Y-728-B16].

Availability of data and materials

The datasets used and/or analysed during the current study are available from the corresponding author on reasonable request.

Ethics approval and consent to participate

Not applicable.

Consent for publication

Not applicable.

Competing interests

The authors declare that they have no competing interests.

Received: 7 December 2020 Accepted: 28 January 2021

References

1. Dominguez E, Heredia-Guerrero JA, Heredia A. The plant cuticle: old challenges, new perspectives. J Exp Bot. 2017;68:5251–5.
2. Fernández V, Sancho-Knapik D, Guzmán P, Peguero-Pina JJ, Gil L, Karabourniotis G, Khayet M, Fasseas C, Heredia-Guerrero JA, Heredia A, Gil-Pelegrín E. Wettability, Polarity, and Water Absorption of Holm Oak Leaves: Effect of Leaf Side and Age. Plant Physiol. 2014;166:168–80.
3. Ganthaler A, Bauer H, Gruber A, Mayr M, Oberhuber W, Mayr S. Effects of the needle bladder rust (Chrysomyxa rhododendri) on Norway spruce: implications for subalpine forests. Eur J Forest Res. 2014;133:201–11.
4. Kerstiens G. Cuticular water permeability and its physiological significance. J Exp Bot. 1996;47:1813–32.
5. Krauss P, Markstadter C, Riederer M. Attenuation of UV radiation by plant cuticles from woody species. Plant, Cell Environ. 1997;20:1079–85.
6. Riederer M, Schreiber L. Protecting against water loss: analysis of the barrier properties of plant cuticles. J Exp Bot. 2001;52:2023–32.
7. Yeats TH, Rose JKC. The Formation and Function of Plant Cuticles. Plant Physiol. 2013;163:5–20.
8. Martin LBB, Rose JKC. There's more than one way to skin a fruit: formation and functions of fruit cuticles. J Exp Bot. 2014;65:4639–51.
9. Riederer M. Introduction: Biology of the Plant Cuticle. In: Roberts JA, ed. Annual Plant Reviews online. 2018. p. 1–10
10. Serrano M, Coluccia F, Torres M, L'Haridon F, Metraux JP. The cuticle and plant defense to pathogens. Front Plant Sci. 2014;5:274.
11. Lewandowska M, Keyl A, Feussner I. Wax biosynthesis in response to danger: its regulation upon abiotic and biotic stress. New Phytol. 2020;227:698–713.
12. Eigenbrode SD, Jetter R. Attachment to plant surface waxes by an insect predator. Integr Comp Biol. 2002;42:1091–9.
13. Weissflog I, Vogler N, Akimov D, Dellith A, Schachtschabel D, Svatos A, Boland W, Dietzek B, Popp J. Toward in vivo chemical imaging of epicuticular waxes. Plant Physiol. 2010;154:604–10.
14. Lopez-Casado G, Matas AJ, Dominguez E, Cuartero J, Heredia A. Biomechanics of isolated tomato (Solanum lycopersicum L) fruit cuticles: the role of the cutin matrix and polysaccharides. J Exp Bot. 2007;58:3875–83.
15. Gniwotta F, Vogg G, Gartmann V, Carver TLW, Riederer M, Jetter R. What do microbes encounter at the plant surface? chemical composition of pea leaf cuticular waxes. Plant Physiol. 2005;139:519–30.
16. Jeffree CE, Sandford AP. Crystalline-structure of plant epicuticular waxes demonstrated by cryostage scanning electron-microscopy. New Phytol. 1982;91:549–59.
17. Jeffree CE, Baker EA, Holloway PJ. Ultrastructure and Recrystallization of Plant Epicuticular Waxes. New Phytol. 1975;75:539.
18. Jeffree CE, Johnson RP, Jarvis PG. Epicuticular wax in the stomatal antechamber of sitka spruce and its effects on the diffusion of water vapour and carbon dioxide. Planta. 1971;98:1–10.
19. Kim KW, Lee IJ, Kim CS, Lee DK, Park EW. Micromorphology of epicuticular waxes and epistomatal chambers of pine species by electron microscopy and white light scanning interferometry. Microsc Microanal. 2010;17:118–24.
20. Muhammad S, Wuyts K, Nuyts G, De Wael K, Samson R. Characterization of epicuticular wax structures on leaves of urban plant species and its association with leaf wettability. Urban For Urban Greening. 2020;47:126557.
21. Wen M, Buschhaus C, Jetter R. Nanotubules on plant surfaces: Chemical composition of epicuticular wax crystals on needles of Taxus baccata L. Phytochemistry. 2006;67:1808–17.
22. Guzmán P, Fernández V, Khayet M, García ML, Fernández A, Gil L. Ultrastructure of plant leaf cuticles in relation to sample preparation as observed by transmission electron microscopy. Sci World J. 2014;2014:1–9.
23. Guzmán P, Fernández V, García ML, Khayet M, Fernández A, Gil L. Localization of polysaccharides in isolated and intact cuticles of eucalypt, poplar and pear leaves by enzyme-gold labelling. Plant Physiol Biochem. 2014;76:1–6.
24. Nawrath C, Schreiber L, Franke RB, Geldner N, Reina-Pinto JJ, Kunst L. Apoplastic diffusion barriers in arabidopsis. Arabidopsis Book. 2013;11:e0167.
25. Kwiatkowska M, Wojtczak A, Poplonska K, Polit JT, Stepinski D, Dominguez E, Heredia A. Cutinsomes and lipotubuloids appear to participate in cuticle formation in Ornithogalum umbellatum ovary epidermis: EM-immunogold research. Protoplasma. 2014;251:1151–61.
26. Segado P, Dominguez E, Heredia A. Ultrastructure of the Epidermal Cell Wall and Cuticle of Tomato Fruit (Solanum lycopersicum L) during Development. Plant Physiol. 2016;170:935–46.
27. Tenberge KB. Ultrastructure and development of the outer epidermal wall of spruce (Picea-Abies) Needles. Can J Bot Revue Canadienne De Botanique. 1992;70:1467–87.
28. Wattendorff J, Holloway PJ. Studies on the ultrastructure and histochemistry of plant cuticles - isolated cuticular membrane preparations of agave-americana l and the effects of various extraction procedures. Ann Bot. 1982;49:769–804.
29. Guzmán-Delgado P, Fernández V, Venturas M, Rodríguez-Calcerrada J, Gil L. Surface properties and physiology of Ulmus laevis and U. minor

samaras: implications for seed development and dispersal. Tree Physiol. 2017;37:815–26.

30. Guzmn P, Fernndez V, GraÃa J, Cabral V, Kayali N, Khayet M, Gil L. Chemical and structural analysis of Eucalyptus globulus and E camaldulensis leaf cuticles: a lipidized cell wall region. Front Plant Sci. 2014;5:8.
31. Solovchenko A, Merzlyak M. Optical properties and contribution of cuticle to UV protection in plants: experiments with apple fruit. Photochem Photobiol Sci. 2003;2:861–6.
32. Szafranek B, Tomaszewski D, Pokrzywinska K, Golebiowski M. Microstructure and chemical composition of leaf cuticular waxes in two Salix species and their hybrid. Acta Biologica Cracoviensia Series Botanica. 2008;50:49–54.
33. Buschhaus C, Herz H, Jetter R. Chemical composition of the epicuticular and intracuticular wax layers on the adaxial side of Ligustrum vulgare leaves. New Phytol. 2007;176:311–6.
34. Buschhaus C, Hager D, Jetter R. Wax Layers onCosmos bipinnatus-Petals contribute unequally to total petal water resistance. Plant Physiol. 2015;167:80–8.
35. Moreira CJS, Bento A, Pais J, Petit J, Escorcio R, Correia VG, Pinheiro A, Halinski LP, Mykhaylyk OO, Rothan C, Silva Pereira C. An ionic liquid extraction that preserves the molecular structure of cutin shown by nuclear magnetic resonance. Plant Physiol. 2020;184:592–606.
36. Oros DR, Standley LJ, Chen XJ, Simoneit BRT. Epicuticular wax compositions of predominant conifers of western North America. Zeitschrift Fur Naturforschung C-a J Biosci. 1999;54:17–24.
37. Franich RA, Wells LG, Holland PT. Epicuticular wax of pinus-radiata needles. Phytochemistry. 1978;17:1617–23.
38. Hunt GM, Baker EA. Phenolic constituents of tomato fruit cuticles. Phytochemistry. 1980;19:1415–9.
39. Jetter R, Riederer M. Composition of cuticular waxes on Osmunda regalis fronds. J Chem Ecol. 2000;26:399–412.
40. Jetter R, Riederer M. In-vitro reconstitution of epicuticular wax crystals - formation of tubular aggregates by long-chain secondary alkanediols. Botanica Acta. 1995;108:111–20.
41. Kögel-Knabner I, de Leeuw JW, Tegelaar EW, Hatcher PG, Kerp H. A lignin-like polymer in the cuticle of spruce needles: implications for the humification of spruce litter. Org Geochem. 1994;21:1219–28.
42. Prügel B, Lognay G. Composition of the Cuticular Waxes ofPicea abies andP sitchensis. Phytochem Anal. 1996;7:29–36.
43. Jetter R, Riederer M. Localization of the Transpiration Barrier in the Epi- and intracuticular waxes of eight plant species: water transport resistances are associated with fatty acyl rather than alicyclic components. Plant Physiol. 2016;170:921–34.
44. Reynhardt EC, Riederer M. Structures and Molecular-Dynamics of Plant Waxes 2 Cuticular Waxes from Leaves of Fagus-Sylvatica L and Hordeum-Vulgare L. Eur Biophys J Biophys Lett. 1994;23:59–70.
45. Bourgault R, Matschi S, Vasquez M, Qiao PF, Sonntag A, Charlebois C, Mohammadi M, Scanlon MJ, Smith LG, Molina I. Constructing functional cuticles: analysis of relationships between cuticle lipid composition, ultrastructure and water barrier function in developing adult maize leaves. Ann Bot. 2020;125:79–91.
46. Goodwin SM, Kolosova N, Kish CM, Wood KV, Dudareva N, Jenks MA. Cuticle characteristics and volatile emissions of petals in Antirrhinum majus. Physiol Plant. 2003;117:435–43.
47. Tulloch AP, Bergter L. Epicuticular Wax of Juniperus-Scopulorum. Phytochemistry. 1981;20:2711–6.
48. Villena JF, Dominguez E, Stewart D, Heredia A. Characterization and biosynthesis of non-degradable polymers in plant cuticles. Planta. 1999;208:181–7.
49. Heredia-Guerrero JA, Benitez JJ, Dominguez E, Bayer IS, Cingolani R, Athanassiou A, Heredia A. Infrared and Raman spectroscopic features of plant cuticles: a review. Front Plant Sci. 2014;5:305.
50. Heredia-Guerrero JA, Benitez JJ, Cataldi P, Paul UC, Contardi M, Cingolani R, Bayer IS, Heredia A, Athanassiou A. All-natural sustainable packaging materials inspired by plant cuticles. Adv Sustain Syst. 2017;1:1600024.
51. Fernandez V, Guzman-Delgado P, Graca J, Santos S, Gil L. Cuticle structure in relation to chemical composition: re-assessing the prevailing model. Front Plant Sci. 2016;7:427.
52. Buda GJ, Isaacson T, Matas AJ, Paolillo DJ, Rose JKC. Three-dimensional imaging of plant cuticle architecture using confocal scanning laser microscopy. Plant J. 2009;60:378–85.
53. Veraverbeke EA, Van Bruaene N, Van Oostveldt P, Nicolai BM. Non destructive analysis of the wax layer of apple (Malus domestica Borkh) by means of confocal laser scanning microscopy. Planta. 2001;213:525–33.
54. Mazurek S, Mucciolo A, Humbel BM, Nawrath C. Transmission Fourier transform infrared microspectroscopy allows simultaneous assessment of cutin and cell-wall polysaccharides of Arabidopsis petals. Plant J. 2013;74:880–91.
55. PratsMateu B, Hauser MT, Heredia A, Gierlinger N. Waterproofing in arabidopsis: following phenolics and lipids in situ by confocal Raman Microscopy. Front Chem. 2016;4:7.
56. Littlejohn GR, Mansfield JC, Parker D, Lind R, Perfect S, Seymour M, Smirnoff N, Love J, Moger J. In vivo chemical and structural analysis of plant cuticular waxes using stimulated Raman scattering microscopy. Plant Physiol. 2015;168:18–28.
57. Colthup NB, Daly LH, Wiberley SE. Introduction to Infrared and Raman Spectroscopy. 3rd ed. New York: Academic Press Inc; 1990.
58. Edwards HGM, Farwell DW, Jenkins R, Seaward MRD. Vibrational Raman-spectroscopic studies of calcium-oxalate monohydrate and dihydrate in lichen encrustations on renaissance frescoes. J Raman Spectrosc. 1992;23:185–9.
59. Varsanyi G. Vibrational Spectra of Benzene Derivatives. 1st ed. New York: Academic Press; 1969.
60. Wiley JH. Raman Spectra of Celluloses. Doctor's Dissertation. Lawrence University, The Institute of Paper Chemistry; 1986.
61. Gierlinger N. New insights into plant cell walls by vibrational microspectroscopy. Appl Spectrosc Rev. 2018;53:517–51.
62. Prats-Mateu B, Felhofer M, de Juan A, Gierlinger N. Multivariate unmixing approaches on Raman images of plant cell walls: new insights or overinterpretation of results? Plant Methods. 2018;14:52.
63. Fich EA, Segerson NA, Rose JKC. The plant polyester cutin: biosynthesis, structure, and biological roles. Annu Rev Plant Biol. 2016;67(67):207–33.
64. Bock P, Gierlinger N. Infrared and Raman spectra of lignin substructures: Coniferyl alcohol, abietin, and coniferyl aldehyde. J Raman Spectrosc. 2019;50:778–92.
65. Schmid ED, Brosa B. Raman Intensity and Conjugation 1 Substituent Dependence of Raman Intensities of 1600 1/Cm Ring Vibrations of Monosubstituted Benzene Derivatives. Berichte Der Bunsen-Gesellschaft Fur Physikalische Chemie. 1971;75:1334–43.
66. Turtola S, SallaS L, Holopainen JK, Julkunen-Tiitto R, Kainulainen P. Long-term exposure to enhanced UV-B radiation has no significant effects on growth or secondary compounds of outdoor-grown Scots pine and Norway spruce seedlings. Environ Pollut. 2006;144:166–71.
67. Jung MJ, Jung HA, Kang SS, Hwang GS, Choi JS. A New Abietic Acid-Type Diterpene Glucoside from the Needles of Pinus densiflora. Arch Pharmacal Res. 2009;32:1699–704.
68. Metsämuuronen S, Sirén H. Bioactive phenolic compounds, metabolism and properties: a review on valuable chemical compounds in Scots pine and Norway spruce. Phytochem Rev. 2019;18:623–64.
69. Karapandzova M, Stefkov G, Cvetkovikj I, Stanoeva JP, Stefova M, Kulevanova S. Flavonoids and other phenolic compounds in needles of Pinus peuce and Other Pine Species from the Macedonian Flora. Natl Product Commun. 2015;10:987–90.
70. Bock P, Nousiainen P, Elder T, Blaukopf M, Amer H, Zirbs R, Potthast A, Gierlinger N. Infrared and Raman spectra of lignin substructures: Dibenzodioxocin. J Raman Spectrosc. 2020;51:422–31.
71. Solhaug KA. Stilbene Glucosides in Bark and Needles from Picea Species. Scand J For Res. 1990;5:59–67.
72. Felhofer M, Prats-Mateu B, Bock P, Gierlinger N. Antifungal stilbene impregnation: transport and distribution on the micron-level. Tree Physiol. 2018;38:1526–37.
73. Agarwal UP, Atalla RH. Raman Spectroscopic Evidence for Coniferyl Alcohol Structures in Bleached and Sulfonated Mechanical Pulps. 1993;531:26–44.
74. Farber C, Wang R, Chemelewski R, Mullet J, Kurouski D. Nanoscale structural organization of plant epicuticular wax probed by atomic force microscope infrared spectroscopy. Anal Chem. 2019;91:2472–9.

75. Gunthardt MS, Wanner H. The amount of cuticular growth on needles of Pinus-Cembra L and Picea-Abies (L) Karsten in Relation to Needle Length and Location. Flora. 1982;172:125–37.
76. Ensikat HJ, Boese M, Mader W, Barthlott W, Koch K. Crystallinity of plant epicuticular waxes: electron and X-ray diffraction studies. Chem Phys Lipids. 2006;144:45–59.
77. Pfündel EE, Agati G, Cerovic ZG. Optical properties of plant surfaces. In: Riederer M, Müller C, editors. Biology of the Plant Cuticle. Oxford: Blackwell Publishing Ltd; 2006.
78. Gierlinger N, Luss S, Konig C, Konnerth J, Eder M, Fratzl P. Cellulose microfibril orientation of Picea abies and its variability at the micron-level determined by Raman imaging. J Exp Bot. 2009;61:587–95.
79. Sun L, Singh S, Joo M, Vega-Sanchez M, Ronald P, Simmons BA, Adams P, Auer M. Non-invasive imaging of cellulose microfibril orientation within plant cell walls by polarized Raman microspectroscopy. Biotechnol Bioeng. 2016;113:82–90.
80. Heredia A. Biophysical and biochemical characteristics of cutin, a plant barrier biopolymer. Biochim Biophys Acta. 2003;1620:1–7.
81. Stark RE, Tian S. The Cutin Biopolymer Matrix. In: Roberts JA, ed. Annual Plant Reviews online. 2018. p. 126–144
82. Holloway PJ. Surface factors affecting the wetting of leaves. Pestic Sci. 1970;1:156–63.
83. Stark R, Tian S. The Cutin Biopolymer Matrix. 2007. p. 126–144
84. Ray AK, Lin YY, Gerard HC, Chen ZJ, Osman SF, Fett WF, Moreau RA, Stark RE. Separation and identification of lime cutin monomers by high-performance liquid-chromatography and mass-spectrometry. Phytochemistry. 1995;38:1361–9.
85. Holloway PJ. Chemical constitution of plant cutins. 1982.
86. Baker EA, Procopiou J, Hunt GM. The cuticles of Citrus species. Composition of leaf and waxes. 1975.
87. Reina JJ, Heredia A. Plant cutin biosynthesis: the involvement of a new acyltransferase. Trends Plant Sci. 2001;6:296.
88. Graca J, Pereira H. Suberin structure in potato periderm: glycerol, long-chain monomers, and glyceryl and feruloyl dimers. J Agric Food Chem. 2000;48:5476–83.
89. Graça J. Glycerol and glyceryl esters of ω-hydroxyacids in cutins. Phytochemistry. 2002;61:205–15.
90. Luque P, Heredia A. Glassy State in Plant Cuticles during Growth. Zeitschrift Fur Naturforschung Section C-a Journal of Biosciences. 1994;49:273–5.
91. Laguna L, Casado CG, Heredia A. Flavonoid biosynthesis in tomato fruit cuticles after in vivo incorporation of H-phenylalanine precursor. Physiol Plant. 1999;105:491–8.
92. Franceschi VR, Horner HT. A microscopic comparison of calcium-oxalate crystal idioblasts in plant-parts and callus-cultures of Psychotria-Punctata (Rubiaceae). Z Pflanzenphysiol. 1980;97:449–55.
93. Gal A, Brumfeld V, Weiner S, Addadi L, Oron D. Certain biominerals in leaves function as light scatterers. Adv Mater. 2012;24:77–83.
94. Tillman-Sutela E, Kauppi A. Calcium oxalate crystals in the mature seeds of Norway spruce, Picea abies (L) Karst. Trees-Struct Funct. 1999;13:131–7.
95. Webb MA. Cell-mediated crystallization of calcium oxalate in plants. Plant Cell. 1999;11:751–61.
96. Hudgins JW, Krekling T, Franceschi VR. Distribution of calcium oxalate crystals in the secondary phloem of conifers: a constitutive defense mechanism? New Phytol. 2003;159:677–90.
97. Franceschi VR, Nakata PA. Calcium oxalate in plants: Formation and function. Annu Rev Plant Biol. 2005;56:41–71.
98. Kuo-Huang LL, Ku MSB, Franceschi VR. Correlations between calcium oxalate crystals and photosynthetic activities in palisade cells of shade-adapted Peperomia glabella. Bot Stud. 2007;48:155–64.
99. Pierantoni M, Tenne R, Brumfeld V, Kiss V, Oron D, Addadi L, Weiner S. Plants and light manipulation: the integrated mineral system in okra leaves. Adv Sci. 2017;4:1600416.
100. Cote GG. Diversity and distribution of idioblasts producing calcium oxalate crystals in Dieffenbachia seguine (Araceae). Am J Bot. 2009;96:1245–54.
101. Karabourniotis G, Horner HT, Bresta P, Nikolopoulos D, Liakopoulos G. New insights into the functions of carbon-calcium inclusions in plants. New Phytol. 2020;228:845–54.
102. Horner HT, Wagner BL. The Association of Druse Crystals with the Developing Stomium of Capsicum-Annuum (Solanaceae) Anthers. Am J Bot. 1980;67:1347–60.
103. Molano-Flores B. Herbivory and calcium concentrations affect calcium oxalate crystal formation in leaves of Sida (Malvaceae). Ann Bot. 2001;88:387–91.
104. Fink S. Comparative microscopical studies on the patterns of calcium oxalate distribution in the needles of various conifer species. Botanica Acta. 1991;104:306–15.
105. Hoque E, Remus G. Natural UV-screening mechanisms of Norway spruce (Picea abies [L] Karst) needles. Photochem Photobiol. 1999;69:177–92.
106. Synytsya A, Copıkova J, Matejka P, Machovic V. Fourier transform Raman and infrared spectroscopy of pectins. Carbohyd Polym. 2003;54:97–106.
107. Frost RL, Yang J, Ding Z. Raman and FTIR spectroscopy of natural oxalates: implications for the evidence of life on Mars. Chin Sci Bull. 2003;48:1844–52.
108. Machado NFL, de Carvalho LAEB, Otero JC, Marques MPM. The autooxidation process in linoleic acid screened by Raman spectroscopy. J Raman Spectrosc. 2012;43:1991–2000.
109. Agarwal UP. Raman imaging to investigate ultrastructure and composition of plant cell walls: distribution of lignin and cellulose in black spruce wood (Picea mariana). Planta. 2006;224:1141–53.
110. Maddams WF. The scope and limitations of curve fitting. Appl Spectrosc. 1980;34:245–67.
111. Losso A, Sailer J, Bar A, Ganthaler A, Mayr S. Insights into trunks of Pinus cembra L: analyses of hydraulics via electrical resistivity tomography. Trees (Berl West). 2020;34:999–1008.
112. Shinzawa H, Awa K, Kanematsu W, Ozaki Y. Multivariate data analysis for Raman spectroscopic imaging. J Raman Spectrosc. 2009;40:1720–5.

Publisher's Note